ELECTRICAL AND MAGNETIC PROPERTIES OF Ni-Ti SUBSTITUTED PEROVSKITES

Sanele Tobias Dlamini

BSc (University of KwaZulu-Natal), BSc(Hons)(University of the Witwatersrand)

Submitted in fulfilment of the academic requirements for the degree of Master of Science in Physics, School of Chemistry and Physics, University of KwaZulu-Natal, Durban, South Africa

August 2018

Abstract

All perovskites samples studied in this work: (La,Bi,Sr)$Ni_{0.25}Ti_{0.25}Fe_{0.5}O_3$ were synthesized by a combination of high energy ball milling (HEBM) on a Retsch PM 400 instrument and heat treatment on a Sentro Tech (type: STT-1600C-3-24) high temperature tube furnace. These samples were selected in anticipation of a future study of gas sensing properties not undertaken in this work because of equipment constraints. The additional $Ni_{0.5}Ti_{0.5}Fe_2O_4$ spinel ferrite was synthesized by HEBM. The compounds were characterized by X-ray diffraction (XRD), Fourier transform infrared spectroscopy (FTIR), high resolution transmission electron microscopy (HRTEM), Mössbauer spectroscopy, vibrating sample magnetometer (VSM) at temperatures between 10 K and 300 K, resistivity four probe method, Brunauer-Emmett-Teller (BET) and Barrett-Joyner-Halenda (BHJ) for surface area measurements.

The X-ray diffraction data for $LaNi_{0.25}Ti_{0.25}Fe_{0.5}O_3$ (LNTFO) showed the formation of single phase compound with orthorhombic structure which is similar to that of reported $LaFeO_3$. The average particle size obtained from HRTEM was 91±5 nm. The co-substitution of Ni^{2+} and Ti^{3+} at the Fe^{3+} site indicated enhanced magnetic properties. Magnetization measurements showed soft ferromangetic behavior with saturation magnetisation M_S in the range 2.25±0.2 emu/g (at 300 K) to 2.61±0.2 emu/g (at 10 K). The coercivity increased from 0.36±0.02 kOe to 0.41±0.02 kOe with decreasing temperatures. Mössbauer data revealed the sample was magnetically ordered at room temperature. The isomer shift values indicated possible strong covalent bonds between metal and the oxygen ions and existence of only Fe^{3+} ions in the structure. Furthermore, the milled material showed semiconducting behavior with activation energy of 3.4±0.1 eV whilst the milled and annealed sample has lower activation energy of 0.9±0.06 eV.

A $BiNi_{0.25}Ti_{0.25}Fe_{0.5}O_3$ (BNTFO) perovskite compound has been successfully synthesized by high energy ball milling and annealing. The crystallites size were obtained to be in the range 10 nm to 70 nm. The grains were observed to be semi-spherical with good surface coverage. We found improved saturation magnetization relative to the LNTFO sample with M_S in the range 6.5±0.2 emu/g (at 300 K) to 7. 3±0.2 emu/g (10 K) and the coercivity in the range 0.49±0.02 kOe (300 K) to 0.62±0.02 kOe (10 K). Mössbauer

spectrum reveals magnetic ordering at room temperature. Isomer shift values indicated only the presence of Fe^{3+} ions. Magnetic hyperfine values at 300 K were obtained to be 518±5 kOe and 510±4 kOe for the A and B sites respectively. A low activation energy of 0.66±0.02 eV was obtained for this sample.

$SrNi_{0.25}Ti_{0.25}Fe_{0.5}O_3$ (SNTFO) belonging to an orthorhombic crystal system showed paramagnetic behavior at room temperature whilst at lower temperatures it was superparamagnetic. The magnetization M_S was relatively low ranging from 14.14±0.23 emu/g to 0.0032±0.0001 emu/g and the coercive field increased with decreasing temperature from 0.34±0.06 kOe to 1.14±0.06 kOe. The Mössbauer spectrum indicated the presence of both Fe^{4+} and Fe^{3+} iron ions which is consistent to that reported for $SrFeO_3$ compounds. Particle size obtained from FETEM averaged 127±12 nm and the surface morphology was indicative of a rough absorber surface with semi-spherical grains of different sizes. An activation energy of 0.37±0.03 eV for the annealed SNTFO indicated good electronic conductivity at relatively higher temperature.

An additional $Ni_{0.5}Ti_{0.5}Fe_2O_4$ compound was successfully synthesized by HEBM. The sample was characterized by quick phase formation. Prolonged milling destroyed the phase. From the structural analysis it was evident that starting precursors for a chemical reaction are of vital importance as they have great influence on the reaction product. The mean particle size was obtained to be 45±9 nm. Particle size reduced with milling time whilst the strain increased. The coercivity and saturation magnetization appeared to follow the Stoner–Wohlfarth model in two distinct regions at high temperatures (300 K to 100 K) and low temperatures (50 K to 10 K) with approximately equal anisotropies in each temperature range. Saturation magnetization was obtained to be between 38.73±0.03 emu/g to 38.84±0.03 emu/g and the coercivity was between 820±32 Oe to 407±32 Oe. Room temperature Mössbauer spectrum revealed hyperfine fields of 446±1 kOe and 480±1 kOe for A and B sites respectively. Isomer shift values indicated co-existence of both Fe^{3+} and Fe^{2+}.

Preface

The experimental work described in this dissertation was conducted at the Condensed Matter Physics Lab, School of Chemistry and Physics, Westville Campus, University of KwaZulu-Natal, Durban, South Africa. The project was completed under the supervision of Dr. Thomas Moyo.

The content presented in this dissertation represents original work by the author and has not been submitted in any form for any degree or diploma to any other tertiary institution. Where use has been made of the work of others it is duly acknowledged in the text.

College of Agriculture, Engineering and Science

Declaration 1 - Plagiarism

Sanele Tobias Dlamini declares that

1. The research reported in this dissertation, except where otherwise indicated, is my original research.

2. This dissertation has not been submitted for any degree or examination at any university.

3. This dissertation does not contain other person's data, pictures, graphs or other information, unless specifically acknowledged as being sourced from other persons.

4. This dissertation does not contain other persons writings, unless specifically acknowledged as being sourced from other researchers. When other written sources have been quoted, then:

5. Their words have been re-written but general information attributed to them has been referenced.

6. Where their exact words have been used, their writing has been placed in italics and inside quotation, and referenced.

7. This dissertation does not contain text, graphics or tables copied and pasted from internet, unless specifically acknowledged, and the source being detailed in the dissertation and in the reference sections.

Declaration 2

Publications

1. **S. T. Dlamini** and T. Moyo. Structural, Electrical and Magnetic Characterization of $La\,Ni_{0.25}\,Ti_{0.25}\,Fe_{0.5}O_3$ perovskite. *In process* 2018.

2. W. B. Mdlalose, S. R. Mokhosi, **S. T. Dlamini**, T. Moyo and M. Singh. Effect of chitosan coating on the structural and magnetic properties of $MnFe_2O_4$ and $Mn_{0.5}Co_{0.5}Fe_2O_4$ nanoparticles. *AIP Advances*, **8** , 056726 (2018).

3. K. Mbela, T. Moyo, I. P. Ezekiel and **S. T. Dlamini**. Superparamagnetic behaviour and exchange bias in $Sn_{0.2}Fe_xCr_{1.8-x}O_3$ nano oxides. *Submitted*.

4. I. P. Ezekiel, T. Moyo and **S. T. Dlamini**. Mechanical milling effect on the structural and magnetic properties of sintered $La_{0.67}\,Sr_{0.33}\,MnO_3$. Accepted. *SAIP*. 2018.

5. **S. T. Dlamini** and T. Moyo. Synthesis, structural and magnetic properties of $Ni_{0.5}Ti_{0.5}Fe_2O_4$. *In process* 2018.

Signed: ..... Date: April 2018

Name: Sanele Tobias Dlamini

Dedication

I dedicate this dissertation to my family for their love and support. Especially my mother Vuyisile Dlamini for her constant encouragement and support. God bless you all.

Acknowledgements

I would like to express my deepest thanks and gratitude to Dr T. Moyo for his advice and for always being available when needed. It has been a great honor to work under his supervision. I would also like to express my deepest thanks and appreciation to Itegbeyogene Patrick Ezekiel for his insightful discussions and support especially at the beginning of my project. Patrick, you have been a great friend and colleague. I would also like to extend my thanks and gratitude to Wendy Bonakele Mdlalose for her insightful advice.

I would like to thank the School of Chemistry and Physics, Westville Campus for providing all possible assistance. I also extend my thanks to the National Research Foundation of South Africa for research and equipment grants. Thank you to the members of the Electron Microscope Unit, Westville Campus for HRTEM, SEM and EDX measurements. I would also like to thank Mr. P. Suthan for assisting with XRD measurements.

Contents

List of Figures

List of Tables

List of Abbreviations and Acronyms

HEBM	High-Enegy Ball Milling
ABO_3	Perovskite oxide general formulation
SEM	Scanning Electron Microscopy
HRTEM	High-Resolution Transmission Microscopy
FTIR	Fourier Transform Infrared Spectroscopy
EDX	Energy-Dispersive X-ray spectroscopy
XRD	X-ray Powder Diffraction
MS	Möbauer Spectroscopy
BET	Brunauer-Emmett-Teller
LNTFO	$LaNi_{0.25}Ti_{0.25}Fe_{0.5}O_3$
LFO	$LaFeO_3$
BNTFO	$BiNi_{0.25}Ti_{0.25}Fe_{0.5}O_3$
BFO	$BiFeO_3$
SNTFO	$SrNi_{0.25}Ti_{0.25}Fe_{0.5}O_3$
SFO	$SrFeO_3$
NTFO	$Ni_{0.5}Ti_{0.5}Fe_2O_4$
D	Average crystillite size
EFG	Electric field gradient
hkl	Miller indices
B	Applied external magnetic field
$\boldsymbol{M}_S$	Saturation Magnetization

$\boldsymbol{M}_R$	Remenant Magnetization
$\boldsymbol{R}$	Squareness ratio
$\boldsymbol{IS}$	Isomer Shift
$\boldsymbol{QS}$	Quadrupole Splitting
$\boldsymbol{f}$	Fractional population
$\boldsymbol{SSA}$	Specific Surface Area
E_a	Activation Energy of ionization
$\boldsymbol{t}$	Tolerance factor
Γ	Line Width
β_{hkl}	Full Width at Half Maximum
λ	X-ray Wavelength of CoKα radiation

Chapter 1

Introduction

1.1 Gas sensors and general background

The air atmosphere that surrounds living organisms contain different kind of gases. Some of the gases are pivotal in supporting life while many others are hazardous. Apart from gases of natural origin, there exist numerous other gases which are of artificial origins such as combustion processes. Gases of human importance such as oxygen are to be monitored and kept at adequate levels while harmful gases should be controlled and maintained at harmless levels. This kind of monitoring and controlling can only be obtained by knowing the concentration of each gas in real time. Gas sensors have been developed as devices which can monitor targeted gas concentrations in real time.

Gas sensors fall under two categories of detection methods i.e direct and indirect method. Direct method is based on spectrometry [1]. Although spectrometers give accurate and stable results, they tend to be heavy and not easily portable. They are also very expensive with complex equipment that is generally used in stationary applications. The indirect detection method is based on the interaction of the gas species and the gas sensor surface that induces a change in electrical resistivity of the sensor material. An electrical signal is produced and is proportional to the concentration of targeted gas species. These types of gas sensors are portable, user friendly and generally are produced at low cost. These are the types of gas sensors that are of interest for this dissertation.

Decades ago, scientists working on p-n junctions discovered that these junctions were

sensitivity to environmental background gases [2]. Furthermore, the interaction of gas molecules with some metal oxide surfaces influenced changes in the surface and their overall properties [2]. These discoveries led to the development of gas sensors based on different characteristics. There are catalytic sensors which operate by burning the gas being detected. The sensor material is consumed and changed in the process and is eventually burnt out. Solid state gas sensors generally consists of one or more metal oxides from transition metals. Their fundamental principle is based on indirect detection method. When the gas being detected disappears, the sensor returns to its original condition. No material is consumed in the process and hence solid state gas sensors offer long life expectancy compared to catalytic sensors.

Scientists are constantly working on improving gas sensors. All gas sensors have advantages and disadvantages. Table 1.1 shows different types of solid state gas sensors with their corresponding physical change used for gas detection. Gas sensors can be applied in automobile, safety, indoor air quality, environmental control, food, industrial production and medicine [3]. The response of gas sensing parameters such as sensitivity, accuracy, response time and selectivity depends on the type of gas sensor [4].

1.2 Gas sensing operating principle

In 1962 an experiment conducted using zinc oxide thin film layers demonstrated that the absorption or desorption of a gas on to the surface of a metal oxide solid changes the conductivity of the material [5]. It is desirable that metal oxide sensors have large surface area in order to increase the probability of gas/solid interaction in the surface of the solid, to give a stronger and measurable response especially at lower concentrations.

Advances in the fabrication techniques have resulted in the production of low cost sensors with improved sensitivity and reliability as compared to previous methods. Metal oxides can be reproduced relatively quickly on a large scale making them a desirable technology to exploit.

Table 1.1: Types of solid state gas sensors with the corresponding physical change used as gas detection principle [3].

Type of device	Physical change
Semiconductor gas sensors	Electrical conductivity
Field effect gas sensors: diodes, transistors, capacitors	Work function (electrical polarisation)
Piezoelectric sensors: Quartz crystal micro-balances (QMB), surface acoustic wave (SAW), micro-cantilevers	Mass
Optical sensors (fibre optic or thin film)	Optical parameters: SPR, reflection, interferometry, absorption, fluorescence, refractive index or optical path length
Catalytic gas sensors: Seebeck effect, pellistors, semistors	Heat or temperature
Electrochemical gas sensors (potentiometer or amperometric)	Electromotive force or electrical current in a solid state electrochemical cell

1.2.1 Basics of band theory

Band theory is important for understanding the principle operation of gas sensors. Band theory states that within a lattice there exists a conduction band and a valence band. The band structure in solids arises due to electrons in the outermost orbits experiencing an attractive force from nearest or neighboring atomic nuclei. Due to this attractive force the energies of the electrons in the same orbit exhibits different energy level. The grouping of these energy levels is referred to as energy band. The energy levels of the electrons are changed to a value which is higher or lower than that of the original energy level of the electron.

The separation between the conduction band and the valence band is a function of en-

ergy particularly the Fermi level. Fermi level energy is the energy level above which the probability of finding an electron is 0 at 0 K that is all electrons have energy less than the Fermi level energy at 0 K, no electrons exist above Fermi level at 0 K. Fermi level lies somewhere between conduction band and valence band and its position is decided by donor and acceptor impurities.

The Fermi energy level for n-type semiconductor lies nearer to the conduction band and in p-type semiconductor it lies closer to the valance band. In n-type semiconductors donor atoms donate electrons to the semiconductor and these electrons are closer to the conduction band so at room temperature they require very little energy for all the donor electrons to go into the conduction band. There are three main classes of material in band theory namely insulators, semiconductors and conductors as illustrated in Figure 1.1.

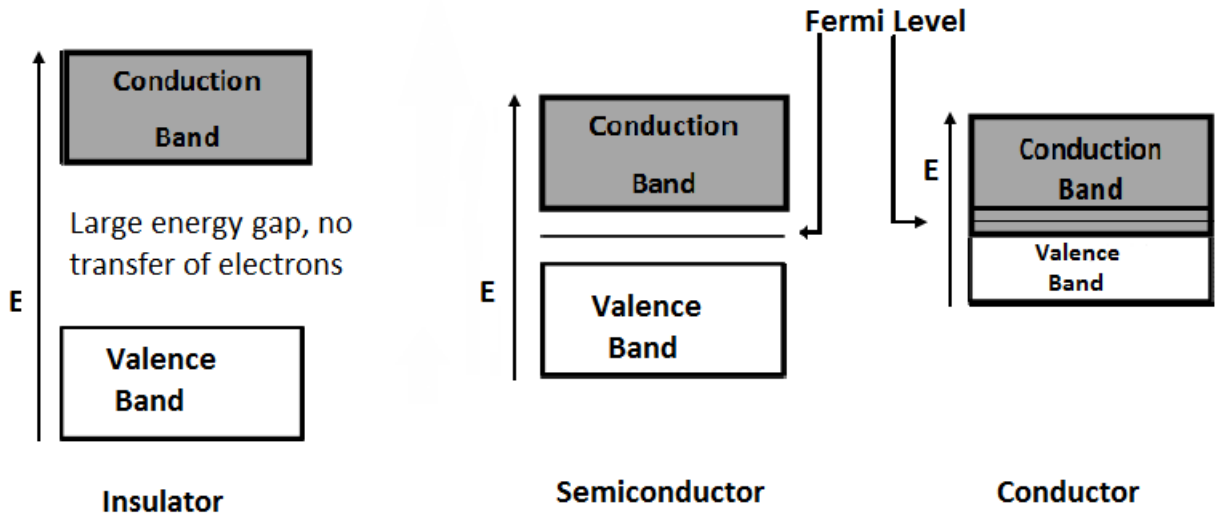

Figure 1.1: Schematic band diagrams of insulator, semi-conductor and conductor.

Insulators have a large energy band gap between the valence and conduction bands typically about 10 eV. This implies that for an insulator to conduct a lot of energy is required to excite electrons to the conduction band. Semiconductors have relatively smaller band gaps in the range of 0.5 - 5.0 eV. If sufficient energy is supplied electrons can transfer to the conduction band and hence increase conductivity. Conductors have the Fermi level lying within the conduction band. The highest occupied state at $T = 0$ is the Fermi level [2].

1.2.1.1 Band theory applied to gas sensors

The most commonly accepted mechanism for semiconductor gas sensors involves a change of the carrier density in the space charge region. This change in carrier concentration serves to alter the conductivity or resistivity of the material. The change in carrier concentration is due to the target gas interacting with the surface of the metal oxide, generally through surface adsorption of oxygen ions. Adsorption or desorption of negatively charged oxygen on the surface of material plays a key role in the detection of oxidizing or reducing gases in air. This detection is governed by the processes of diffusion, adsorption, reaction and desorption of all gases in a given ambient environment. The chemical bond between the adsorbed gas species and surface atoms modify their electronic structure [2]. The oxygen ion adsorption in a semi-conducting material causes conductivity changes. The surface of a metal oxide can adsorb oxygen in molecular or ionic form based on the operating temperatures. The widely accepted model for oxygen adsorption (ads) process is described as:

$$O_{2(gas)} \longleftrightarrow O_{2(ads)} \tag{1.2.1}$$

$$O_{2(ads)} + e^- \longleftrightarrow {O_2}^-_{(ads)} \tag{1.2.2}$$

$${O_2}^-_{(ads)} + e^- \longleftrightarrow 2\,O^-_{(ads)} \tag{1.2.3}$$

$$O^-_{(ads)} + e^- \longleftrightarrow O^{2-}_{(ads)}. \tag{1.2.4}$$

Increasing temperature results in more electron transfers from the valence band to the conduction band. This increases the probability of electron capture by the adsorbed oxygen ions or molecules as described by equation 1.4.2. This changes the electron/hole concentration on the surface resulting in a change of the charge carrier concentration and the overall conductivity. Hence, electronic and chemical phenomena dually control conductivity.

1.3 Effect of nano-crystalline particles in gas sensing properties

Metal oxide gas sensors perfomance is significantly influenced by the morphology and structure of the sensing materials. Sensors based on nanomaterials are of interest as they

tend to improve gas sensing properties such as sensitivity, selectivity and response speed. In general, nanomaterials consists of particles of atleast in one dimension in the range of 1 to 100 nm. In the nanoscale, the physical and chemical properties tend to be generally different from those of corresponding bulk materials.

Gas sensing is based on the interaction of gas species with active sites of metal oxide. Increasing the surface area increases the gas/solid interaction. Generally, sensors are considered to be composed of crystallites that are connected to their neighbors by necks. These interconnected grains form larger aggregates that are connected to their neighbors by grain boundaries. On the surface of the grains, oxygen molecules are adsorbed, these oxygen molecules forces out electrons from the conduction band and trap the electrons at the surface in the form of ions, which produce an electron depleted region referrred to as space charge layer. In nanomaterial when the particle size of the sensing material is closer to or less than double the thickness of the space charge region, the sensitivity increases remarkably. This is explained by Xu's model and is illustrated in Figure 1.2 [6].

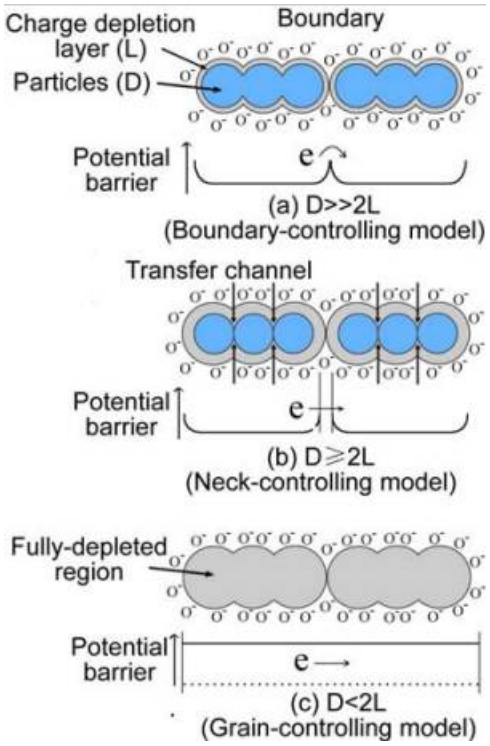

Figure 1.2: Schematic model of the effect of the crystallite size on the sensitivity of metal-oxide gas sensors: (a) $D >> 2L$; (b) $D \geqslant 2L$; $D < 2L$ [6].

The relationship between the particle size (D) and the width of the space charge layer which is produce around the surface of the crystallites due to chemisorbed ions have a major influence on the sensitivity of the material. Xu's model describes that grain conduction controls the overall conductivity of the sensing film, implying that overall conductivity of sensing films can be affected by very low concentration of gas. Therefore a decrease in particle size can directly increase the sensitivity of the sensing material, as shown in Figure 1.3.

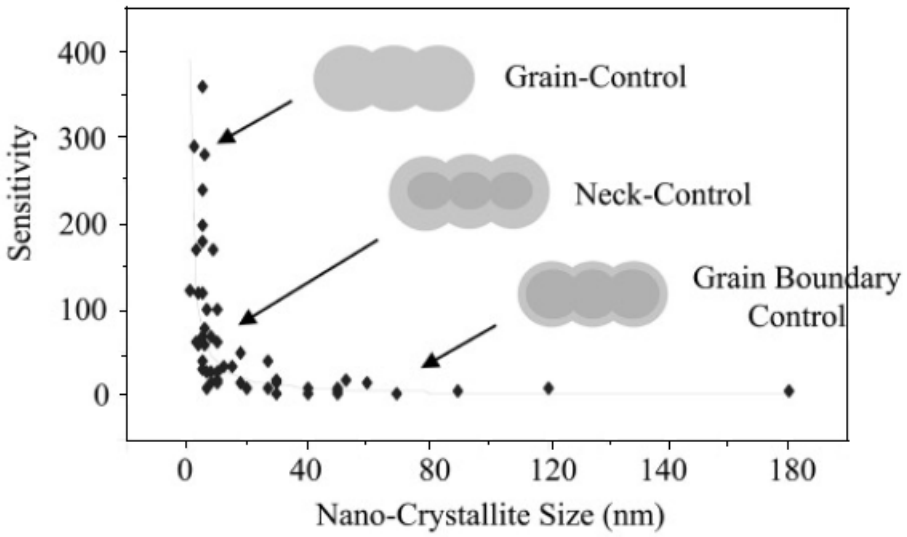

Figure 1.3: The variation in sensitivity as a function of nanocrystallite size for semiconductor oxide gas sensors [7].

1.4 Strategies of the project

The aim of this project is to synthesize, characterize, investigate and explore the influence of equal mole ratios of substituted Ni-Ti into ferrite nano-structured perovskites and investigate their potential application to gas sensors. The preferred method of preparation is high energy ball milling (HEBM) and high temperature treatment as it is cost efficient. The pervoskite structure amongst other metal structured materials is well known for its catalytic activities, doping flexibility and good stability under different working conditions. Figure 1.4 shows a flow chart representing steps followed in the production of the Ni-Ti substituted ferrites perovskites.

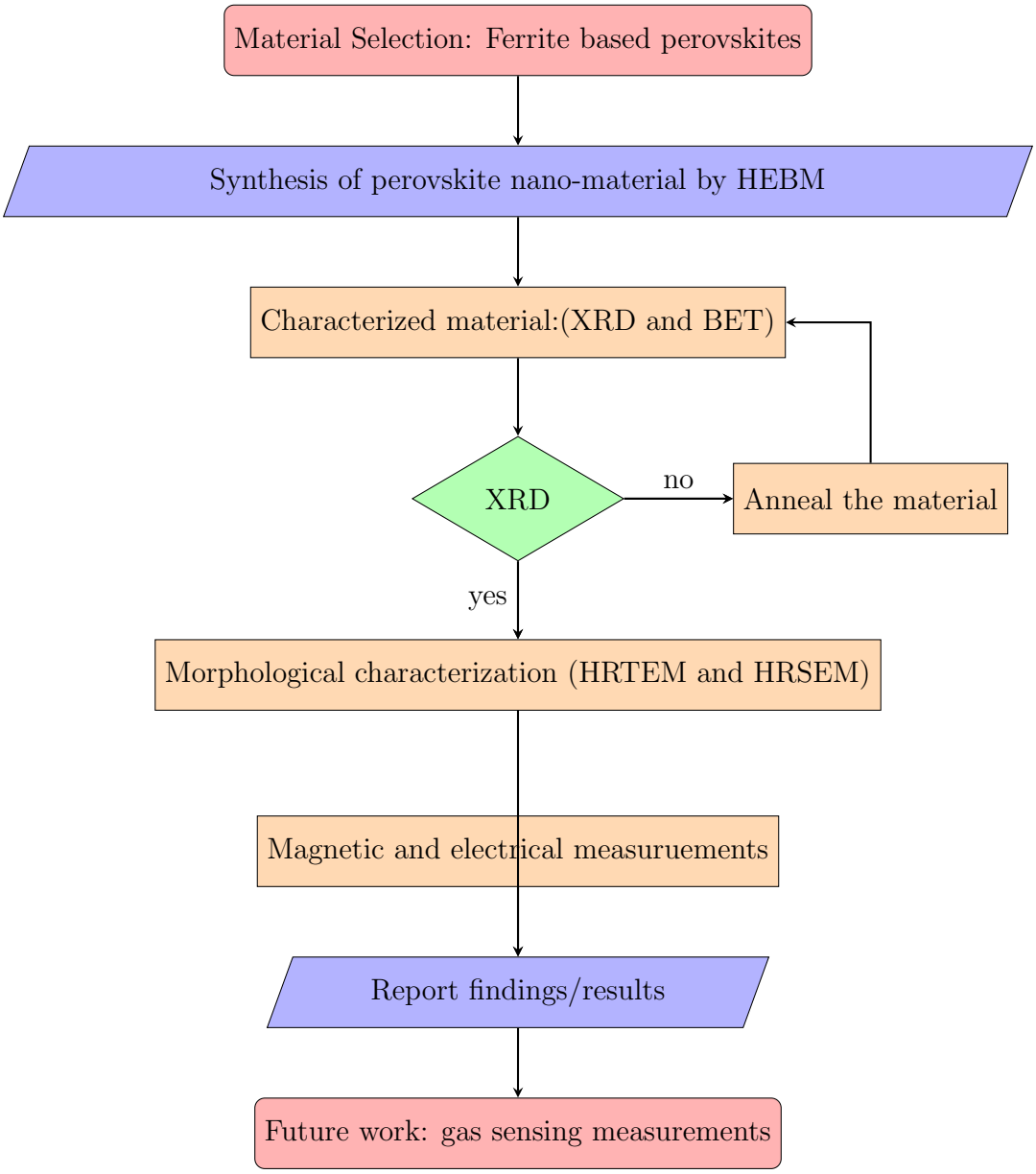

Figure 1.4: Developmental flow chart for processes involved in this project.

1.5 Motivation for the project

The interest of this project is motivated by the fascinating characteristics of the metal alloy of Nickel and Titanuim referred to as Nitinol, where the two elements are present in approximately equal atomic percentages. NiTi alloy behaves differently depending on the crystal structure and changes in temperature. This allows for use of the material in special applications for which normally, complex sensing and actuation systems could be required.

In this study, we aim to investigate and explore Ni-Ti oxides which have equal mole ratio of metal ions simultaneously substituted to the octahedral (B) sites of magnetic nano-structured perovskite obtained by high energy ball milling (HEBM) technique in order to develop cost efficient and high performing gas sensors. The base metal oxide chosen have been reported to have intrinsic gas sensing abilities. Gas sensors are utilised in a variety of fields such as in process control industries, monitoring of environmental hazards, boiler control, fire detection, alcohol breath tests, detection of toxic gases in mines, home safety and grading of agro-products like coffee and spices. The main focus for this project is to synthesize and study properties of materials that have potential applications for gas sensors for environmental application such as emission and combustion process monitoring in vehicles, smoke detection and monitoring of emissions in industrial processes. In combustion based systems gases are released by burning of fossil fuels. The gases released include carbon monoxide (CO), nitrogen oxide NO_x and hydrocarbons. The driving force for this work is the demand to develop more selective sensing and accurate gas sensors at an affordable fabrication and operational cost.

The recent rise in popularity of the field of magnonics has caused increased interest in the development of gas sensors based on magnetic nanoparticles. Recent research has reported ferrites that have shown improved gas sensing properties [8, 9]. However, not much work has been reported on ferrites with perovskites structure even though some studies have often reported to have found the material to have different degrees of gas sensing abilities [10]. It is also well known that metal oxide sensors are relatively inexpensive, more robust, portable, long lasting with high material sensitivity, quick response time compared to other sensing technologies. Moreover, the improved properties of gas

sensing metal oxides are due to their high specific surface area and small crystallite size [11]. However, synthesis of metal oxides tends to pose a challenge in terms of waste treatment, mass production and manufacturing costs. HEBM promises a synthesis technique that has improved capabilities for production of low cost high performing nano-crystallites metal oxides.

Perovskites with the structural formula ABO_3 have received considerable attention as gas sensors and catalysts due to their affordability, thermal and chemical stability. Several perovskite type mixed oxides have been recognised as very active oxidation/reduction catalysts [12]. Metal oxides are one of the widely studied oxide materials owing to their inherent ability to accommodate a wide range of element compositions with a wide range of structural variants. The perovskite structure usually consists of an alkaline earth or rare earth elements on the dedocahedral A sites and transitional metals on the octahedral B sites. In addition, they have the ability to be partially substituted on the A and B sites for example $A_{1-x}A'_xB_{1-y}B'_y$ resulting in a higher degree of freedom for different compositions. The crystal structure is able to easily accommodate different types of dopants in its lattice due to the intrinsic capability of the perovskite structure to accommodate ions of different sizes [13]. This has led to the possibility of tailoring the properties of metal oxides in order to optimize sensing properties and to improve gas sensing. It has also been reported that some ternary metal oxides with perovskites structure have more stable and reliable gas sensing properties [10]. The physical and chemical properties of ternary metal oxides provides micro-structural and morphological stability to improve reliability and long-term sensing performance.

1.6 Dissertation outline

The dissertation consists of 10 chapters. **Chapter 1** gives a review of metal oxide gas sensors and their accepted operating principles. The effect of nanocrystalline materials on gas sensing properties is also discussed. Finally, the strategy of the project is elaborated and also a brief explanation of the motivation behind this project. **Chapter 2** presents a literature review on perovskite structure and their application and also discusses different synthesis routes and their influence on magnetic and electrical properties. **Chapter 3** dis-

cusses the fundamental origin of magnetism in solids. **Chapter 4** presents the principles of the Mössbauer spectroscopy. **Chapter 5** presents experimental techniques relevant to the current study. **Chapter 6** to **Chapter 8** presents results of synthesized perovskites. **Chapter 9** is an additional chapter of surprisingly quick forming $Ni_{0.5}Ti_{0.5}Fe_2O_4$ synthesized by HEBM. **Chapter 10** discusses general conclusion and recommendations of work to be done in the future for the for the as-prepared pervoskite samples.

Chapter 2

Perovskites

Perovskites belong to a large family of compounds having the crystal structure of mineral perovskite $CaTiO_3$. The mineral is named after a Russian minerologist, Count Lev Aleksevich von Perovski. It was descovered and named by Gustav Rose in 1839 from samples found in the Ural mountains [14]. Early structural work on perovskites were conducted by Goldschmidt *et al.* This work formed the basis for further exploration of the perovskite family of compounds. An ideal perovskite has a cubic structure belonging in the space group $Pm-33m$ Oh [15]. However, ideal perovskites are very rare that even the mineral perovskite is not ideally cubic as it consists of some distortions. The structural distortions play key roles in the material's magnetic and electric properties. Due to these properties, perovskites have several applications as summarized in Table 2.1.

2.1 Perovskites structure

A number of perovskite-type oxides have been used as gas sensor materials due to their semi-conductive properties and the flexibility of doping and the ease at which their formulation can be adjusted [17]. These materials can be obtained in pure or doped formulations. Doping flexibility allows the control of the ion transport properties and the adsorption or desorption behaviour. This advantage is useful in optimizing the matierial's performance.

The perovskite structure can be adopted by compounds of the general formula ABO_3, where A and B are cations and O is an anion. Figure 2.1 shows a unit cell for a simple

Table 2.1: Applications of perovskite materials [16].

Application	Material
Multilary capacitor	$BatiO_3$
Piezoelecteric transducer	$Pb(Zr, Ti)O_3$
P.T.C Thermistor	$BatiO_3$
Electrooptical modulator	$(Pb, La)(Zr, Ti)O_3$
Switch	$liNbO_3$
Thick film resistor	$BaRuO_3$
Electrosalctive actuator	$Pb(Mg, Nb)O_3$
Superconductor	$Ba(Pb, Bi)O_3$
Magnetic Bubble Memory	$GdFeO_3$
Laser Host	$YALO_3$
Ferromagnet	$(Ca, La)MnO_3$
Refractor Electrode	$(LaCoO_3)$
Second Harmonic Generator	$KNbO_3$
Gas sensor	$LaFeO_3$

perovskite crystal structure for $SrTiO_3$ as an example. The perovskite structure is ideally cubic with the A site cations at the corners of the cube, B site cations are body centered and oxygen anions face centered. The structure is based on a cubic array sharing BX_6 octahedra, with the A site cations located within the cuboctahedral cavities. However, due to crystal defects the majority of perovskites are not perfectly cubic. Different distortions in the perovskite structure results in the structure taking up tetragonal, orthorombic, and rhombohendral symmetric arrangements [18]. The A site cations are usually alkaline earth or rare earth elements. The B site cations can be $3d$, $4d$ and $5d$ transitional metal elements. A list of some of the elements relevant to this work able to occupy the A and B sites of the perovskite structure is shown in Table 2.2. A number of metallic elements are stable if their Goldschmidt tolerance factor, t, is in the range $0.75 \leqslant t \leqslant 1$ [19]. The Goldschmidt tolerance factor, t, is defined as

$$t = \frac{r_A + r_O}{\sqrt{2}(r_B + r_O)}, \tag{2.1.1}$$

where r_A and r_B are the ionic radii of the A and B cations respectively, and r_O is the ionic radius of the oxygen anion in units of Å.

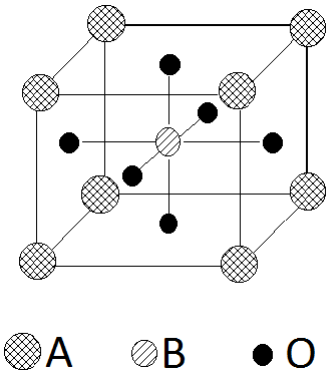

Figure 2.1: A schematic crystal structure of a unit cell for perovskite ABO_3.

Table 2.2: Some of the cations commonly found in perovskite-type oxides [16].

Dedocahedral A site		Octahendral B site	
Ion	Radius Å	Ion	Radius Å
Bi^{3+}	1.07	Fe^{3+}	0.64
La^{3+}	1.22	Ni^{3+}	0.62
Sr^{2+}	1.23	Ti^{3+}	0.76
Ba^{2+}	1.46	Ti^{4+}	0.68

2.2 Magnetic and electrical properties of perovskites

Transitional metal ions substituted on the B sites of perovskite structure show a variety of interesting electrical and magnetic properties [20, 21, 22, 23]. Apart from chemical flexibility these variations are related to the complex coordination of transitional metals ions with oxygen [24]. Magnetic and electronic properties are usually due to 3d unfilled electron shells of the transitional metal ions. Also the tilting of the BO_6 octahedra has great influence on the properties of perovskites. Dielectric properties are due to filled 3d

electron shells of transitional elemental ions and multiferrocity materials are a consequence of the coexistence of spontaneous ferroelectric and ferromagnetic moments. Nevertheless, in competing interactions, canted moments and in composites large, magneto-capacitive coupling has been reported [25, 26, 27]. To a certain extent some of these aspect can be related to applications such as sensors, transducers, actuators and capacitors.

2.3 Synthesis of perovskites

Synthesis techniques play a major role in determining the physical and chemical properties of a material by controlling the structure, morphology, grain size and surface area of the reaction product. Due to this, synthesis routes have vital influence in optimizing different types of applications. Perovskites can be synthesized by high energy ball milling in which metal oxides are used as precursors. However, materials synthesized using ball milling alone tend to have secondary phases. This can be minimized by reaction-grinding technique [28] in order to get pure a phase. Reaction-grinding is a technique that involves ball milling and firing at high temperatures and re-milling again. This technique has been reported to reduce particle size and increase surface area. Solid state reaction has traditionally been used to synthesize perovskites owing to its simplicity and cost efficiency. This technique produces large particle sizes and often results in undesirable secondary phases. However, soft mechano-chemical processing before firing can result in single phase perovskites which may be used in electroceramic applications. Alternatives to the solid state reaction methods are the wet chemistry methods which include techniques such as co-precipitation [28], combustion [29], hydrothermal [30], sol-gel [31] and spray-pyrolysis [32]. Wet chemistry methods can accelerate phase formation. This is due to the liquid media which allows reactions to take place because of better elemental mixing at an atomic level. This results in lower annealing temperature, controllable grain size, morphology and increased surface area. In most cases the micro-structure of interest is important in determining the type of synthesis to be followed. In some materials crystal symmetry plays an important role such as in multiferroic material based devices. Therefore it is worth while to try different kinds of synthesis techniques [33]. The synthesis routes also influence the magnetic and electrical properties of perovskites [34, 35, 36, 37, 38].

Chapter 3

Principles of magnetism

3.1 Magnetism

Magnetic phenomena have been known and exploited for many centuries. The oldest magnetic material is the so-called magnetite (Fe_3O_4) and was initially found in the district of Magnesia of modern Turkey and hence the Greek name magnet. The mineral magnetite was also referred to as lodestone after its property of being able to align itself in certain directions if allowed to rotate freely. Thus it was able to indicate directions of north and south and had the ability to attract and repel pieces of itself. After the production of iron from its ore, it was realized that magnetite could also attract iron. There are numerous magnetic materials today and it is therefore important to know the origin of this phenomenon [39, 40].

The magnetism arises due to magnetic moments which are associated with individual electrons orbiting the nucleus and their intrinsic electron spins. When a magnetic material is placed in the presence of an external magnetic field it can respond in different ways. The most common magnetic responces can reveal paramagnetism, diamagnetism, ferromagnetism, antiferromagnetism and ferrimagnetism.

3.2 Origin of magnetism

The microscopic magnetic properties of materials are a consequence of magnetic moments associated with their individual electrons in atoms. The motion of an electron is not free.

The electron is bound to the atom by the attractive force of the nucleus and consequently quantum machanics predicts that the electron motion and energy is quantised i.e electrons move in specific orbits and emit or absorb specific quantities of energy called quanta [39]. It is well known that magnetic moments originate directly from two sources, the electron orbital motion around the nucleus and the intrinsic electron spin. A schematic diagram illustrating a single electron motion about the nucleus is shown in Figure 3.1.

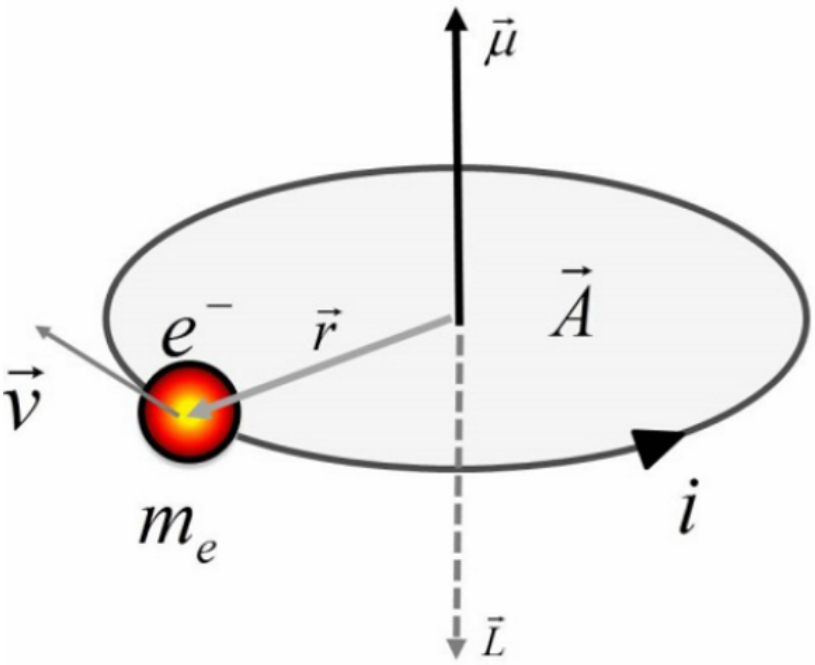

Figure 3.1: Schematic representation of the precession of a single electron [41].

A moving electron constitute a current I. A circulating current is associated with a magnetic moment $\mu = IA$ where A is the area given by πr^2. It can be shown for an electron of charge e moving around a circular loop of radius r with angular speed ω that the electron orbital motion contributes a orbital magnetic moment of

$$\mu_l = I\pi r^2 = \frac{-ew\pi r^2}{2\pi} = \frac{-ewr^2}{2}. \tag{3.2.1}$$

For an electron of mass m_e the orbital magnetic moment can be rewritten as

$$\vec{\mu}_l = \frac{-e}{2m_e}\vec{l}, \tag{3.2.2}$$

where $\vec{l}$ is the orbital angular momentum of magnitude $|\vec{l}| = m_e\omega r^2$.

Similarly, magnetic moments due to intrinsic electron spin $\vec{s}$ can be shown to be

$$\vec{\mu}_s = \frac{-e}{m_e}\vec{s}. \tag{3.2.3}$$

In Quantum mechanics angular momenta of $\vec{l}$ and $\vec{s}$ are quantised in the z direction in units of $\hbar$. hence, $L_z = m_l\hbar$ and $S_z = m_s\hbar$. Therefore, equations 3.2.2 and 3.2.3 can than be rewritten as

$$\mu_{l_z} = \frac{-e\hbar}{2m_e}m_l = -\mu_B m_l \tag{3.2.4}$$

and

$$\mu_{s_z} = \frac{-e\hbar}{m_e}m_s = -2\mu_B m_s \tag{3.2.5}$$

where m_s and m_l are the spin and orbital quantum numbers respectively. The magnetic quantum numbers take values $m_l = 0, \pm1, \pm2, \pm3, ...$ and the spin quantum numbers $m_s = \pm1/2$. μ_B is the Bohr magneton and is the fundamental unit of magnetic moment. The Bohr magneton is given by

$$\mu_B = \frac{e\hbar}{2m_e}, \tag{3.2.6}$$

where $\hbar$ is given by $h/2\pi$ and h is the Planck's constant. The Bohr magneton is equivalent to the lowest non zero value of magnetic moment [42].

Transitional metal ions such as iron group (incomplete 3d shell), palladium group (4d shell), the lanthanide group (4f shell), platinum group (5d shell) and the actinide group (5f shell) are examples of elements that have magnetic moments. Atoms constitute a system of orbital electrons. Hence, the total magnetic moment is determined by the contribution of all the electrons. Therefore, the total angular momenta ($\vec{J}$) is given by the sum of all the angular momenta of all the electrons. The different interactions associated with all the momenta are spin-orbit, orbit-orbit and spin-spin interactions [39]. However, it has been shown experimentally that electrons prefer orbital-orbital interactions and spin-spin interactions. This leads to the so-called Russell-Saunders coupling (L-S coupling). The resultant spin momentum due to spin-spin interactions is given by

$$\vec{S} = \sum \vec{s}_i. \tag{3.2.7}$$

Similarly for orbital-orbital interactions lead to

$$\vec{L} = \sum \vec{l_i}. \tag{3.2.8}$$

The resultant coupling between $\vec{L}$ and $\vec{S}$ through spin-orbit interaction gives a total angular momentum

$$\vec{J} = \vec{L} + \vec{S}. \tag{3.2.9}$$

Hence, the total magnetic moment of an atom can be deduced from spin-spin and orbital-orbital interactions using Russell-Saunders coupling and Hund's rules [42]. The total magnetic moment of an atom in the $\vec{J}$ direction can therefore be shown to be

$$\vec{\mu_J} = -g\mu_B\vec{J}, \tag{3.2.10}$$

where g is the Landé g-factor defined as

$$g = 1 + \frac{J(J+1) + S(S+1) - L(L+1)}{2J(J+1)}, \tag{3.2.11}$$

where J, L and S are the corresponding quantum numbers to operators $\vec{J}$, $\vec{L}$ and $\vec{S}$. The magnitude of μ_J can be obtained using the expression

$$\mu_J = g\mu_B\sqrt{J(J+1)}. \tag{3.2.12}$$

The parameter g characterizes the state of an atom. A g value of 1 is associated with pure orbital moments whilst that of $g = 2$ is for pure spin moment. Any g-value ranging between 1 and 2 are associated with a complicated spin-orbit interaction in an atom.

3.2.1 Magnetisation

Transitional and rare earth elements of partially filled electron shells exhibit net magnetic moments. In the presence of an external magnetic field (B), the net magnetic moment from all contributing electrons within an atom in a material per unit volume (V) is referred to as the magnetization ($\vec{M}$), mathematically expressed as

$$\vec{M} = \frac{1}{V}\sum_{i=1}^{N}\vec{\mu_i}. \tag{3.2.13}$$

The $\vec{M}$ represented by equation 3.2.13 is for homogeneously magnetized isotropic materials of volume (V). However, in a non-homogeneous systems, the magnetic moment may vary, hence equation 3.2.13 can be rewritten as

$$\vec{M} = \sum_{i=1}^{N} \frac{d\vec{\mu_i}}{dV}. \tag{3.2.14}$$

In practice $\vec{M}$ is investigated with varying temperature and applied external magnetic field. However, equations 3.2.13 and 3.2.14 have volume dependency. This is not usually useful since volume (V) is affected by thermal expansion and magnetostriction [39]. Therefore, magnetization is redefined in a more reliable way as

$$\vec{\sigma} = \frac{1}{m} \sum_{i=1}^{N} \vec{\mu_i}. \tag{3.2.15}$$

The degree of change in magnetization of a material under an external magnetic field (B) is known as the magnetic susceptibility and can be expressed as

$$\chi_m = \frac{\mu_0 M}{B}, \tag{3.2.16}$$

where μ_0 is the magnetic permeability of free space. Magnetic susceptibility is useful in classifying different types of magnetic behaviors in materials.

3.3 Types of magnetism in solids

Magnetic materials can grouped into different magnetic classes depending on the presence and ordering of magnetic moments and temperature dependence of the magnetic susceptibility. Figure 3.2 illustrate ordering of magnetic moments and their associated ideal hysteresis loops for different classes of magnetic behavior. A material that is easily magnetized and demagnetized is referred to as a soft magnetic material. A material that is difficult to demagnetize is called a hard or permanent magnetic material. The two most common types of magnetism are diamagnetism and paramagnetism which account for most elements of the periodic table at room temperature. The concept behind paramagnetism is explained by Langevin's theory [39]. From a magnetic point of view solids can be divided into two types of magnetism which include materials that do not exhibit any spontaneous magnetization in the absence of an external magnetic field and those

that do. Spontaneous magnetization exists in ferromagnetic, anti-ferromagnetic materials and ferrimagnetic materials. The concept behind these types of classifications are well explained by Weber's (1852) and Ewin's (1890) molecular theory and more recently by the domain theory of magnetism [43]. The mechanisms leading to spontaneous magnetization is either due to direct exchange or indirect exchange interactions [39].

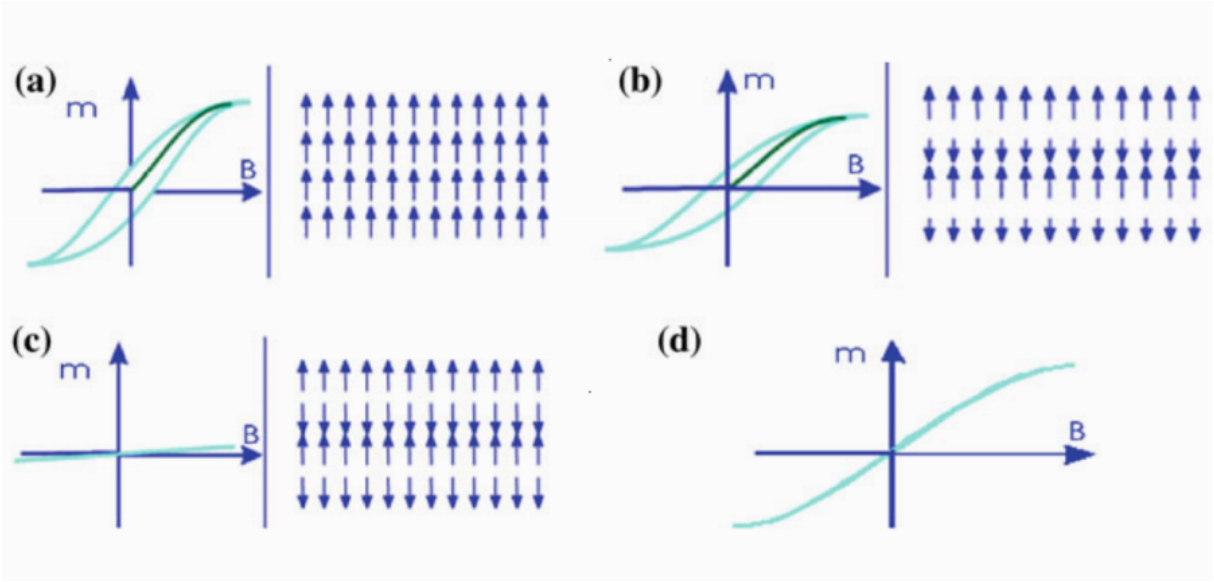

Figure 3.2: Magnetic ordering a, b, c and d represent ferromagnetic, ferrimagnetic, anti-ferromagnetic and superparamagnetic material respectively [44].

3.3.1 Larmor Diamagnetism

Diamagnetism is a very weak quantum mechanical magnetic effect that occurs in all materials in the presence of a external magnetic field. It affects all orbital electrons in an atom. Classically, in the presence of an external magnetic field any material induce magnetic moments in the direction opposite to the applied field due to Lenz's law. This produces an induced magnetization that is opposite to the direction of the applied field. This phenomena is referred to as diamagnetism and gives rise to a negative susceptibility. The diamagnetic susceptibility per unit volume can be shown to be

$$\chi_m = -\mu_0 n \frac{e^2}{6m_e} \sum_{i=1}^{Z} < r_i^2 >, \tag{3.3.1}$$

where n is the number of atoms per unit volume, Z is the atomic number and r_i^2 are the orbital radii [42]. The diamagnetic susceptibility is independent of temperature. Figure

3.3 illustrates the magnetic response for a diamagnetic material when subjected to an applied field (H) and the response of the magnetic susceptibility (χ) as a function of temperature.

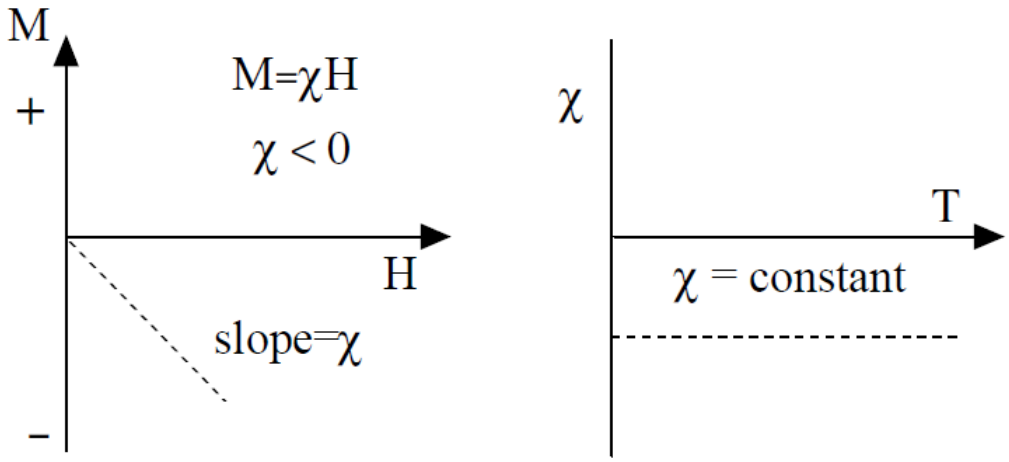

Figure 3.3: Magnetic response for a diamagnetic material in applied field (left) and magnetic susceptibility response to variation of temperature (right) [45].

3.3.2 Langevin theory of Paramagnetism

Paramagnetism exists in atomic systems with unpaired electrons with a net nonzero orbital and spin angular momenta. The magnetic moments are randomly aligned in the absence of an applied field but tend to experience a torque when subjected to an external field which aligns the magnetic moments in the direction of the applied field. Figure 3.4 illustrates the behavior of magnetic moments in the absence and presence of an external field [46]. Magnetic moments of the atom interact with the applied field but do not or weakly interact with one another. Paramagnetic materials do not retain their magnetic property when the external magnetic field is removed. The magnetic susceptibility is small, positive and varies inversely with temperature T or $T \pm \theta_p$ where θ_p is a constant. Transitional metal and rare earth ions can exhibit paramagnetic behavior. The most prominent paramagnet elements include the iron group ions consisting of unpaired 3d shells and the lanthanides which have unpaired electrons in the 4f shells.

The total magnetic moment of a material is dependent upon total angular momentum ($\vec{J}$), which is linked to the magnetic moment by a gyromagnetic ratio. However, as stated

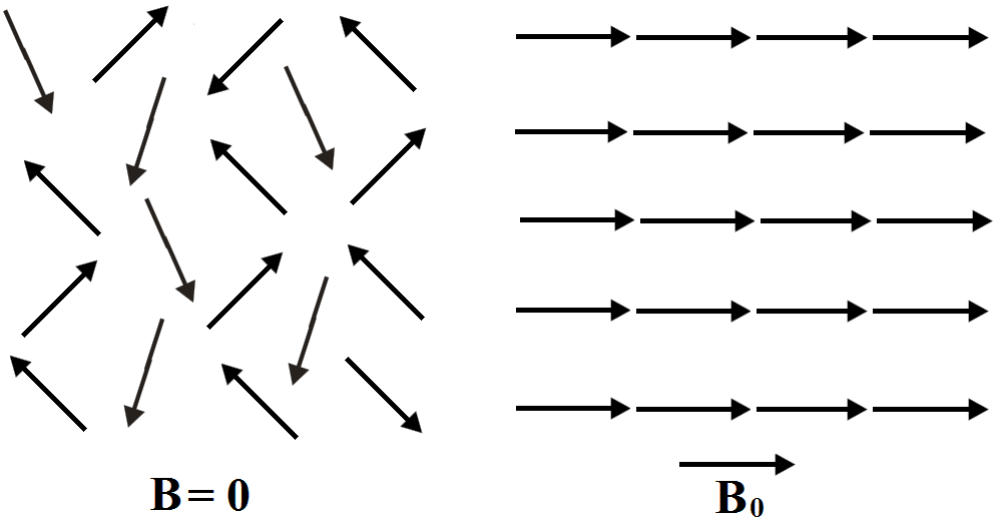

Figure 3.4: Alignment of magnetic moments in the absence and presence of external field [46].

before it can be linked in terms of Bohr magneton, given by equation 3.2.10. Placing a material with a permanent magnetic moment in a magnetic field (B_0), leads to degenerate magnetic state splitting into substates with distinct energies similar to those of the Zeeman effect. However, considering the total angular momenta of the entire atom, the magnitude of the Zeeman splitting is given by

$$E_{m_J} = m_J g \mu_B B_0, \tag{3.3.2}$$

where the magnetic quantum number $m_J = -J, -J+1, ... + J-1, +J$ relates to the total angular momentum. The probability of the relative occupation of a given state is given by the Maxwell-Boltzmann distribution expressed as

$$P(E_{m_s}) = \frac{e^{-\frac{E_{m_J}}{k_B T}}}{\sum_{m_J} e^{-\frac{E_{m_J}}{k_B T}}}, \tag{3.3.3}$$

where k_B is the Boltzmann's constant. The probability distribution compares the magnetic interaction energy (E_{m_J}) with the thermal energy ($k_B T$) for the two energy level system ($J = \frac{1}{2}$). The mean magnetic moment in the direction of the applied field can be expressed as

$$< \mu_J >_z = J g \mu_B F(J, y), \tag{3.3.4}$$

where $F(J, y)$ is the Brillouin function given by

$$F(J,y) = \Big(1 + \frac{1}{2J}\Big)\coth\Big\{\Big(1 + \frac{1}{2J}\Big)y\Big\} - \frac{1}{2J}\coth\Big\{\frac{y}{2J}\Big\}, \tag{3.3.5}$$

where y is given by $y = \frac{Jg\mu_B B_0}{K_B T}$. At high temperature approximately 300 K and low applied fields of 1 T. The Brillouin function can be reduced to

$$F(J,y) \approx \frac{y(J+1)}{3J}. \tag{3.3.6}$$

For Avogadro's number of molecules the total magnetization of the material will be given as

$$M = N_A\langle\mu_J\rangle_z = N_A J g \mu_B F(J,y). \tag{3.3.7}$$

Hence, substituting equation 3.3.6 to equation 3.3.7, the total magnetization will be given by

$$M = \frac{N_A g^2 \mu^2 J(J+1)}{3k_B T} B_0. \tag{3.3.8}$$

The magnetic susceptibility can therefore be expressed as

$$\chi_m = \frac{\mu_0 M}{B_0} = \frac{\mu_0 N_A g^2 \mu_B^2 J(J+1)}{3k_B T}. \tag{3.3.9}$$

This gives the Curie law

$$\chi_m = \frac{C}{T}, \tag{3.3.10}$$

where $C = \frac{\mu_0 N_A g^2 \mu_B^2 J(J+1)}{3k_B}$ is the Curie constant for non-interacting magnetic moments. However, if magnetic moments interact with one another, the magnetic susceptibility behavior follows the Curie-Weiss law

$$\chi_m = \frac{C}{T - \theta_p}, \tag{3.3.11}$$

where θ_p is the paramagnetic Curie temperature. The sign of θ_p determines whether the interactions between the neighboring magnetic moments are in the same direction or opposite direction. Weiss suggested the interactions could be expressed in terms of a molecular field H_m in addition to H [39, 47]. The theoretical predictions of the Curie-Weiss paramagnetic material is illustrated in Figure 3.5. There are also other types of paramagnetic behavior such as Pauli paramagnetism and Van Vleck paramagnetism [39].

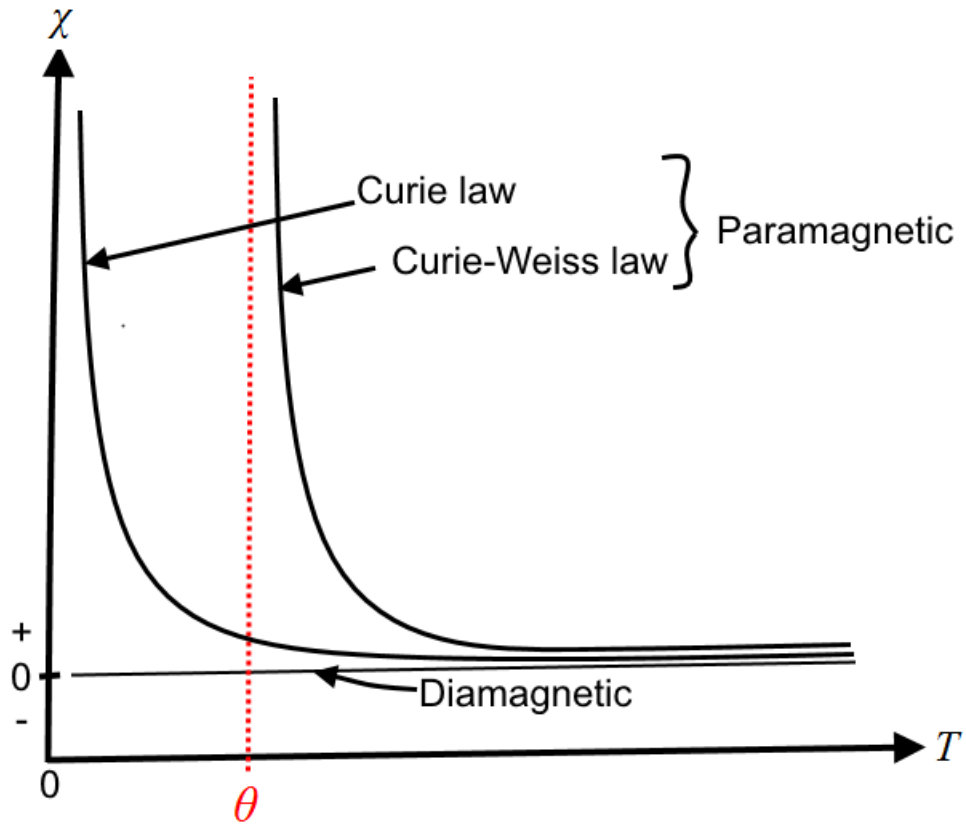

Figure 3.5: Theoretical prediction for a paramagnetic material.

3.3.3 Ferromagnetism

Ferromangetic materials exhibit a large spontaneous magnetization and unlike paramagnetic materials they are able to retain this magnetization in the absence of an external applied magnetic field. Ferromagnetism is a result of strong quantum mechanical interaction between magnetic moments. The interaction is governed by Pauli exclusion principle and Coulomb interaction. These interactions are most likely between the magnetic d-shell electrons or f-shell electrons. The spontaneous magnetization occurs below the Curie temperature (T_C). Above the T_C ferromagnetic materials follow the Weiss-Curie law of paramagnetism. Examples of ferromagnetic materials and their Curie temperatures are shown in Table 3.1. The Heisenberg model Hamiltonian describing the interaction between two magnetic atoms with spin $\vec{S}_i$ and $\vec{S}_j$ are given as

$$\mathcal{H}_{ex} = -\mathcal{J}_{ij}\vec{S}_i.\vec{S}_j, \tag{3.3.12}$$

where $\mathcal{J}_{ij}$ is the exchange integral between the i-th and j-th spins. The sign of the integral determines whether a material is ferromagnetic (FM) or anti-ferromagnetic (AFM). The

Table 3.1: Examples of Ferromagnetic materials and their Curie Temperatures.

Metal	M_S $(\mu_B/atom)$	Ions	gJ	Curie Temperature (T_C)
Iron	2.2	Fe^{3+}	5	1043
Cobalt	1.7	Co^{2+}	6	1388
Nickel	0.6	Ni^{2+}	6	627
Gadolinium	6.8	Gd^{3+}	7	292
Dysprosium	10.2	Dy^{3+}	10	88

symmetric ($\uparrow\uparrow$) spin configuration has $\mathcal{J}_{ij} > 0$ corresponding to FM behavior and the anti-symmetric ($\uparrow\downarrow$) spin configuration for $\mathcal{J}_{ij} < 0$ corresponding to AFM [39].

Exchange interactions are responsible for the existence of internal molecular field B_{int} which is used to explain FM magnetic behavior. Weiss assumed that B_{int} is proportional to the magnetization M so that internal field is given by

$$B_{int} = \lambda M, \tag{3.3.13}$$

where λ is the Weiss molecular field constant. Weiss incorporated the internal field to the paramagnetic case of magnetization i.e the paramagnetic equation 3.3.7 and assumed an effective field acting on an atomic moment of

$$B_{eff} = B_0 + B_{in} = B_0 + \lambda M, \tag{3.3.14}$$

where M is a function of temperature. The parameter y is now replaced by

$$y^{'} = \frac{Jg\mu_B B_0 + \lambda M}{k_B T}. \tag{3.3.15}$$

Hence, the magnetization can now be expressed by

$$M = N_A \langle \mu_J \rangle_z = N_A Jg\mu_B F(J, y^{'}). \tag{3.3.16}$$

In a ferromagnet the spontaneous magnetization exists even when $B_0 = 0$. In this case

$$y^{'} = \frac{Jg\mu_B \lambda M_s(0,T)}{k_B T}. \tag{3.3.17}$$

At $T = 0$ K

$$M_s(0,0) = N_A J g \mu_B, \tag{3.3.18}$$

Equations 3.3.16, 3.3.17 and 3.3.18 can be rewritten as

$$\frac{M_s(0,T)}{M_s(0,0)} = F(J, y^{'}), \tag{3.3.19}$$

and

$$\frac{M_s(0,T)}{M_s(0,0)} = \left(\frac{k_B T}{N_A J^2 g^2 \mu_B^2 \lambda}\right) y^{'}. \tag{3.3.20}$$

The solutions for equations 3.3.19 (curve 1) and 3.3.20 (curve 2) can be shown graphically as illustrated in Figure 3.6. Curve 1 is directly proportional to temperature whilst curve 2 is independent of the temperature. A rise in temperature causes an increase in the slope of curve 1 causing reduced magnetization to drop and reaches zero at some temperature T_C. The Equation 3.3.20 at the onset of spontaneous magnetization has solutions when the temperature (T) is sufficiently small, at critical temperature (T_C). Expanding the Brillouin function at small $y^{'}$ at $B_0 = 0$ gives

$$F(J, y^{'}) = \frac{(J+1)}{3J} y^{'} = \frac{k_B T_C}{N J^2 \mu_B^2 g^2 \lambda} y^{'}. \tag{3.3.21}$$

Hence, the critical temperature can be shown to be

$$T_C = \frac{1}{3k_B} J(J+1) N_A J g^2 \mu_B^2 \lambda. \tag{3.3.22}$$

At $T = T_C$, the spontaneous magnetization goes to zero as a signature of a phase transition. Materials exhibit a spontaneous magnetization at $T < T_C$. At $T = 0$ K the magnetic order is perfectly aligned. However, as the temperature increases some of the magnetic moments begin to disorder due to thermal agitation until at T_C where the disorder is complete. At $T > T_C$, a ferromagnetic material behaves as a paramagnet. The magnetic susceptibility at $T > T_C$ for a ferromagnet can be shown to be

$$\chi_m = \frac{C}{T - T_C}, \tag{3.3.23}$$

where $T_C = C\lambda$ and λ is the effective molecular field constant given by

$$\lambda = \frac{3k_B T_C}{N_A g^2 \mu_B^2 J(J+1)}. \tag{3.3.24}$$

However, in the vicinity of T_C equation 3.3.23 does not hold. What is found is that as $T \to T_C$ from above and from below, the susceptibility is given by $\chi \sim (T - T_C)^\gamma$ and $\chi \sim (T - T_C)^\beta$ respectively, where γ and β are known as critical exponents. In the Weiss mean field theory the exponents γ and β are predicted to be 1 and $\frac{1}{2}$ respectively.

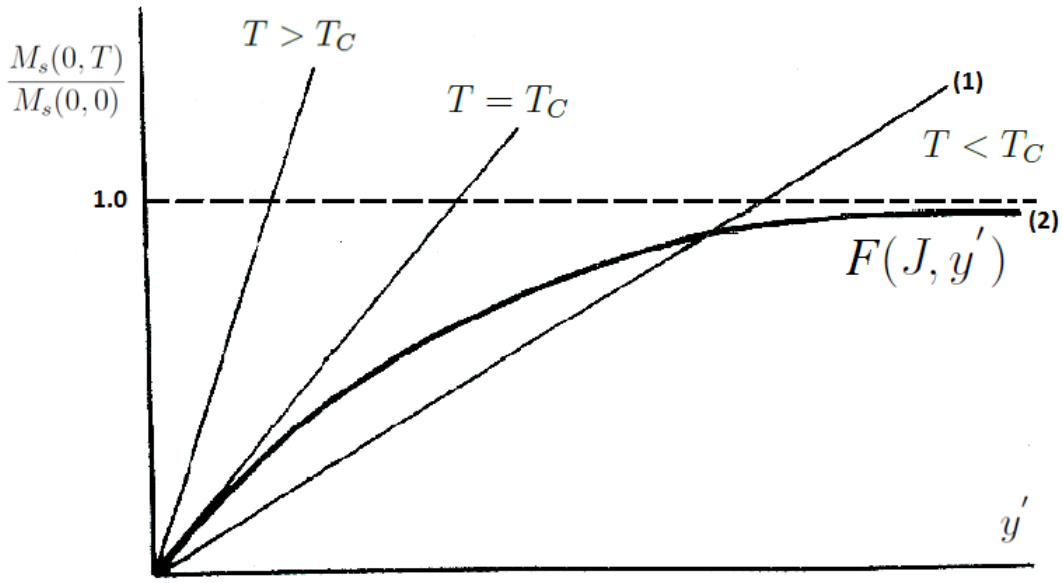

Figure 3.6: Graphical solutions for equations 3.3.19 and 3.3.20.

3.3.4 Antiferromagnetism

The exchange coupling in antiferromagnetic (AFM) material favors antiparallel spins rather than parallel alignment as previously explained for ferromagnetism. The exchange integral is negative. AFMs have small positive susceptibilities at all temperatures. However, near 0 K there many exist a small net magnetization due to the effect of spin canting [48]. AFMs have a critical temperature called Néel temperature (T_N), named after the French scientist Louis Néel who was the first to identify and explain this type of magnetic ordering in 1936. Examples of AFM materials and their corresponding T_N values include Cr (311 K), MnF_2 (67 K), NiF_2 (73 K), MnO (116 K) and FeO (198 K). Below T_N, the net magnetization is zero and for $T > T_N$ the moments are disordered and follow the

Weiss-Curie law of paramagnetism. To explain this phenomenon Néel assumed that an antiferromagnetic crystal consists of two equal and oppositely directed magnetic moments on sublattices (A and B) with internal magnetic fields at the sublattices in the presence of an external applied field given by

$$B_{in}^{A} = \lambda_{AA} M_A + \lambda_{AB} M_B + B_0 \tag{3.3.25}$$

and

$$B_{in}^{B} = \lambda_{BB} M_B + \lambda_{BA} M_A + B_0, \tag{3.3.26}$$

where the molecular field coefficients $\lambda_{i,j}$ (where i,j = A or B) represent the intrasublattice and the intersublattice molecular field coupling respectively. The magnetization of each sublattice is given by $\vec{M}_A$ and $\vec{M}_B$. The net magnetization $\vec{M} = \vec{M}_A + \vec{M}_B$ in the absence of an external field (B_0) is zero. The magnetization of each sublattice approaches zero towards T_N and the spontaneous magnetization for each magnetic sublattice is described by the Brillouin function $F(J, y)$ as

$$M_i = \frac{N_A \mu_B J}{2} F(J, y_i), \tag{3.3.27}$$

where $i = A, B$ and $y_i = \frac{Jg\mu_B}{k_B T} B_{in}^{i}$. Here the magnetization at each sublattice is $M_{AO} = -M_{BO} = \frac{N_A g \mu_B J}{2}$.

At temperatures above the Néel's temperature AFMs follow paramagnetic behavior, $M_i = \chi B_{in}^{i}$ where $\chi = \frac{C'}{T}$ and $C' = \frac{\frac{n}{2} g^2 \mu_B J(J+1)}{3k_B}$. Hence, the magnetization for $M_{A,B}$ is given by

$$M_A = (\frac{C'}{T})(\lambda_{AA} M_A + \lambda_{AB} M_B + B_0) \tag{3.3.28}$$

and

$$M_B = (\frac{C'}{T})(\lambda_{BA} M_A + \lambda_{BB} M_B + B_0). \tag{3.3.29}$$

Spontaneous magnetization for $\vec{M}_i$ occurs when equations 3.3.28 and 3.3.29 have nonzero solution in the absence of an external applied field. The Néel's temperature is obtained by setting the determinant of the coefficients of M_A and M_B to zero and can be shown to give

$$T_N = C'(\lambda_{AA} - \lambda_{AB}). \tag{3.3.30}$$

The susceptibility for the entire system is given by $\chi = \frac{(M_A+M_B)}{B_0}$ which can be easily shown to give the Curie-Weiss law

$$\chi = \frac{C}{T - \theta_p}, \tag{3.3.31}$$

where θ_p is the paramagnetic Curie temperature shown to be $\theta_p = C' = (\lambda_{AA} + \lambda_{AB})$.

The Néel Temperature and the paramagnetic Curie temperature are related by

$$T_N = \frac{\lambda_{AA} - \lambda_{AB}}{\lambda_{AA} + \lambda_{AB}}\theta_p. \tag{3.3.32}$$

The magnetic susceptibility for $T < T_N$ is dependent on the direction of B_0 in relation to the antiferromagnetic axis along which the sublattices A and B lie. For powdered materials, two components contribute to the total magnetic susceptibility, $\chi_{\shortparallel}$ and $\chi_\perp$ which are parallel and perpendicular components to the direction of external field (B_0) respectively. The total magnetic susceptibility is given by

$$\chi_{T<T_N} = \frac{2}{3}\chi_\perp + \frac{1}{3}\chi_{\shortparallel}. \tag{3.3.33}$$

Figure 3.7 shows the magnetic response in relation to temperature. It is observed from this plot that $\chi_\perp$ is independent of temperature whilst $\chi_{\shortparallel}$ increases from zero at 0 K to reach the paramagnetic value at T_N. At $M_i = 0$ where the Brillion function is $F(J, y) = \left(\frac{J+1}{3J}\right)y$, the magnetic susceptibility adopts the Curie-Weiss behavior, since $T_N = -\theta_p = -C'\lambda_{AB}$.

3.3.5 Ferrimagnetism

Ferrimagnetic materials exhibit spontaneous magnetization due to unequal antiparallel alignment of magnetic moments between two magnetic sublittaces, similar to AFM. However, unlike AFM, a net magnetic moment arises because of unequal magnetic moments on two sublattaces. Ferrimagnetic materials have non zero magnetization below the Curie temperature similar to that of ferromagnetic material and above the Curie temperature they become paramagnetic. Néel explained ferrimagnetism using mean field theory with

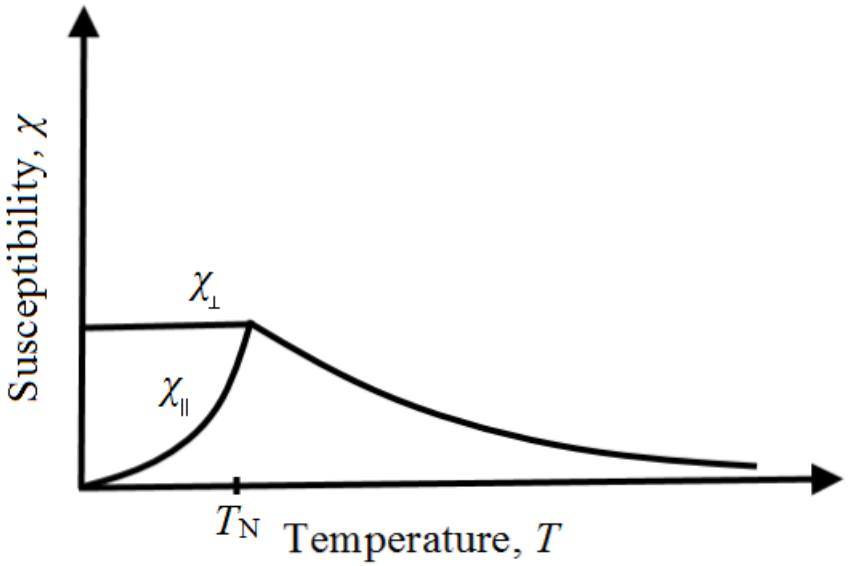

Figure 3.7: Magnetic response to temperature [39].

internal field in the presences of an external field for two sublittices expressed as in equation 3.3.33 for antiferromagnetism. However, the net magnetization $\vec{M} = \vec{M}_A + \vec{M}_B$ is non zero, hence $\vec{M}_A \neq \vec{M}_B$. The Weiss coefficients $\lambda_{AA} \neq \lambda_{BB}$ and λ_{AB} is the negative exchange parameter. Ferrimagnets behave similar to antiferromagnetic materials when M_A = - M_B at a compensate temperature, T_{comp} [39]. At T_C, the materials loses their magnetization. At temperatures above T_C, the magnetization for each sublattice ($M_i = \chi_i H_i^{in}$) is given by

$$M_A = \left(\frac{C_A}{T}\right)\left(\lambda_{AA}M_A + \lambda_{AB}M_B + B_0\right) \tag{3.3.34}$$

and

$$M_B = \left(\frac{C_B}{T}\right)\left(\lambda_{AB}M_A + \lambda_{BB}M_B + B_0\right) \tag{3.3.35}$$

where $C_i = \frac{\mu_0 n_i g^2 \mu_B^2 J(J+1)}{3k_B}$ and n_i is the number of atoms per cubic meter on a particular sublattice. Spontaneous magnetization occurs when there is a non-zero solution for equations 3.3.34 and 3.3.35 in zero applied field. The Curie temperature can be shown to be

$$T_C = \frac{1}{2}\left[\left(C_A\lambda_{AA} + C_B\lambda_{BB}\right) + \sqrt{\left(C_A\lambda_{AA} + C_B\lambda_{BB}\right)^2 + 4C_AC_B\lambda_{AB}^2}\right]. \tag{3.3.36}$$

The magnetic susceptibility above T_C can be shown to be

$$\frac{1}{\chi} = \frac{T-\theta}{C_A - C_B} - \frac{C''}{T-\theta'}, \tag{3.3.37}$$

where C'', θ' and θ are the microscopic parameters [39]. The magnetic susceptibility behavior as function of temperature is illustrated in Figure 3.8.

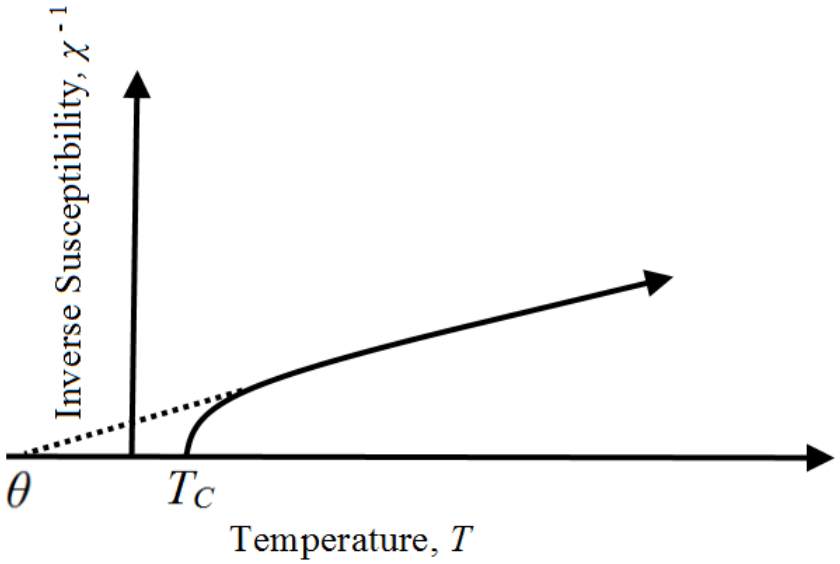

Figure 3.8: Magnetic susceptibility response for ferrimagnets above T_C [39].

3.3.6 Superparamagnetism

The magnetic properties of an assembly of single domain particles is studied within the framework of the so-called superparamagnetic theory. This type of magnetic behaviour is observed in small ferromagnetic or ferrimagnetic nanoparticles. Frenkel and Dorfomarn [49] were the first to predict that a particle of a ferromagnetic material, below a critical particle size would consist of a single magnetic domain [49]. This critical particle size was observed to be below 50 nm [50]. The single domain nano-particles consists of uni-axial magnetic anisotropy and are said to consistently vibrate at random due to thermal fluctuations. It is therefore possible for these nanoparticles to obtain enough thermal energy from these vibrations for its magnetization field to reverse [51]. Thermal energy can therefore overcome an energy barrier (ΔE) for the magnetization to be reversed. The energy barrier is given by

$$\Delta E = K_{ans} V sin^2\theta, \tag{3.3.38}$$

where K_{ans} is the anisotropy constant, V is the volume of the nanoparticle and θ is the angle between the moment and the easy axis. The average time for such a magnetic reversal to occur is called Néel relaxation time and is a function of energy barrier and temperature. Quantitatively this is expressed by the Néel - Brown model as

$$\tau_N = \tau_m exp\Big(\frac{\Delta E}{k_B T}\Big), \tag{3.3.39}$$

where τ_m is the average measurement time of the probed material and is reported to be in the range $(10^{-9} - 10^{-10})$ s [52]. A blocked state and a superparamagnetic state occurrences are governed by the relation between τ_m and τ_N. A blocked state occurs when $\tau_m << \tau_N$ at temperatures below the blocking temperature (T_B). In this state the magnetic ordering is similar to that of ferromagnetism. Alternatively, at temperatures above the T_B that is at $\tau_m >> \tau_N$, it is possible to observe magnetic reversal within the experimental time frame. This is called the superparamagnetic state. The blocking temperature separating the two states is expressed as

$$T_B = \frac{\Delta E}{k_B ln\Big(\frac{\tau_N}{\tau_m}\Big)}. \tag{3.3.40}$$

Essentially, the superparamagnetic state has a probability of occurrence anywhere between $(T_B < T < T_C)$ depending on the material. Measurement time has a huge influence in determining which state is observed. Some typical measurement times for DC magnetisation, AC susceptibility and Mössbauer spectroscopy have been reported to be 100 s, $(10^{-1} - 10^{-}5)$ s and $(10^{-7} - 10^{-9})$ s respectively. In the absence of an applied field the net magnetization is zero whilst in the presence of an applied external field a non-zero net magnetization exists due to moments aligning in the direction of the applied field similar to paramagnetism. The net magnetization can be expressed in terms of the classical Langevin function $L(x)$ to give

$$M = n\mu\bigg(cothx - \frac{1}{x}\bigg), \tag{3.3.41}$$

where $x = \frac{\mu B_0}{k_B T}$ and $n\mu$ is the maximum magnetization value reached by the entire system which corresponds to all or a fraction of the magnetic moments aligned in the direction of the applied field [51, 39]. The corresponding reduced magnetization is expressed as

$$\frac{M(T)}{M_S} = L\left(\frac{\mu B_0}{k_B T}\right), \tag{3.3.42}$$

where L is the Langevin function. A plot of the reduced magnetization against $\frac{B_0}{T}$ can be used to verify superparamagnetism [42]. For a superparamagnetic material the plots are expected to follow the Langevin's universal curve provided the measurement temperature are above the irreversibility temperature, T_{irr} [42]. The magnetic susceptibility which is related to the well known Curie law can be obtained by expansion of the Langevin function as a power series given by

$$\chi_{sp} = \frac{M_s^2 V}{3k_B T}. \tag{3.3.43}$$

3.3.7 Magnetization processes

The magnetization processes that give rise to magnetic hysteresis loops and their shapes is a direct consequence of the variety of possible magnetic domain structures. Magnetic domains are a result of the balancing act of several competing energy terms such as exchange energy [53], magnetocrystalline anisotropy [42] and magnetostatic energy [54, 39]. In addition the magnetic moments are coupled to the external field by the energy $-\vec{\mu}.\vec{B}$ which favor domain magnetization in the direction of $\vec{B}$. By changing $\vec{B}$ with time, the energy is altered and a rearrangement of the domain structure occurs, mainly through motion of domain walls. The domain magnetization pointing in the direction of $\vec{B}$ is energetically favored and expands at the expense of the other domains. At high $\vec{B}$, the material is magnetized everywhere and the moments align in one direction. This is viewed as one big domain occupying the whole specimen. At this point the average magnetization becomes close to the spontaneous magnetization. When the field is reversed, domains of reversed magnetization are formed, which progressively increases in size through domain wall motion until a single domain of reversed magnetization is formed. In the presence of an external field, uniaxial nanoparticles (> 100 nm) show spin rotation whilst those of bulk react by the movement of their domain walls. The magnetization process is well described by the Stoner-Wohlforth model [55]. The model assumes a single domain ellipsoidal with uniaxial anisotropy, uniformily magnetized as shown in Figure 3.9. The

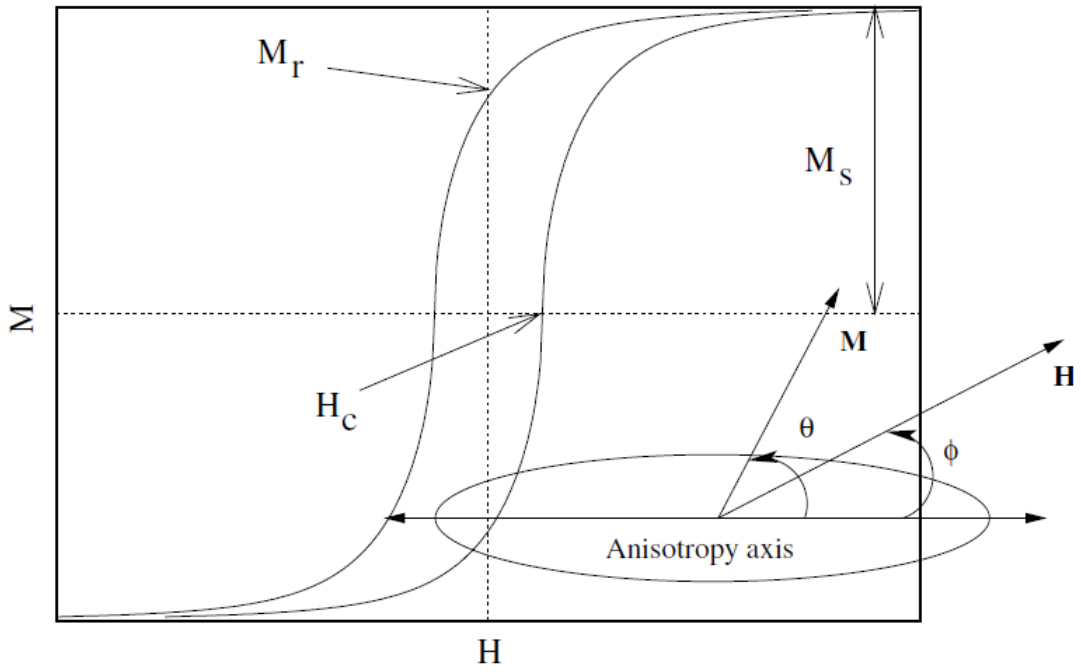

Figure 3.9: Single domain hysteresis loop at arbitrary ϕ between the magnetic field and the uniaxial anisotropy [55].

single moment (M) is subjected to two competing alignment forces, one due to uniaxial anisotropy and the other due to an external field. Therefore, the total energy is the anisotropy and Zeeman energies. At T=0 K the energy per unit volume is given by

$$E = E_A + E_Z = Ksin^2\theta - HMcos(\theta - \phi) \tag{3.3.44}$$

where K is the magnetic uniaxial anisotropy constant [39]. The moments prefer directions in which the energy density is minimized. Hysteresis occurs when equation 3.3.44 has two minima. The area under the hysteresis curve represents energy loss for a FM. In the presence of an applied field the magnetization of the initial magnetization curve is given by

$$M = \chi_j H + \nu H^2, \tag{3.3.45}$$

where χ_j is the reversible initial susceptibility and ν is the irreversible response to applied field. At high applied field, the curve approaches a spontaneous magnetization M_S according to the empirical expression

$$M = M_S\left(1 - \frac{a}{H} - \frac{b}{H^2} - ....\right) + \chi_0 H, \tag{3.3.46}$$

where a and b are parameters due to defects and uniform magnetocrystalline anisotropy respectively. χ_0 is a high field susceptibility due to para-processes [39]. Hysteresis loops may take different shapes. The prime characterization parameters for loop properties are the remanent magnetization (M_r) and the coercive field (H_C) as shown in Figure 3.9. M_r is the magnetization that remains when the field applied to a material is removed. Various geometrical and structural defects may play a role in decreasing M_r well below M_S. The field needed to bring the magnetization from the remanent value to zero is referred to as the coercive field. The coercive field measures the order of magnitude of the fields that must be applied to a material in order to reverse its magnetization. It is common to classify materials as soft and hard magnetic materials based on the values of M_r and H_C. Soft magnetic materials can easily be magnetized and demagnetized. The main characteristics of soft magnetic material includes high magnetic saturation and permeability, low coercivity and low energy loss making them suitable for applications such as in electric motors, DC-DC Converters and electromagnet pole-pieces. Hard magnetic materials are those that do not demagnetize easily. These materials are characterized by high coercivity H_C and M_r values. Such materials are ideal for permanent magnets.

Chapter 4

Mössbauer spectroscopy

Mössbauer spectroscopy (MS) is a versatile technique which is based on the principle of the Mössbauer effect. The Mössbauer effect is observed only for γ rays of sufficiently low energy. The Mössbauer effect involves recoil-free emission of gamma radiation by excited nuclei which are inturn resonantly absorbed by identical nuclei in their ground state. This was experimentally discovered by Roudolf L. Mössbauer in 1957 [56]. The spectroscopy gives information at an atomic scale by precise measurement of the emitted and absorbed γ ray energy. Mössbauer spectroscopy measures γ-ray energies with an accuracy of 1 part in 10^{12}. The difference in γ-ray energies emitted can be of the order of approximately 10^{-8} eV [57].

A number of isotopes such as ^{57}Fe, ^{61}Ni, ^{119}Sn, ^{151}Eu, ^{161}Dy and ^{191}Ir show the Mössbauer effect [57, 58]. However, most published works have reported the use of mainly ^{57}Fe and ^{119}Sn. This is mainly due to the low energies of the nuclear transitions for both ^{57}Fe and ^{119}Sn, which allow measurements at ambient temperature, and also the relatively long half-life of the respective ^{57}Co and ^{57}Sn parent nuclides feeding the nuclear transitions which allow the use of a Mössbauer source for several months. In the present work ^{57}Fe Mössbauer spectroscopy was used to study our samples. Figure 4.1 shows the decay scheme of an isolated ^{57}Fe nucleus. However, in nature, isolated atoms or nuclei of ^{57}Fe do not exist. ^{57}Fe atoms only exist in roughly about 2.12 % of iron containing materials.

The ground state of an isolated ^{57}Fe nucleus splits into two substates M_I=($+\frac{1}{2}$,$-\frac{1}{2}$) and the splitting energy is of the order of 10^{-8} eV. The first excited state $I = \frac{3}{2}$ of an isolated

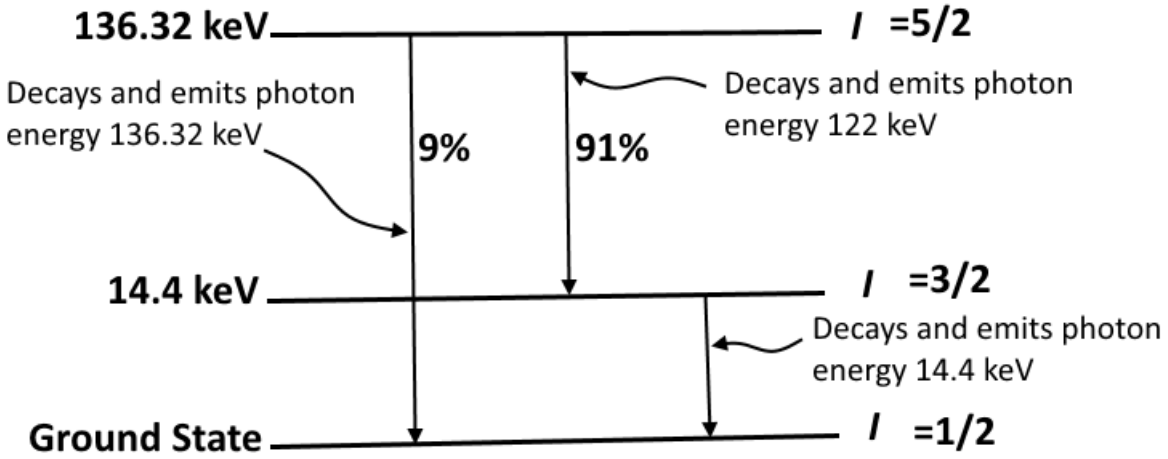

Figure 4.1: Decay scheme of an isolated ^{57}Fe nucleus energy levels.

^{57}Fe nucleus splits into four substates M_I=($\frac{3}{2}$,$\frac{1}{2}$,$-\frac{1}{2}$). The ground state with $I = \frac{1}{2}$ splits into M_I=($+\frac{1}{2}$,$-\frac{1}{2}$) states that can interchange depending on the material. The nuclear energy level splitting for an iron piece is due to ferromagnetic interaction that generates an internal magnetic field. In ferromagnetic material there is also a shift due to atomic electrons which interact with the nucleus more especially the S-electrons because they overlap with the nucleus. However, for materials which are non-ferromagnetic, the energy levels are shifted due to interaction from the solid in which the ^{57}Fe isotopes are embedded. The shifts and splitting of the energy levels in ^{57}Fe can serve as an indicator of the local environment of the isotopes. Experimentally the Mössbauer spectrum is presented as a plot of transmitted intensity of the γ-rays against the velocity of the source of γ-rays.

4.1 Principle of Mössbauer effect

The general idea of ^{57}Fe Mössbauer spectroscopy is to measure change in energy levels precisely to obtain information about the environment surrounding the ^{57}Fe isotopes. The commonly used radioactive source for ^{57}Fe Mössbauer spectroscopy is ^{57}Co which is usually embedded in Rhodium matrix. Rhodium is a cubic and non-ferromagnetic material. Figure 4.2 shows a decay scheme of ^{57}Co. ^{57}Co decays to an excited state of ^{57}Fe by electron capture with a half life of 270 days. The exited state decays in a cascade of γ-rays to the stable ground state. The decay from I= $\frac{3}{2}$ to I= $\frac{1}{2}$ emits 14.4 keV γ-rays with a half life 100 ns. This is the γ-ray energy used for Mössbauer spectroscopy since it easier to detect rather than the higher energy photons.

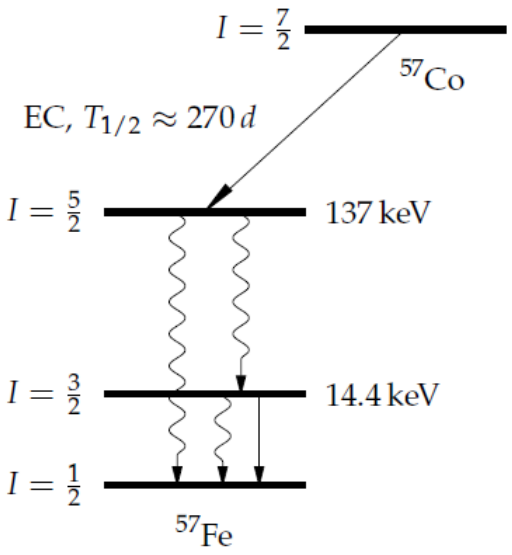

Figure 4.2: Decay scheme of ^{57}Co to unstable ^{57}Fe by electron capture [59].

The Mössbauer spectroscopy consists of a source, absorber detector and instrumentation for recording and storage of γ-rays transmitted intensity of γ-rays through the absorber. The transmitted intensity depends on resonant emission and absorption of γ-rays. For a free nucleus resonant absorption was very difficult to observe up until the discovery of the suppression of recoil energy losses in solids by Mössbauer. The main difficulty in the detection of resonant absorption was due to the momentum recoil during emission or adsorption of γ-rays. This leads to some energy loss via kinetic energy of nuclei that recoil causing the emitted photon to be slightly lower than energy required for resonant absorption. In fact, for resonant absorption the photon energy must be slightly higher than the resonance energy because some kinetic recoil energy may be imparted to the absorbing nucleus. A photon with energy E_γ has momentum $P = \frac{E_\gamma}{c}$ where c is the speed of light. For an isolated nucleus it can be shown using conservation of momentum that the total nuclei transition energy E_0 is divided between the emitted photon and the nucleus that recoils with energy E_R given by

$$E_R = \frac{E_\gamma^2}{2m_{nu}c^2}, \tag{4.1.1}$$

where m_{nu} is the mass of the nucleus [56]. Conservation of energy informs that the γ-ray energy emitted is the same as that absorbed (E_γ=$E_0 - E_R$). This leads to the conclusion

that the energy of an emitted photon and a photon that is absorbed are different by energy $2E_R$ as shown in Figure 4.3. The natural linewidth Γ of the emission and absorption lines is six orders of magnitude smaller than the natural width of the emission and adsorption line of the recoil energy given by the 14.4 keV nuclear transition. This implies that the separation between the adsorption and the emission energies is too large for resonant absorption of the γ-rays for free nuclei [60]. However, a source can be constrained to minimize recoil energy to negligible quantity if the nuclei are bound in a crystal lattice. This is because the mass in equation 4.1.1 is replaced by the mass of the entire crystal.

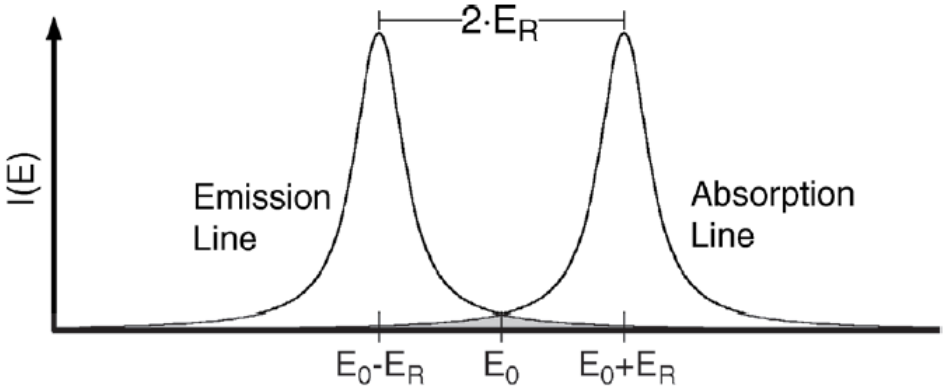

Figure 4.3: Recoil effect caused by emission and absorption of photons in isolated nuclei [60].

In the case of ^{57}Co source the atoms are embedded in Rh matrix. Hence the whole crystal lattice of Rh is assumed to recoil when emission of a γ-ray occurs. The fraction for recoilless emission and absorption is found to be

$$f = exp\bigg(- \frac{E_\gamma^2 < x^2 >}{(\hbar c)^2}\bigg), \tag{4.1.2}$$

where $< x^2 >$ is the mean square thermal displacement of the emitting nucleus in the direction of the γ-ray and $\hbar = \frac{h}{2\pi}$ where h is the Planck's constant [61]. The γ-rays being absorbed has energy:

$$E_\gamma = E_{source}\bigg(1 + \frac{v}{c}\bigg), \tag{4.1.3}$$

where v is the variable velocity changing from some v_{max} to v_{min}. According to Heisenberg uncertainty principle, the energy emission line width Γ depends on the average lifetime of the nuclear excited state τ and is given by

$$\Gamma = \frac{\hbar}{\tau}. \tag{4.1.4}$$

Resonance absorption does not accur if $E_R > \Gamma$. However, by Doppler shifting the γ ray energy resonant absorption can occur. The source is vibrated at maximum velocity of ± 10 mm/s. Hence, the γ-ray energy is Doppler shifted by

$$\delta E = E_\gamma \frac{v}{c}, \tag{4.1.5}$$

where E_γ is the energy of the γ-ray [58]. The source vibrates as a function of time. Its velocity changes and the energy of the γ-ray also changes from some minimum to maximum see equation 4.1.3. ^{57}Fe energy level is shifted due to Rh environment. γ-ray energy emitted by a source can be shown to be $E_{source} = E_{excited} - E_{ground}$ and the γ-ray energy absorbed is given by $E_{absorbed} = E'_{excited} - E'_{ground}$. Figure 4.4 shows resonant absorption of emitted γ-rays. The shift of the source and absorber are different in the order of 10^{-8}eV. The source is moving in a periodic motion which increases the probability of the source γ rays being absorbed by the absorber (sample of interest). Due to the Doppler shift, at a certain point in time the energy difference of $E_{source} = E_{absorber}$. At this point the detector records a velocity drop due to the resonance absorption by the material being investigated but for other velocities where $E_{source} \neq E_{absorber}$ the γ-rays pass through the sample and higher counts are observed from detector.

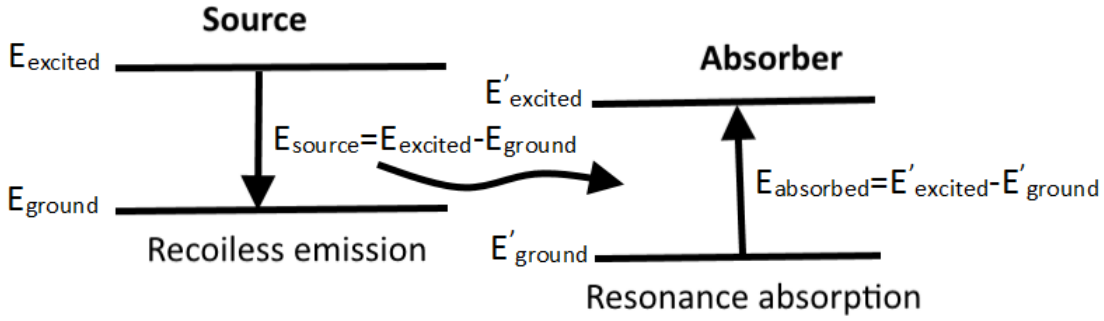

Figure 4.4: Schematic diagram showing resonance absorption of γ rays.

4.2 Hyperfine interactions

The interaction between a nucleus and its surroundings is known as hyperfine interaction. These interactions are very small in comparison with energy levels of the nucleus. How-

ever, the extreme energy resolution of the Mössbauer effect enables these interactions to be observed. The hyperfine interactions may shift energy levels or lift their degeneracy. These variations affect the shape of a Mössbauer spectrum. Hyperfine interaction can reveal information about the electronic and magnetic states of a material. This information is extracted from the hyperfine parameters such as isomer shift, quadrupole splitting and magnetic hyperfine interactions which are generated via processing software such as recoil or Mosswinn.

4.2.1 Isomer shift

The electric monopole interaction, which causes a shift of the resonance line is referred to as isomer shift. Electric monopole interaction causing the shift are part of Coulomb interaction between the nuclear charge distribution of finite size and the negatively charge s-electrons. Nuclei of the same mass and charge but at different nuclear states are referred to as isomers, hence the name name isomer shift. The reason for the shift is given by different radii of the nucleus in the excited and the ground state [60]. In ^{57}Fe MS, the isomer shift for Fe^{2+} ions is in the range (0.6-1.7) mm/s, whereas for Fe^{3+} ions the range is between (0.1-0.5) mm/s [62]. The difference in the s-electron environment between the source and absorber produces a shift in the resonant energy of the transition. This shifts the whole spectrum positively or negatively depending upon the s-electron density. The shift cannot be measured directly. It is quoted relative to a known absorber for example in ^{57}Fe Mössbauer spectroscopy it is quoted relative to alpha-iron absorber at room temperature. The expression for the isomer shift can be derived based on the difference in nuclear energy levels between the source and absorber and can be shown to be

$$\delta = \left(\frac{c}{E_0}\right)\frac{2\pi Z e^2}{3}\langle \Delta r^2 \rangle \left[|\Psi_A(0)|^2 - |\Psi_S(0)|^2 \right], \tag{4.2.1}$$

where $\langle \Delta r^2 \rangle$ is the difference of the average squared nuclear radii of the excited and ground states and $\left[|\Psi_A(0)|^2 - |\Psi_S(0)|^2 \right]$ is the difference in the electron densities at the nucleus for absorber and source [60].

4.2.2 Quadrupole splitting

The interaction between the nuclear quadrupole moment and the electric field gradient (EFG), generated by the charge distribution of the valance electrons or by the environment of the Mössbauer atoms in a solid produces the electric quadrupole splitting. Any nucleus with a spin quantum number $I > \frac{1}{2}$ has a non-spherical charge distribution which leads to a quadrupole term [63]. This causes a splitting of the Mössbauer line as show in Figure 4.5. The excited state with $I = \frac{3}{2}$ splits into two substates $M_I = \pm\frac{3}{2}$ and $M_I = \pm\frac{1}{2}$ where M_I is the magnetic quantum number. The expression for E_Q which is dependent on nuclear spin on the quadrupole moment of the V_{zz} component of the EFG with nuclear operator and asymmetry parameter of EFG can be derived from perturbing Hamiltonian [63]. $\triangle E_Q$ which is associated with the splitting of the energy levels can be shown to be related to the spectroscopy quadrupole moment of the V_{zz} component of the electric field gradient which can be shown to be

$$\triangle E_Q = E_Q\left(\pm\frac{3}{2}\right) - E_Q\left(\pm\frac{1}{2}\right) = \frac{eQV_{zz}}{2}. \tag{4.2.2}$$

The quadrupole splitting can reveal information on the symmetry of the surrounding nuclei environment and the magnetic behavior of the material under investigation.

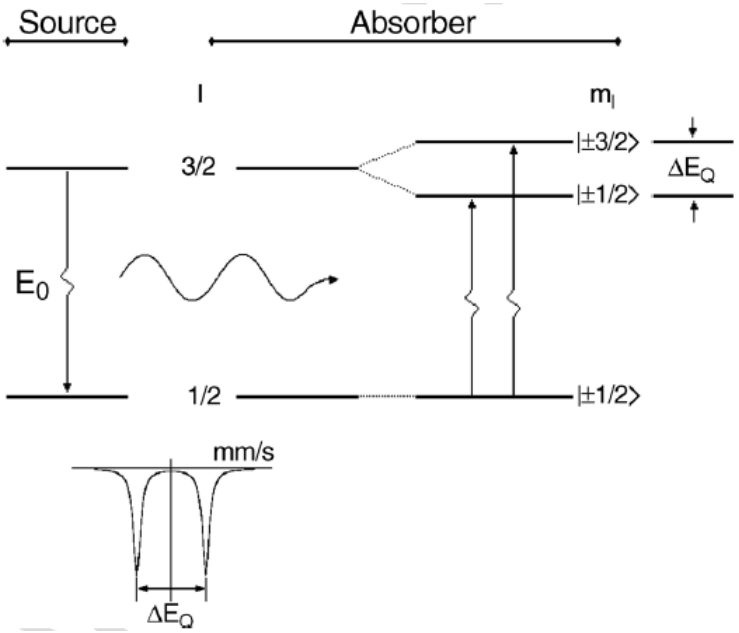

Figure 4.5: Quadrupole splitting of the nuclear energy levels for ^{57}Fe.

4.2.3 Magnetic hyperfine interaction

The nuclear energy levels in the presence of an internal magnetic field split due to nuclear magnetic dipole $\vec{\mu}$ interacting with the magnetic field $\vec{H}$. A nucleus with spin quantum number $I = 0$ has no Zeeman splitting whilst a nucleus with spin quantum number $I > 0$ has magnetic hyperfine dipole interaction given by the Hamiltonian

$$\mathcal{H} = -\vec{\mu}.\vec{H} = -g_N \mu_N \vec{I}.\vec{H}, \tag{4.2.3}$$

where μ_N is the nuclear Bohr magneton, $\vec{\mu}$ is the nuclear magnetic moment and g is the nuclear g-factor. The energy levels can be derived from the eigenvalues of the Hamiltonian and are expressed as

$$E_m = -g_N \mu_N H M_I, \tag{4.2.4}$$

where M_I is the magnetic quantum number. The magnetic field splits the nuclear level of spin I into $(2I+1)$ equally spaced non-degenerate sub-levels [58]. The Zeeman splitting obeying the selection rule of $\triangle M_I = 0, \pm 1$ produce a resultant spectrum called a sextet as shown in Figure 4.6.

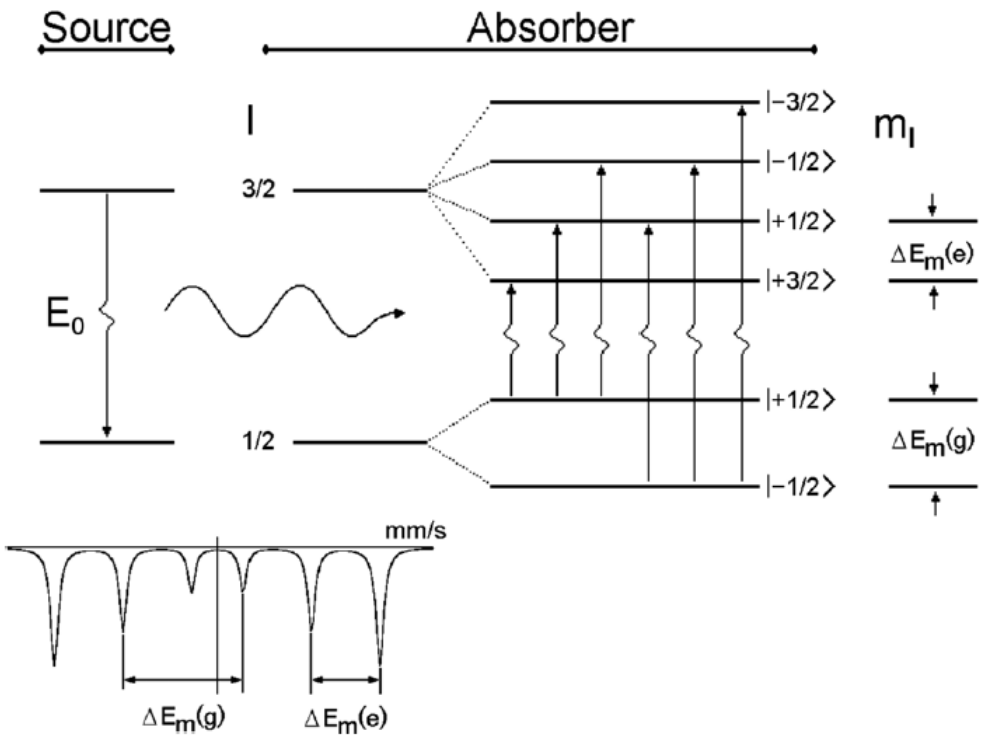

Figure 4.6: Magnetic splitting of the nuclear energy levels in ^{57}Fe.

Chapter 5

Experimental methods

5.1 Synthesis techniques

Several different synthesis techniques are currently in use for synthesis of nano-materials. However, cost efficient synthesis methods targeting specific properties for particular application are also in high demand. Many routes can be used to synthesize perovskite materials, including solid state reaction, co-precipitate, hydrothermal, spray and freeze drying, co-precipitate and sol gel [64]. It is well known that synthesis routes have vital influence on the physical and chemical properties of the final product. A unique microstructure is obtained by each synthesis method and this always has an impact on the properties of a material [65]. All synthesis techniques have advantages and disadvantages. In this project high energy ball milling (HEBM) and high temperature treatment was utilized to synthesis the materials.

5.1.1 High-energy ball milling

HEBM is the most frequently used system for mechanosynthesis. This is attributed to the fact that only minimal amount of powder is required for synthesis. Hence, it is suitable for laboratory research purposes. The Retsch planetary ball mill used in this study Figure 5.1 consists of one turning disc and four vial jars. The disc turns in one direction while the vial jars rotate in the opposite direction. Centrifugal forces alternatively act in like but opposite direction are created by both the rotation of the vial jars around its own axis together with the rotation of the turning disc as illustrated in Figure 5.2. This causes the milling balls to rise up inside the walls of the vial jar in the direction of the rotating

vial. The milling balls cascade from near the top of the vial inner chamber and collide against the opposite inside wall in the process crushing solid particles between the balls [66]. Other ball motions include cascading and centrifugal forces are illustrated in Figure 5.3.

Figure 5.1: Retsch planetary ball mill (type PM 400 MA), Condensed Matter Physics Laboratory, Westville campus.

Mechanical processes that take place during HEBM involve deformation, fracture and cold welding until there is no further physical improvement in the final product. These processes are a consequence of ball-wall and ball-ball impacts. Earliest developments of this method was only used for particle size reduction until Carry Lee reported the synthesis of halogen and metal from grinding of halides of metals such as gold, silver, platinum and mercury [67]. Mechanosynthesis process uses mechanical energy to break bonds between atoms and activate chemical reaction [68]. A number of important parameters such as milling atmosphere, speed, time, ball to mass ratio and the extent of filling up the milling vial jars influence the quality of the final product.

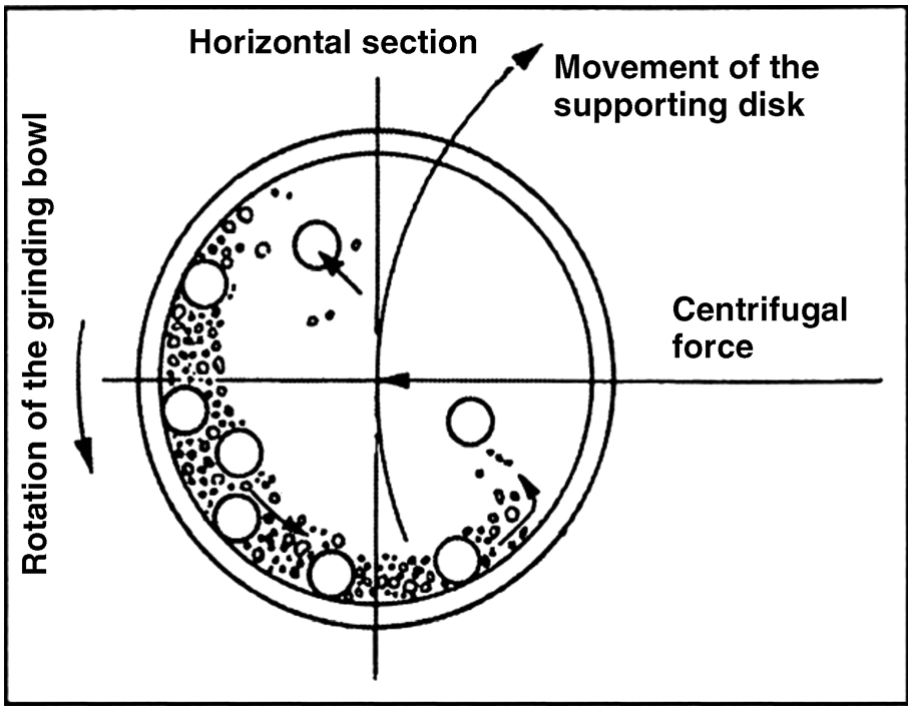

Figure 5.2: A schematic view showing rotation of vial jars about central disc in a planetry ball mill [66].

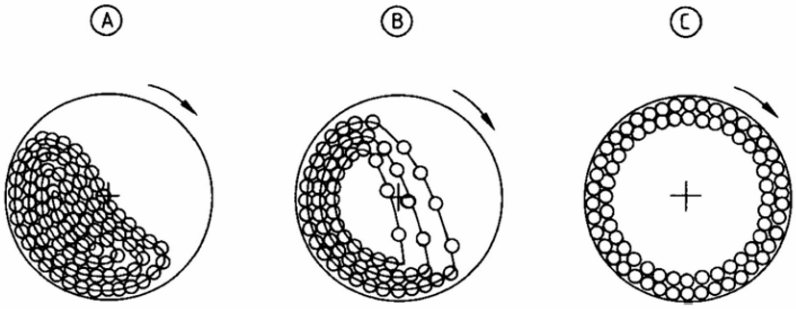

Figure 5.3: (a), (b) and (c) shows cascading, falling and centrifugal motion of milling balls respectively [66].

Mechanical milling is a cost effective method for producing a wide range of nano-materials. Numerous researchers have used mechanical milling to synthesize nano-structured perovskites [69, 70, 71]. The synthesis for the present materials was conducted using a Retsch planetary ball mill in conjunction with a high temperature thermal annealing in a furnace. Precursors were mixed according to the required stoichiometry and milled to initiate chemical reaction and structural changes. Stainless steel balls were used for this study but it is also common to use balls and jars made of tungsten carbide or zirconia to increase the impact energy, reduce contamination of mixtures and to reduce ball wear.

It is possible to conduct dry and wet grinding. Moreover, wet grinding with additives such as ethanol, stearic acid, acetic acid and acetone can be used can be used for very fine grinding. HEBM is a powerful technique for particle size reduction and surface area enhancement for gas materials [70]. The ball to mass ratio and rotation acceleration are important parameters for determining the collision energy between the balls. The reported mass to ball ratios are between 1:5 and 1:50 [72]. As a result of mechanical milling homogeneous nano-crystallite compounds can be formed at quasi-ambient temperatures. Materials processed using HEBM have showed significantly different characteristics in comparison with materials processed using conventional powder methods [66, 73, 74].

5.2 Characterization

5.2.1 X-ray diffraction

X-ray diffraction (XRD) is a technique commonly used to obtain information about the internal structure and phase identification of crystalline materials. X-rays are chosen and are suitable because their typical wavelength is comparable to inter-atomic spacing is approximately 2 to 3 Å. The technique was pioneered by Max Von Laue in 1912, who discovered that crystalline material act as a diffraction grating for X-ray wavelengths. The technique employs the diffraction of electromagnetic waves through a specimen.

Bragg's law describes a simplistic model to understand what conditions are required for diffraction. The law describes two or more parallel planes of atoms, with d-spacing between the planes as show in Figure 5.4(a). Rays interfere constructively only when Bragg's law is satisfied which is expressed as

$$n\lambda = 2d_{(hkl)}sin\theta, \tag{5.2.1}$$

where θ is the Bragg's angle at which a peak is observed, λ is the wavelength and n is an integer known as the order of diffraction, hkl are the Miller indices for inter-planar crystal planes in a crystal lattice and d is the spacing between inter-planar crystal planes also referred to as d-spacing [75]. Consequently, a family of planes produce diffraction peaks only at a specific angles as shown in Figure 5.4(b). In general the d values are calculated and expressed theoretically in terms of the lattice constants a, b, and c and

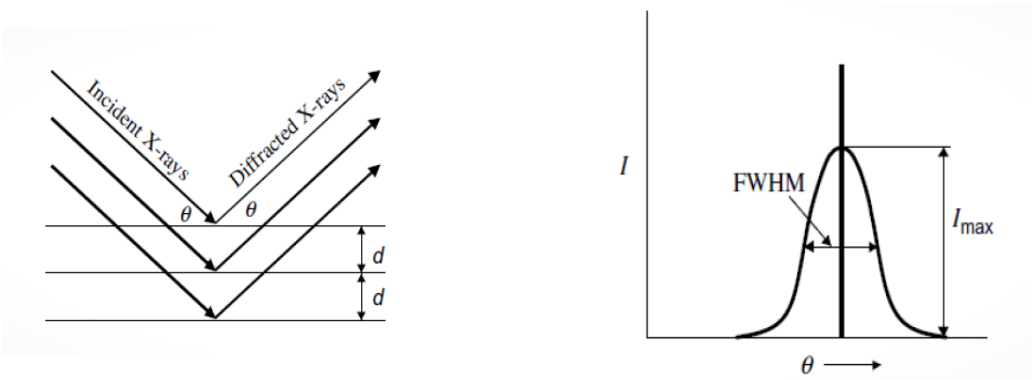

(a) (b)

Figure 5.4: (a) X-ray paths reflecting at normal angle to the reflection intermolecular planes. (b) Diffraction peak at constructive interference and FWHM for instrument broadening correction.

interaxial angles α, β, and γ for all crystal systems. This is achieved with the application of equation 5.2.1. Thus, knowing d, these quantities can be calculated.

The characterization by XRD was performed on a Philips X-ray diffractometer type PW 1710 as shown in Figure 5.5. A recommended 0.5 g of a sample was loaded on an acetone cleaned sample holder and levelled using a glass slide for optimum diffraction. The diffractometer uses a monochromatic beam of CoKα radiation with a wavelength of 1.7903 Å. Scanning was conducted between 20 °C and 80 °C and the diffractograms were recorded for each step of 0.008° of 2θ. The diffractometer used for XRD measurements uses the Bragg-Brentano geometry as shown in Figure 5.6. The intensity is obtained with a movable detector to gather all reflections from different crystal angles. The obtained XRD patterns were processed for phase identification using a combination of JCPDS XRD database, HighScore plus suite and Match software.

Important parameters such as lattice parameters, density ρ, bond lengths and strain can be determined. FullProf software was used for the refinements. The program assumes a starting model and makes use of iterative least squares method for convergence. Hence, the starting model has to be close to the actual values for convergence to occur.

The peak with the most intensity was used to estimate mean crytallite size D. This was done using the Scherrer equation [75].

Figure 5.5: PW 1710 Empyrean PANalytical X-ray diffractormeter, Geology (WC), UKZN.

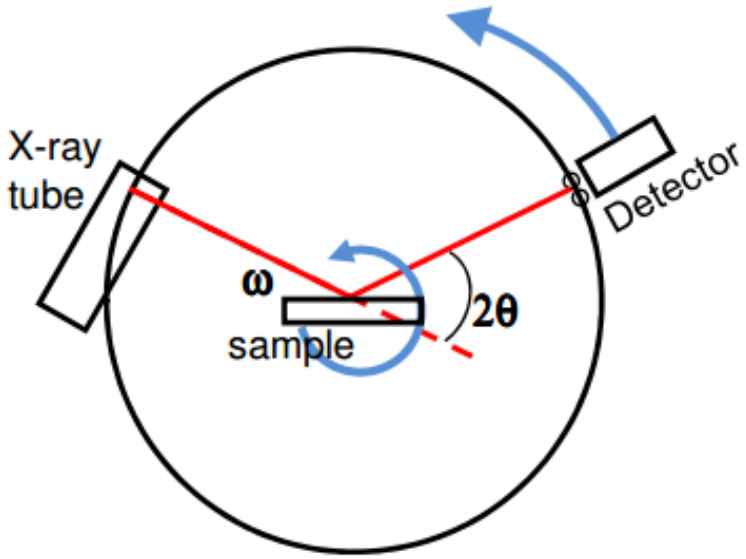

Figure 5.6: A schematic view of the sample and rotating dectator[36].

$$D = \frac{K\lambda}{\beta_{hkl}\cos\theta}, \tag{5.2.2}$$

where K is a crystallite shape dependent parameter and $K = 0.94$ was used assuming

semi-spherical crystallites. β_{hkl} is the full width at half maxima (FWHM) of the peak with the highest intensity, λ is the wavelength of the CoKα radiation (1.9703 Å) and θ is the diffraction angle of the plane with respect to the incident beam.

5.2.2 High resolution transmission electron microscopy and scanning electron microscopy

Structural and morphological investigations for this work were conducted with a high-resolution transmission electron microscope (HRTEM). The operation principle of HRTEM is similar to transmission electron microscope (TEM). TEM works on the principle of electron diffraction. It is a special kind of imaging technique compared to other microscopes. The electrons in TEM pass and interact with the atoms of the sample of interest. This interaction causes electrons to be scattered. The final image is a complicated interference pattern of the incident and diffracted beams. TEM is the best tool for direct visualization and analysis of the crystallography structure and particle size of the sample. The most important feature of this microscope is that the wavelength of the electrons is much smaller than the atomic separation in solids and thus making it possible to visualize crystal details well below the atomic size. However, the resolution of TEM is limited by different aberrations of the magnetic lens used. The most important one is chromatic and spherical aberration C_s. Technological developments of TEM has led to a modern aberration corrected TEM that makes use of a mono-chromator and a C_s corrector to reach point resolution below 0.5 Å. This microscope is now called HRTEM.

A Joel-JEM-2100 high resolution transmission electron microscope as shown in Figure 5.7 was used for this study. A small sample of approximately 0.0002 grams was placed into a small cone shaped plastic container and 0.0005 grams of ethanol was injected into the container. The mixture was vibrated in a 80 Hz/40 Watt transistorized sonic cleaner for 20 minutes. A copper thin film sample holder with a diameter of approximately 0.0005 mm was dipped into the vibrated sample and was loaded into the instrument in order to produce scanned images of the sample of interest. The images obtained for these measurements were processed using Imagej software.

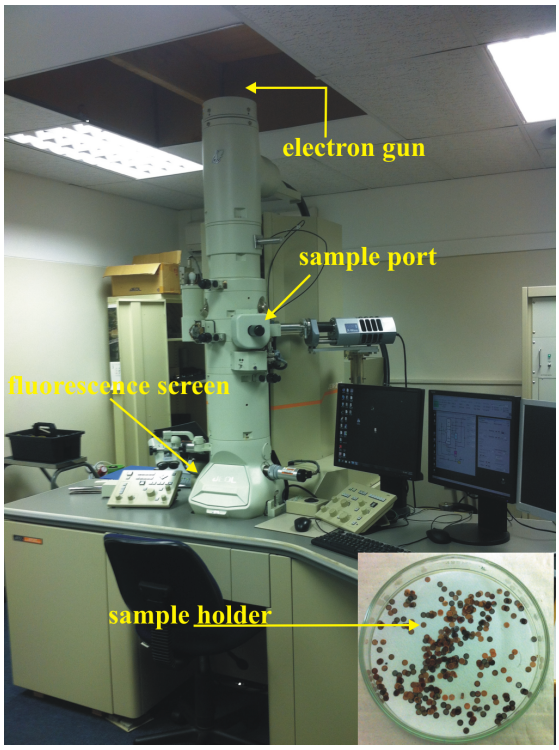

Figure 5.7: High resolution transmission electron microscope [46].

5.3 Magnetization measurement

The vibrating sample magnetometer was first developed by Foner in the late 1950's [11]. It is a basic research tool to determine the magnetic properties and determine magnetic behavior of materials in the presence of an external applied magnetic field. The magnetization measurement systems used are the LakeShore model 735 vibrating sample magnetometer and the Cryogenic Ltd 5 Tesla (50 kOe) mini cryogen free system (CFS).

5.3.1 LakeShore model 735 vibrating sample magnetometer

The LakeShore model 735 vibrating sample magnetometer (VSM) equipment in Figure 5.8 was used to measure the magnetization of the samples of interest. The system consists of an electromagnet power supply, cooling system, temperature controller, VSM controller, Gauss meter and a Janis helium cryostat. Figure 5.9 shows a detailed diagram of the model type used and how the system is integrated. Calibration is mainly done using the VSM software in the computer. A nickel sphere of 126.2 mg was used. The nickel sample produces a best signal of 6.92 emu at a magnetic field of 5000 ± 0.05 Oe. A maximum applied magnetic field of approximately 14 kOe was available on this system.

Figure 5.8: Lakeshore 735 Vibrating Sample magnetometer, Condensed Matter Physics Laboratory (WC), UKZN.

The fundamental operating principle is based on Faraday's law of electromagnetic induction

$$\frac{d\Phi_B}{dt} = -\varepsilon, \tag{5.3.1}$$

where $\frac{d\Phi_B}{dt}$ is the rate of change of magnetic flux and ε is the induced voltage in the pick-up coils that is proportional to the magnetization of the sample.

The sample to be studied was gently inserted in to the sample space such that it rests centered between a pair of pickup coils on the poles of the electromagnet as illustrated in Figure 5.9. The recommended sample size was in the range 0.03-0.06 grams. The magnetic sample under study is constrained to sinusoidal vibrations only along the vertical axis. The studied sample is magnetized by the uniform magnetic field created between the poles of the electromagnet. This causes the sample to generate its own magnetic field. Moving the sample up and down in the vicinity of the pickup coils induces an electrical current in the coils. The sample magnetic moment is measured by measuring the electric current induced in the detection coils. The electrical signal detected in the coils is proportional to the moment, amplitude and frequency of vibration. The magnitude of the signal is dependent on the magnetic properties of the sample itself. Data acquisition was done

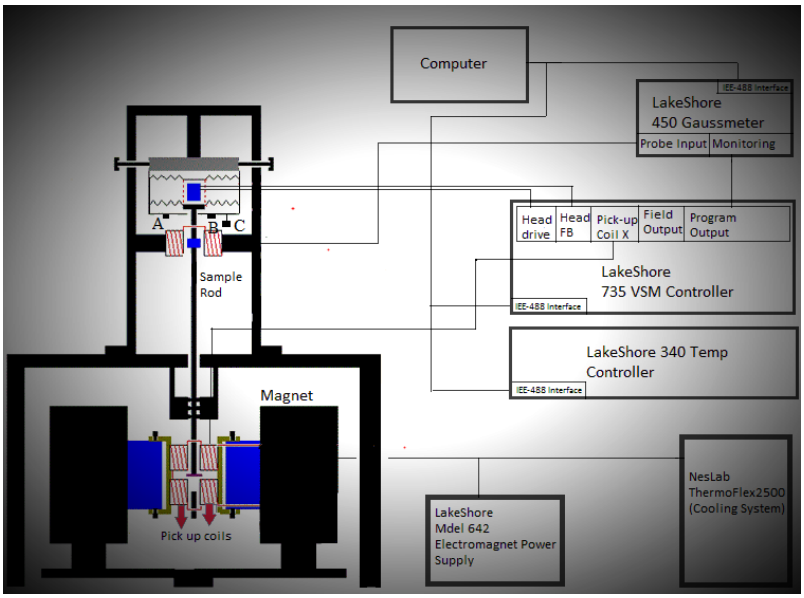

Figure 5.9: VSM block diagram for connection set-up.

using a VSM data acquisition software installed in the computer.

5.3.2 Mini cryogen free measurement system (CFM)

CFM is a physical property measurement system (PPMS) with several measurement options on the same system. The system can be used to conduct magnetic and electrical measurements. The system is designed for magnetic characterization up to 5 Tesla and variable temperatures from 2 K to 300 K without the need of a liquid cryogen. The equipment has a low field power supply in order to achieve accurate magnetic fields from zero to 5 Tesla. A water chiller to suit the F50H compressor on the system is included to minimise cooling water usage. Samples were inserted and carefully lowered via the airlock to the Variable Temperature Insert (VTI) between the pick up coils within the bore of the superconducting magnet. Operation principal for data acquisition is similar to that of LakeShore VSM. Figure 5.10 displays connection of the system during measurements.

A sample of 0.005 grams is required and was used for the magnetization measurements. The sample was loaded into a perspex cone and held fixed by cotton wool to avoid movement of the sample. The loaded perspex cone was carefully guided into a 10 cm straw. The sample to be measured is located at 2 cm from one end of the straw. The sample was held fixed to the perspex cone and straw by Kaptone tape. The side of the straw

with the longer length to the loaded perspex cone was secured to the probe rod via an adaptor provided on the rod. The rod was mounted in the airlock position before centering. Calibration for magnetization measurements were conducted using a yttrium iron garnet sphere. Full operational details are provided in the operational manual provided by Cryogenic Ltd, UK.

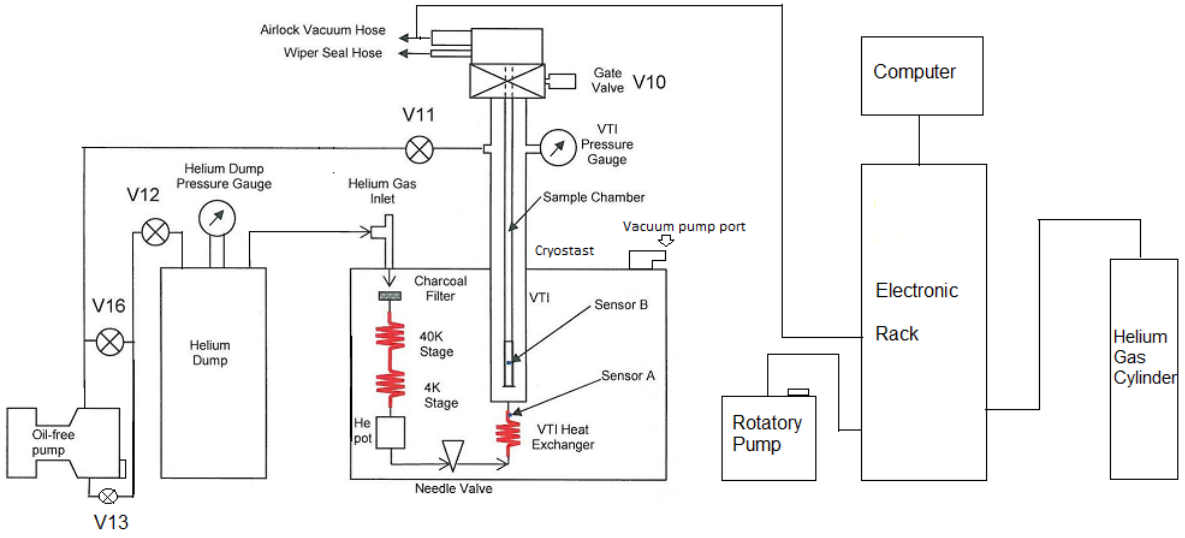

Figure 5.10: Block diagram for the measurement system.

5.4 Mössbauer spectroscopy measurements

In this work ^{57}Fe Mössbauer spectroscopy was used to investigate the oxidation states of Fe ions, magnetic ordering, hyperfine interactions and distribution of Fe ions in the tetrahedral and octahendral sites.

Mössbauer measurements were conducted at ambient temperature. The spectrometer used consists of a power supply, MR-357 Mossbauer drive unit, spectroscopic CANBERRA amplifier, IIFAST ComTec pre-amplifier, LND INC 45431 proportional radiation detector, $ORTECMCS - pci^{TM}$ data acquisition card and multichannel analyzer software version 2.13 installed in a desktop computer. Figure 5.11 shows a schematic diagram of the Mössbauer set-up. The ORTEC $MCS - pci^{TM}$ data acquisition consists of only the option for a single channel analyser (SCA) which sweeps through 512 channels one at a time. This causes the spectrum build up to be rather slow in comparison to data acquisition cards with options for pulse height analysis (PHA) where all channels are

opened simultaneously in order to identify the 14.4 keV Mössbauer peak. Figure 5.12 shows the emission spectrum of a 50 mCi ^{57}Co source. The Mössbauer drive remained off for this measurement spectrum. At 14.4 keV the Mössbauer line can be observed which is emitted by the excited ^{57}Fe when it transitions from $I = \frac{3}{2}$ to $I = \frac{1}{2}$. A standard 99.5% pure iron foil with a thickness of 0.0025 mm was used at ambient temperature to generate a velocity calibration. A typical Mössbauer spectrum for Fe foil is displayed in Figure 5.13.

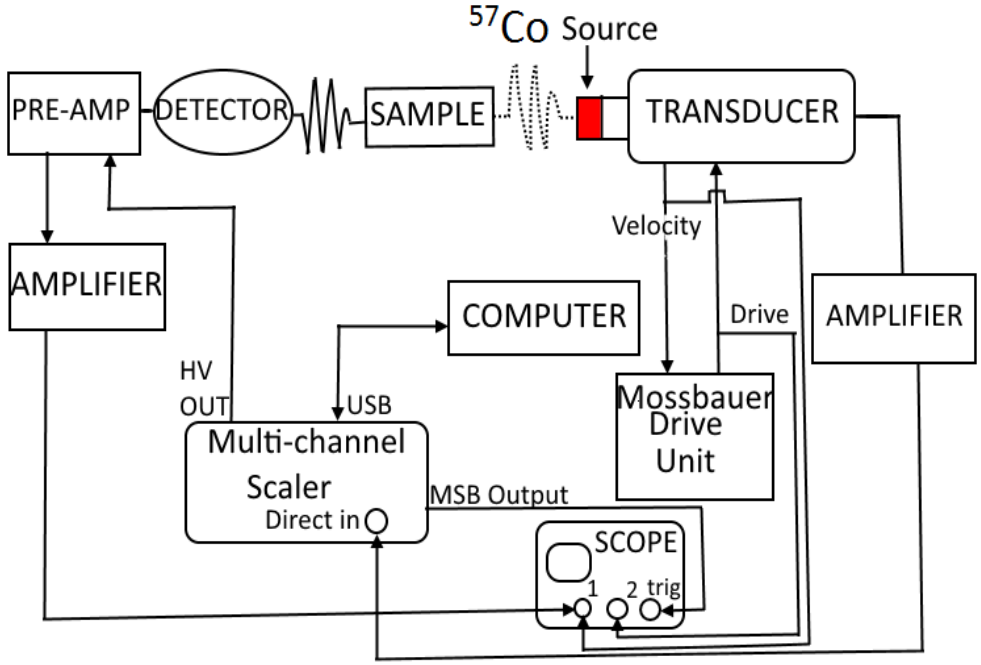

Figure 5.11: Block diagram for showing Mössbauer spectroscopy set-up.

A typical sample size used as an absorber was in the range of 0.9 - 0.1 grams. The powder sample was spread uniformly on a 13 mm diameter plastic sample holder and was firmly immobilized. The source was vibrated at constant acceleration. The detected γ ray spectrum were recorded for at least 5 hours after which it was ready for processing. The processing of the data involve fitting the spectra using recoil software. The parameters extracted include Isomer shift, line-width, nuclear quadrupole splitting and hyperfine magnetic field.

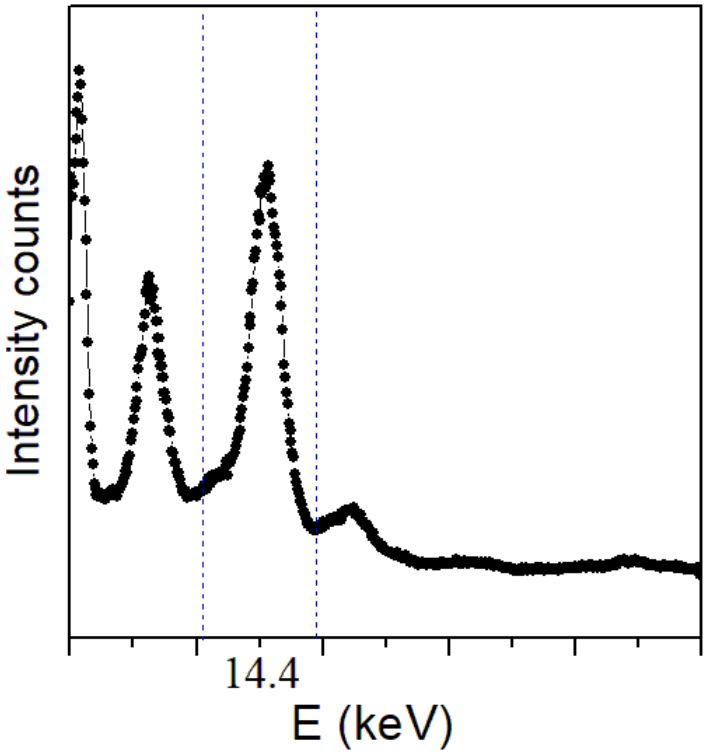

Figure 5.12: Emission spectrum ^{57}Co.

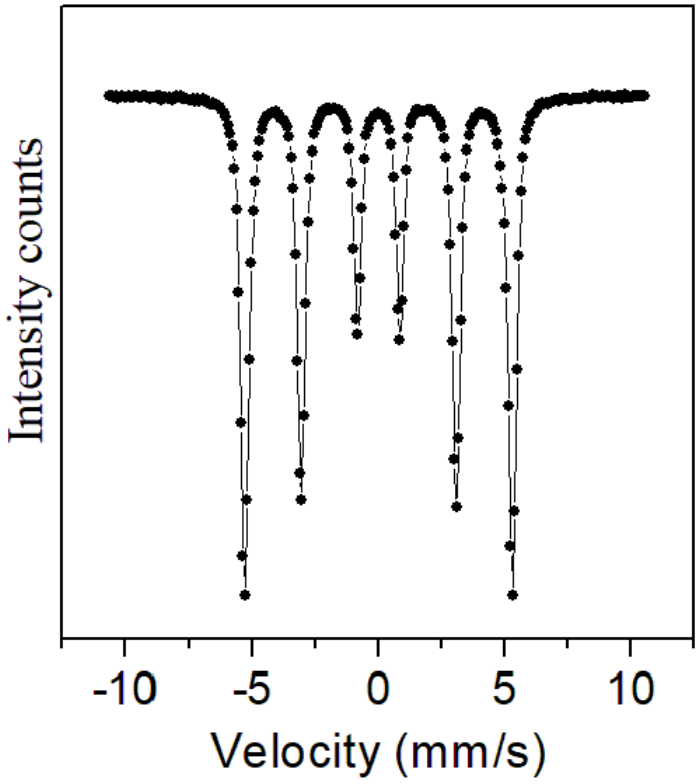

Figure 5.13: Transmission spectrum of elemental iron. The peaks have been annotated with the corresponding velocity of the Mössbauer drive.

5.5 Electrical measurements

The semiconducting properties of the samples were studied through the electrical resistivity measurements using the four-probe method. Figure 5.14 shows the schematic diagram of the experimental setup for resistivity measurements as a function of temperature. The set up consists of a transformer which serves to step down the voltage to 57.5 V. A solid state relay (SSR) functions as a voltage switch and as a digital PID temperature controller connected to the oven. The four probe unit is connected to a low current source and digital microvotmeter. Voltage and current readings were taken from 23.5 °C up to 100 °C at every 1 °C increment. The four probe connections are shown Figure 5.15 consists of two outer probes which measure current and two inner probes which measure voltage drop. This method actually measures the surface layer resistivity. However, by increasing the spacing between the probes and the depth of penetration of the current bulk resistivity can be deduced. The powdered samples were pressed into pellets at 2000 psi for 4 minutes and annealed at 200 °C. The pellets used in the measurements all had sample thickness h always less than probe spacing a. The resistivity in this case can be expressed as

$$\rho = \frac{\pi}{ln2} h \frac{\triangle V}{I}. \tag{5.5.1}$$

Resistivity ρ as a function of temperature can be used to calculate the tunneling activation energy (E_1) and activation energy (E_2). In semiconductors at relatively higher temperatures charge carriers move between the divalent and trivalent cations. At this region resistivity is obtained by following Arrhenius formula

$$\rho(T) = \rho_0 \exp\left[\left(\frac{E_i}{k_B T}\right)\right]. \tag{5.5.2}$$

where E_i is E_1 or E_2 and can be deduced from the plots of $ln\rho_T$ versus $T^{-1/2}$ or T^{-1} respectively.

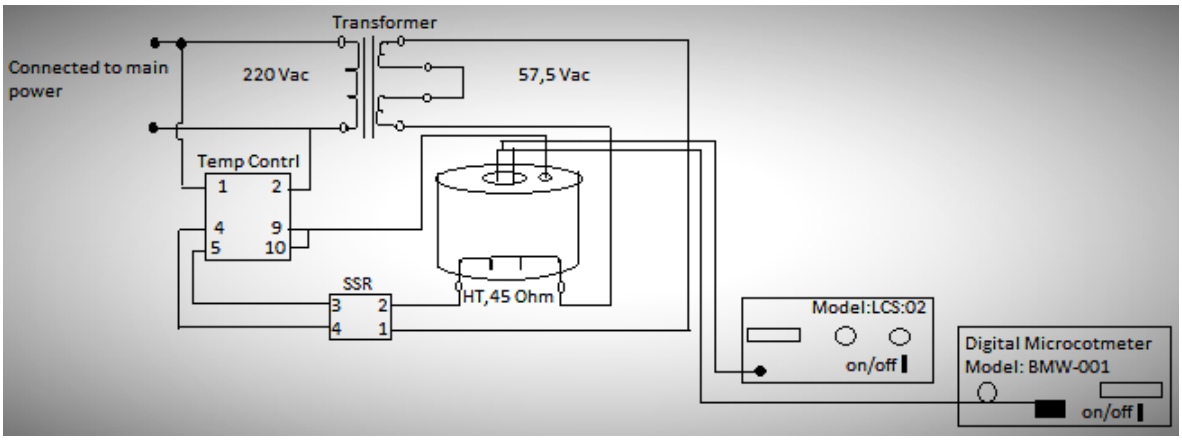

Figure 5.14: Schematic diagram for electrical measurement setup.

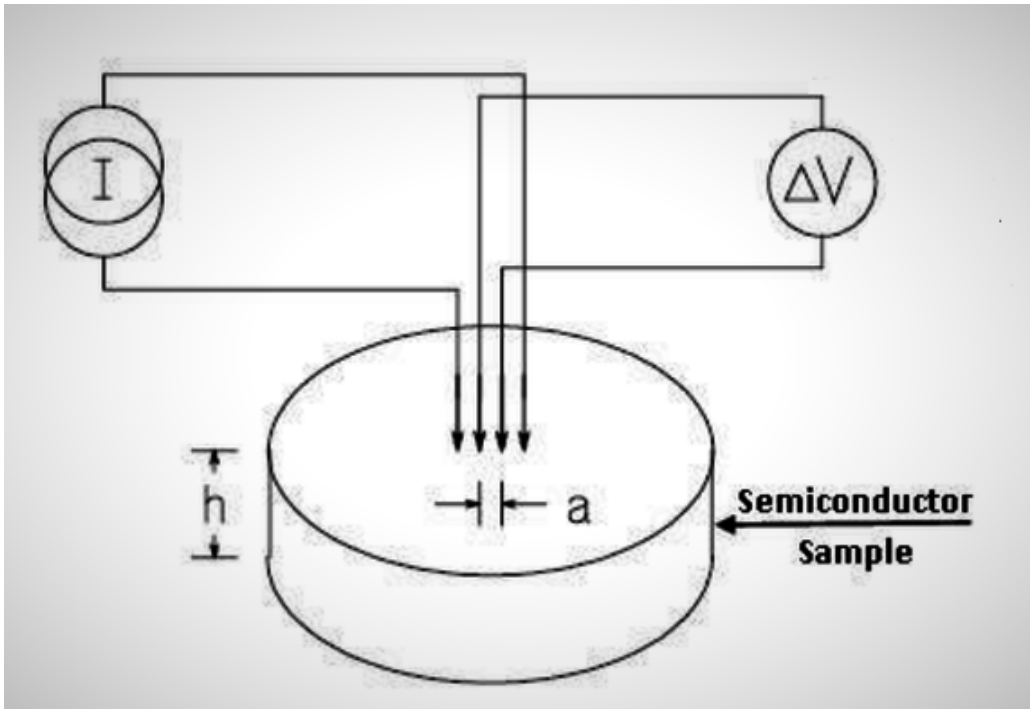

Figure 5.15: Schematic configuration of the four-point unit.

5.6 High temperature tube furnace

Thermal treatment of the samples were conducted in a Sentro Tech (type: STT-1600C-3-24) high temperature tube furnace shown in Figure 5.16. The samples can be heated in powder form or pressed into pellets. The furnace consists of a $MoSi_2$ heating element, B-type thermocouples, Yudian 30 segment programmable temperature controller and Eurotherm over temperature controller. The programmable temperature controller can be used to instruct the heating rate soak stages. For this current study, annealing

schedule was designed to heat up to a user specified temperature and to remains constant for prescribed period of time before cooling at an instructed heating rate back to room temperature to terminate the program. The maximum operating temperature is 1600 °C in air and 1500 °C in a vacuum. The tube diameter is 76.2 mm and the heating zone is length 609.6 mm. The furnace allows measurements to be conducted under air or argon gas environment.

Figure 5.16: Sentro Tech high temperature furnace (type: STT-1600C-3-24).

5.7 Brunauer-Emmett-Teller (BET)

BET analysis provides precise specific surface area evaluation of nano-materials by nitrogen adsorption measured as a function of relative pressure using a fully automated analyzer. The technique encompasses both the external area and pore area evaluation to determine the total specific surface area in m^2/g and at the same time give crucial information on the effects of surface porosity and particle size relevant in applications. BJH analysis can also be utilized to determine pore area and specific volume using adsorption and desorption techniques. However, unlike BET this technique characterizes pore size distribution independent of external area.

5.7.1 Operating principle

The amount of gas adsorption by a material depends not only on the amount of surface exposed but also on the temperature, gas pressure and strength of interaction between the gas and solid. Nitrogen gas (N_2) is mostly used in BET analysis due to its availability in high purity and its strong interaction with most solids. The material of interest is cooled down using liquid N_2 to obtain detectable amounts of adsorption. Liquid N_2 was released step wise into sample cell. Relative pressure which is less than atmospheric pressure is obtained by creating conditions of partial vacuum. Beyond the saturation pressure no adsorption occurs regardless of any further increase in pressure. A highly precise and accurate pressure transducer monitors the pressure changes due to adsorption process. At the point at which the adsorption layers have formed, the sample is removed from nitrogen atmosphere and heated to release the adsorbed nitrogen from the sample and quantified. The data collected is displayed in the form of BET isotherms which are plots of the amount of gas adsorbed as function of the relative pressure. The six IUPAC standard adsorption isotherms are shown in Figure 5.17.

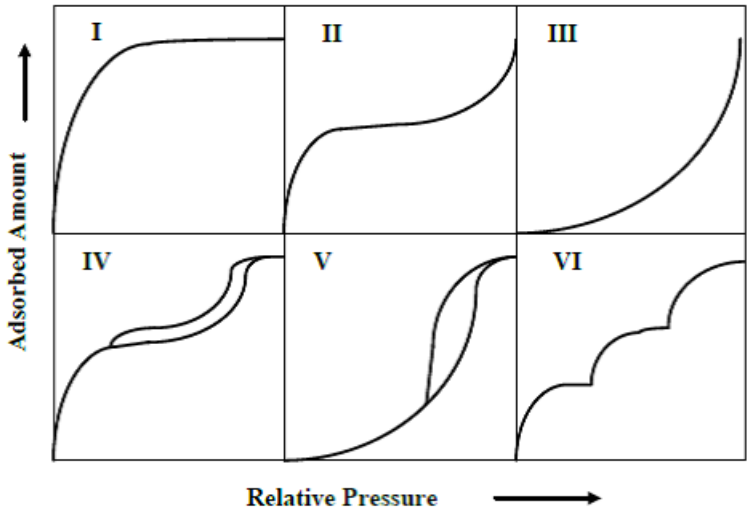

Figure 5.17: The six IUPAC standard adsorption isotherms for gas/solid interaction.

The hysteresis loops differ because the systems demonstrate different gas/solid interactions. Information obtained from BET isotherms can be used to determine the surface area of a sample using the BET equation

$$\frac{1}{X\left[\left(P_0/P\right)-1\right]} = \frac{1}{X_m C} + \frac{C-1}{X_m C}\frac{P}{P_0}, \tag{5.7.1}$$

where X is the weight of nitrogen adsorbed at a given relative pressure (P/P_0), X_m is monolayer capacity, which is the volume of gas adsorbed at standard temperature and pressure (STP), and C is constant. STP is defined as 273 K and 1 atm. A plot of $1/X\left[(P_0/P)-1\right]$ verses P_0/P should be a straight line with a positive slope for reliable surface area measurements. The total surface area of the sample can be obtained form the formular

$$S_{total} = \frac{X_m L_{av} A_m}{M_v}, \tag{5.7.2}$$

where L_{av} is the Avogadro's number, A_m is the cross sectional area of the liquid nitrogen and is equals to 0.162 nm^2 for an absorbed nitrogen molecule, and M_v is the molar volume.

5.7.2 Sample preparation

Figure 5.18 shows the BET instrument used for sample measurements. Samples were degassed to remove water and other contaminants for accurate specific surface area measurements.

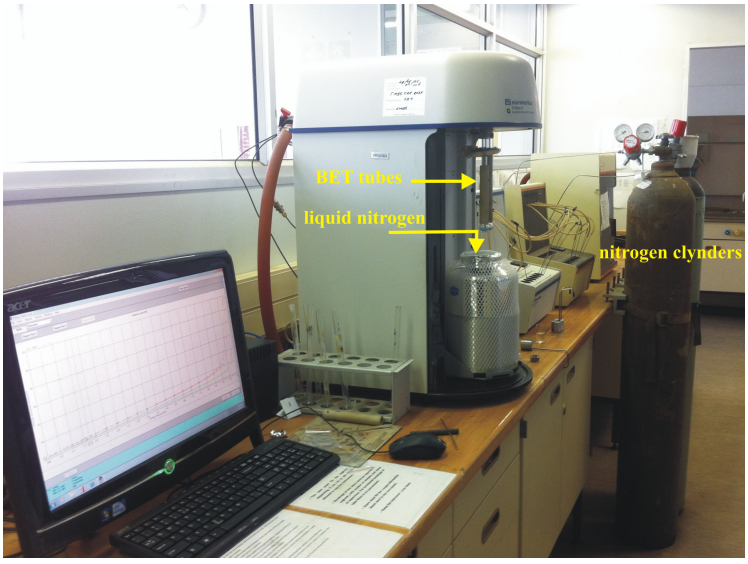

Figure 5.18: Schematic representation of the BET instrument.

Samples were degassed in a vacuum for 20 hours at 150 °C. For each sample, 0.5 grams was measured and transfered in to glass cells for degassing and BET analysis. Glass

rods were placed within the cell to minimize the dead space in the cell. A 6 mm sample cells were used and placed into a heating mantle and connected to the outgas port of the machine. The sample cells was placed in the analysis port post degassing. liquid nitrogen was used to cool the sample and maintain it at constant temperature to optimize the interaction between the gas molecules and the surface of the sample in order to obtain measurable amounts of adsorption. The adsorbate was injected into sample cell with a calibrated piston. The dead volume in the sample cell is calibrated before and after each measurement. Calibration was done using helium gas since it does not adsorb on to any sample.

5.8 Other techniques

Measurements were also conducted on a Zeiss Evo LS15 scanning electron microscope (SEM) for morphological studies and for qualitative measurements of the constituent elemental composition using the energy-dispersive X-ray (EDX) method. A Perkin-Elmer 100 3.2 Attenuated Total reflection Fourier transform infrared spectroscopy (ATR-FTIR) which uses infrared light to scan the sample was used to characterize the chemical properties.

Chapter 6

Structural, electrical and magnetic characterization of $LaNi_{0.25}Ti_{0.25}Fe_{0.5}O_3$ perovskite

6.1 Introduction

Ternary metal oxides with general formula of ABO_3 have received considerable attention due to their wide range applications as catalysts [76, 77], gas sensors [78, 79, 80], magnetic material [81], fuel cells [82, 83, 84], and electric ceramic materials [85]. This is owing to the ease of chemical formula adjustment and flexibility of doping [10]. Partial substitution of transition metals at B sites with other cations can be effective in enhancing the oxidation activity of perovskites and can be used to improve performance [86].

Nickel titanate $NiTiO_3$ belongs to the ilmenite family with a rhombohedral structure at room temperature. In this structure, both Ni and Ti atoms prefer the octahedral coordination with alternating cation layers occupied by Ni and Ti [87]. It is one of the prominent key materials with possible applications in photo-catalysis, sensors and fuel cells [88]. Nickel titanate exhibits ferroelectric properties with excellent electrical properties. Over the past few years, studies to improve sensing properties of perovskite oxides have been conducted by co-substitution of the A, B or AB sites and attempts have been found to be interesting and satisfactory. Substitution in the B or A sites of perovskites has revealed interesting results with respect to gas sensing [10, 89]. $LaFeO_3$ has been

reported to have a degree of gas sensing. It is also a p-type semiconductor with band gap between 2 and 2.6 eV [90].

We have therefore synthesized $LaNi_{0.25}Ti_{0.25}Fe_{0.5}O_3$ (LNTFO) perovskite in which equal mole ratio of Ni and Ti are substituted on the B sites of $LaFeO_3$. To our knowledge the LNTFO compound has not been reported in the literature.

6.2 Experimental details

LNTFO was prepared by a two-step process of milling and thermal annealing. The starting compounds were high purity La_2O_3 (99.99%), NiO (99.8%), TiO_2 (99.8%) and Fe_2O_3 (99%) sourced from Sigma Aldrich. The oxides were weighed according to calculated stoichiometry. About 5 grams of well mixed powdered oxides were charged in a 250 ml stainless steel jars containing 9 mm hardened steel balls in a ball to mass ratio of 10:1. The sample was milled in air atmosphere using a Retch planetary ball mill (type: PM 400 MA) operated at 300 rpm for 5 hours. The milled powder was then annealed at 1000 °C for 2 hours at a heating rate of 5 °C/min in a Sentro Tech furnace. The X-ray diffraction (XRD) patterns before and after annealing were obtained using CoKα radiation (1.7903 Å) on a Philips diffractometer (type: PW 1710) in 2θ steps of 0.008°. The Mössbauer spectrum was acquired at room temperature about 300 K using a conventional constant acceleration spectrometer with a ^{57}Co source sealed in Rh matrix. Magnetization measurements were performed in the range 10 to 300 K on a 5 Tesla mini cryogen free measurement system. The microstructure and morphology were investigated using high resolution electron microscopy (HRTEM) and scanning electron microscopy (SEM).

6.3 Results and discussion

6.3.1 Structural and morphology analysis

The XRD patterns of LNTFO in Figure 6.1 exhibit single phase perovskite structure. The best fit model used for refinement is that of an orthorhombic crystal system belonging to space group *P 2ac 2n* and was obtained using Match software [91]. The Reitveld refinement were carried out using fullprof program [92, 93]. Based on the best agreement

between observed and calculated profile intensities of the powder pattern, lattice parameters, direct cell volume and density of the LNTFO compound were determined. The refined lattice parameters obtained were $a = 5.534 \pm 0.005$ Å, $b = 7.819 \pm 0.006$ Å and $c = 5.539 \pm 0.005$ Å. The direct cell volume and refined density is obtained to be 239.65 ± 0.22 Å^3 and 4.841 g/cm^3 respectively. The lattice strain of 0.004 ± 0.001 was estimated from the slope of the

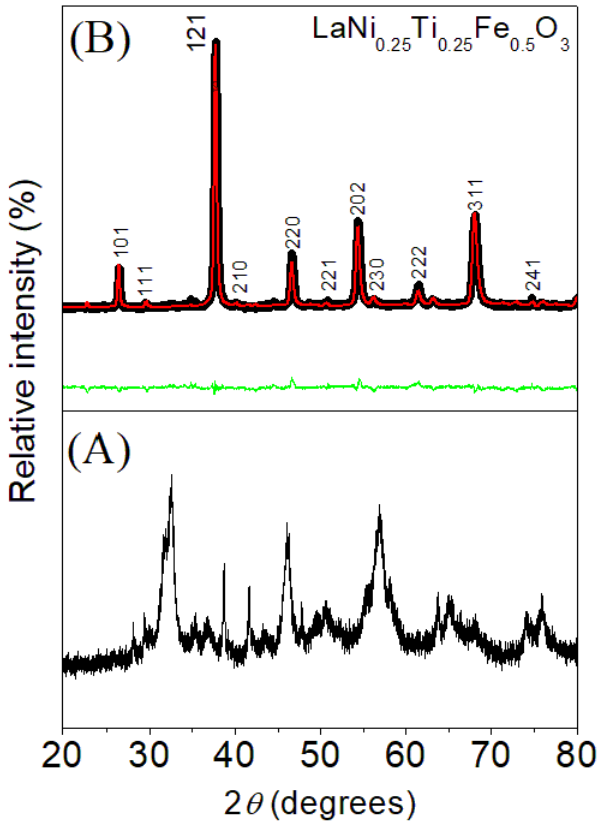

Figure 6.1: Room temperature XRD pattern of the milled and annealed powder of LNTFO.

Williamson-Hall plot in Figure 6.2. The Scherrer's formula [75] was used to estimate the crystallite size

$$D = \frac{K\lambda}{\beta_{hkl} \cos\theta}, \tag{6.3.1}$$

where K is crystallite shape dependent parameter of 0.94 for semi-spherical crystallites. β_{hkl} is the full width at half maxima (FWHM) of the highest intensity (121) peak. λ is the wavelength of the CoKα radiation and θ is the relevant diffraction angle of a plane. The average crystallite size for the compound was calculated from the strong reflection peak

(121) of the XRD pattern and obtained to be 35.5±0.2 nm. The stability of perovskite phase was determined using the Goldschmidt tolerance factor [19]. The tolerance factor is defined as

$$t = \frac{1}{\sqrt{2}}\left(\frac{r_A + r_O}{(r_B + r_O)}\right), \tag{6.3.2}$$

where r_A and r_B are the average ionic radius of the A and B site cations respectively. r_O is the ionic radius of the anion. A tolerance factor of 1 indicates a perfect cubic structure system. In perovskites, t is generally in the range between $0.75 \leqslant t \leqslant 1$. In the lower part of this range the structure may be distorted due to tilting of the BO_6 octahedral and the lowering of symmetry. The tolerance factor for the LNTFO compound was calculated to be 0.89 which is in the range classifying perovskites of an orthorhombic structure [18].

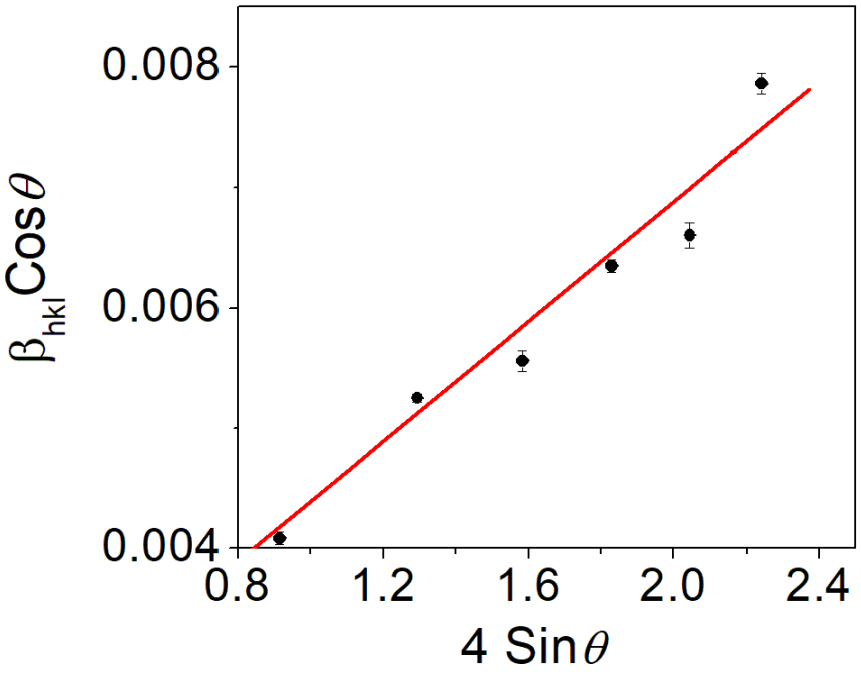

Figure 6.2: Williamson-Hall plot of β_{hkl} cosθ against 4 sinθ of LNTFO perovskite.

Figures 6.3 and 6.4 show micrographs obtained from high resolution transmission electron microscopy (HRTEM). Figure 6.3 confirms the crystallinity of the annealed material. The average d-spacing obtained at different regions of the sample is 0.33 nm and was obtained using Gatan microscopy suite software [94]. Figure 6.3 shows Crystallite sizes estimated using ImageJ software [95]. The crystallite size follow a Gaussian distribution. Particle size is estimated to be 91±5 nm. The reflection bright spots in Figure 6.4 indicates the *hkl* Miller indices. Figure 6.5 shows scanning electron microscopy (SEM) micrographs

and observations indicate that grains are densely packed and are of different shapes and sizes which indicate the existence of polycrystalline microstructure. The grains are loosely packed in some regions of the sample and consists of small voids. Energy dispersive X-ray micro-analysis (EDX) spectrum was utilized to confirm the elemental composition for the as-prepared sample.

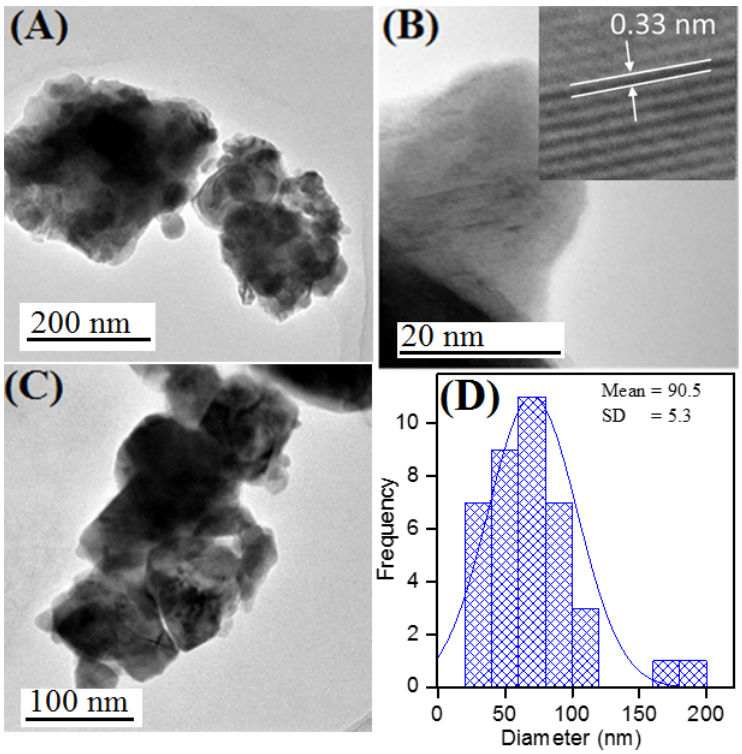

Figure 6.3: HRTEM micrographs (A), (B) and (C). Particle size distribution (D).

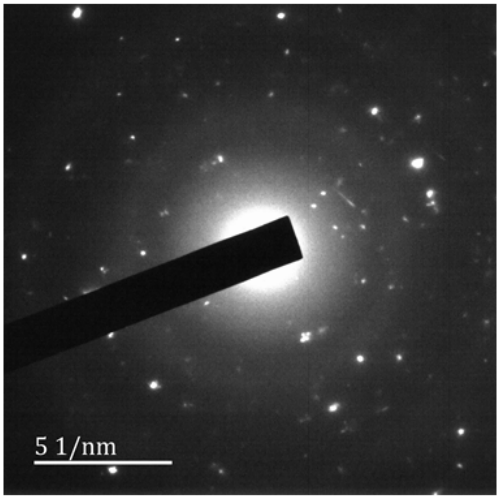

Figure 6.4: HRTEM diffraction micrograph for annealed sample.

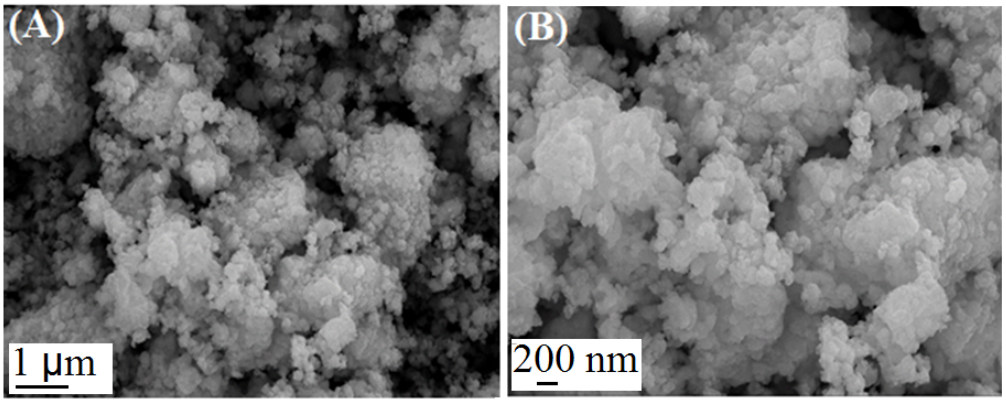

Figure 6.5: SEM micrographs (A) and (B) at magnification 10 KX and 20 KX respectively.

Figure 6.6 shows the peaks corresponding to all expected elements (La, Ni, Ti, Fe, O) and the remaining peaks are of Au which was used to coat the sample before measurements. The inset in Figure 6.6 shows weighted percentages. The elemental composition of the as-prepared sample post synthesis is in agreement with that of calculated stoichiometry before synthesis. The number of atoms present for each element of the compound was verified with the assumption that for each set of elements of the compound one of the element's atom number is true and is printed in bold-face in the results shown Table 6.1.

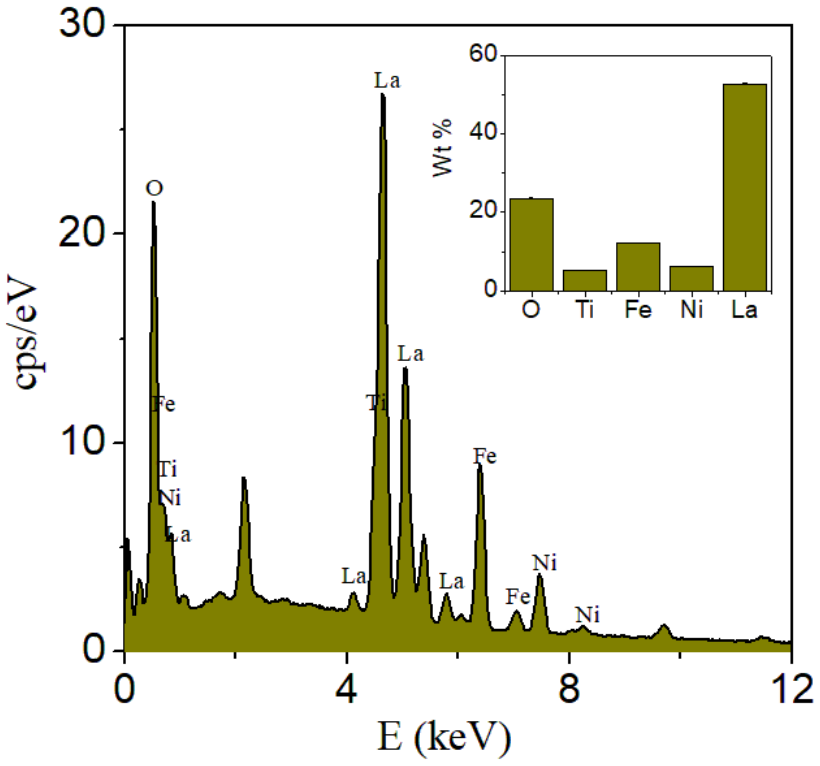

Figure 6.6: EDX elemental composition and atomic percentage of annealed LNTFO.

Table 6.1: Verification for the number of atoms present in the compound post synthesis for the LNTFO sample. The bold face atom values for the compound are assumed to be true.

Elements	M_o	Wt%	$\frac{Wt}{M_o}$	X	number of atoms				
O	15.99	23.54	1.47	2.04	**3**	3.34	3.35	3.47	3.90
Ti	47.86	5.28	0.11	2.27	0.22	**0.25**	0.25	0.26	0.29
Fe	55.85	12.26	0.23	2.28	0.47	0.52	**0.5**	0.54	0.58
Ni	58.69	6.23	0.11	2.36	0.22	0.25	0.25	**0.25**	0.28
La	138.90	52.68	0.38	2.64	0.78	0.86	0.87	0.89	**1**

6.3.2 Attenuated Total reflection Fourier transform infrared spectroscopy (ATR-FTIR)

A Perkin-Elmer 100 FTIR was used to analyze the samples. The spectrometer works under ambient conditions. The spectra were registered in the range 4000-400 cm^{-1} wavenumber region for the as-prepared samples. Figure 6.7 shows the resulting peaks due to various vibrations. The peak at 1609 cm^{-1} can be attributed to La-O vibrations.

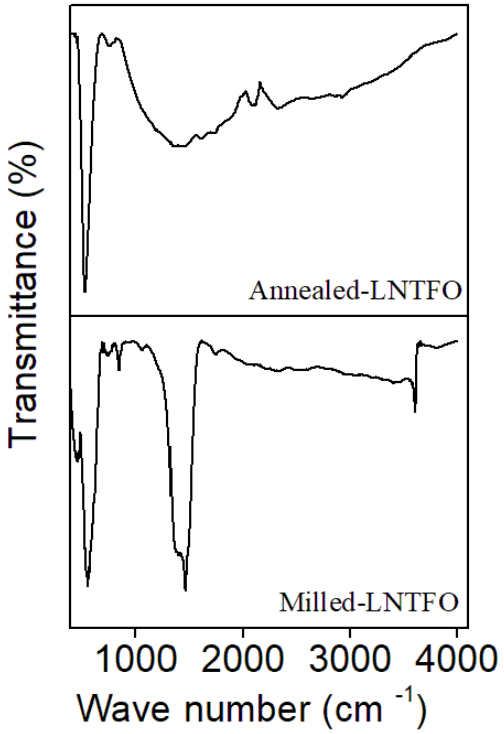

Figure 6.7: FTIR spectra of as milled and annealed samples of LNTFO.

The peak observed in the fingerprint region at 537 cm^{-1} is due to Fe–O stretching vibrations of octahedral FeO_6 group which is characteristic of the perovskite $LaFeO_3$ [96, 97]. No evidence of water is observed in the annealed sample. However, the hydroxyl group exists at 1456 cm^{-1} in the milled LNTFO sample.

6.3.3 Mössbauer and Magnetization

Magnetization measurements were conducted in the temperature range from 10 - 300 K in an applied field of up to 50 kOe. The hysteresis loops presented in Figure 6.8 show typical soft ferromagnetic properties.

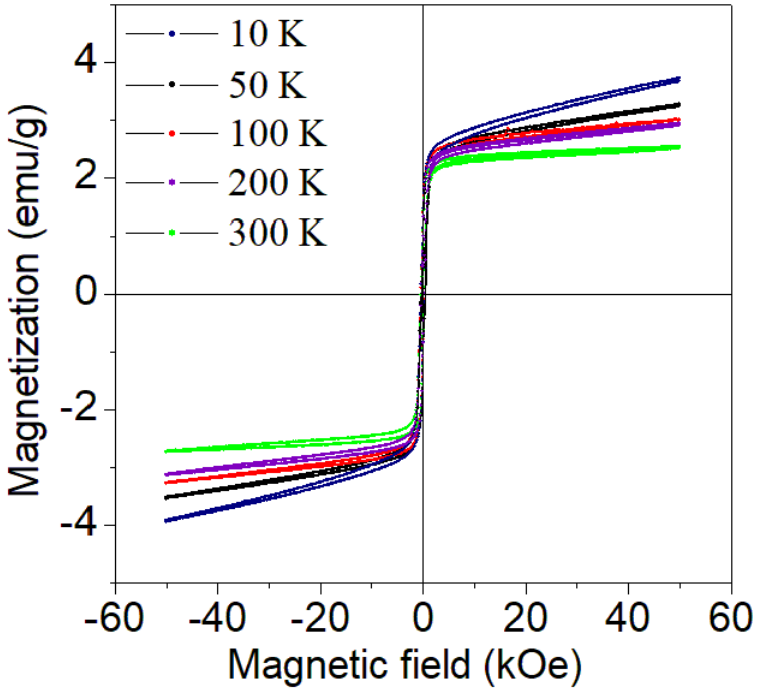

Figure 6.8: Magnetic hysteresis loops of the annealed LNTFO at different temperatures.

Table 6.2 shows variation of saturation magnetization, coercive field, remanent magnetization and squareness with temperature for the annealed LNTFO. Saturation magnetization M_S is relatively low for the as-prepared sample. This may be due to high concentrations of oxygen vacancies serving to undermine the super-exchange interaction resulting in reduced M_S [98]. However, in comparison with $LaFeO_3$ reported in the literature, the magnetization is increased probably owing to the presence of uncompensated spin of Ni^{2+} and Fe^{3+} [99]. Furthermore, the synthesis method tends to have different results of M_S. M_S was estimated according to the law of approach to saturation magnetization [100]

using equation 3.3.46. The coercivity of the annealed sample was calculated by

$$H_C = \frac{|H_1| + |H_2|}{2}, \tag{6.3.3}$$

Table 6.2: Variation of Saturation magnetization M_S, coercive field H_C, remanence magnetization M_R and squareness R with temperature for the annealed LNTFO.

T (K)	M_S (emu/g)	H_C (kOe)	M_R (emu/g)	R
	±0.2	±0.02	±0.1	±0.14
300	2.25	0.36	1.1	0.48
250	2.35	0.37	0.4	0.18
200	2.39	0.36	0.7	0.27
150	2.48	0.38	1.2	0.49
100	2.52	0.39	1.3	0.50
80	2.51	0.40	1.2	0.49
50	2.52	0.41	1.2	0.47
20	2.55	0.41	1.2	0.47
10	2.61	0.41	1.1	0.44

where H_1 and H_2 are the magnitudes of the fields along the field axis where the magnetization curve reduces to zero. The coercivity is small in the range of 360 to 420 Oe. A slight increase in the coercivity as the temperature drops is observed. The remnant magnetization is obtained from the vertical magnetization shifts when the applied field is zero.

^{57}Fe Mössbauer spectroscopy at room temperature was used to investigate the hyperfine magnetic field and the oxidation state of Fe. The Mössbauer spectra was best fitted with a doublet and two sextets as illustrated in Figure 6.9. The doublet fit parameters for isomer shift IS = 0.308±0.002 mm/s, quadrupole spitting QS = 0.675±0.005 mm/s, line width Γ = 0.520±0.005 mm/s and Fe^{3+} fractional population f = 31.9±1.4 % were extracted from recoil software. The doublet may be related to octahedral Fe^{3+} ions distributed homogeneously in the sample. Table 6.3 shows fitted parameters for the two magnetic sextets. The relatively higher magnetic hyperfine for the two sextets is assigned to the A site due to the ionic sizes of Ni-Ti-Fe and these elements commonly occupy the B site in the perovskite structure. This implies that the local spin density around Fe^{3+} atoms at the

A site is relatively high. The sextet with relatively higher population area is assigned to a well crystallized perovskite structure whilst the sextet with relatively lower population area is assigned to poorly crystallized LNTFO [101, 102]. The isomer shift values for the doublet and the two sextets indicate the presence of only Fe^{3+} iron ions [103]. Relatively lower isomer shift values may imply short bond lengths, strong covalent bond and high oxidation states [104].

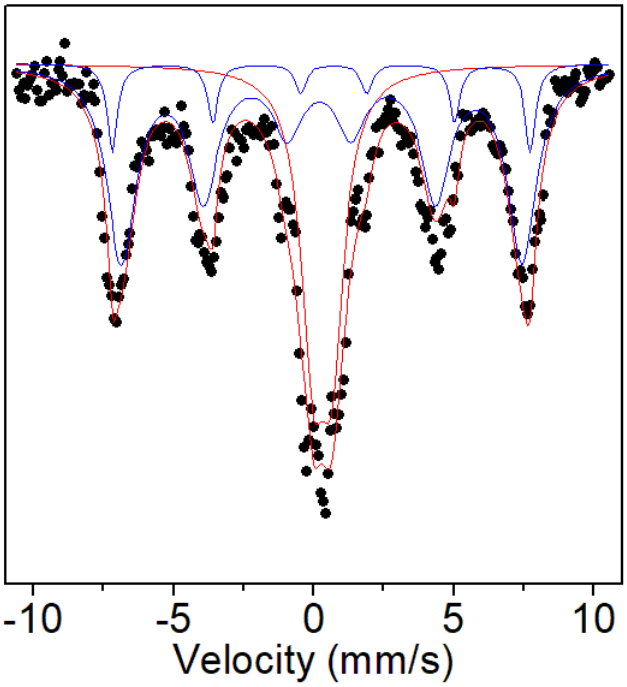

Figure 6.9: Mossbauer spectra of the annealed LNTFO material.

Table 6.3: Room temperature Mössbauer parameters of as prepared LNTFO sample: Hyperfine fields (H), isomer shift (IS), quadrupole spitting (QS), line width (Γ) and Fe^{3+} fractional population f on A and B sites.

H (kOe)		IS (mm/s)		QS (mm/s)		Γ (mm/s)		f (%)	
H_A	H_B	IS_A	IS_B	QS_A	QS_B	Γ_A	Γ_B	f_A	f_B
±3	±3	±0.04	±0.04	±0.04	±0.01	±0.09	±0.06	±2	±9
463	444	0.49	0.24	-0.22	0.04	0.23	0.62	10	58

6.3.4 Resistivity measurements

Measurements were conducted between 23 °C $\leq T \leq$ 100 °C using the four probe method. The inset on Figure 6.10 shows data used to estimate the activation energy. The sampling was done at the same temperature range where dataset is closest to approaching a straight line. Prior to measurements, the milled and annealed samples were pressed into pallets at 2000 psi for 4 minutes and heat treated at 200 °C for 2 hours. Figures 6.10 shows the Arrhenius plot of $ln\rho$ verses T^{-1} for the milled and annealed samples used to estimate E_a.

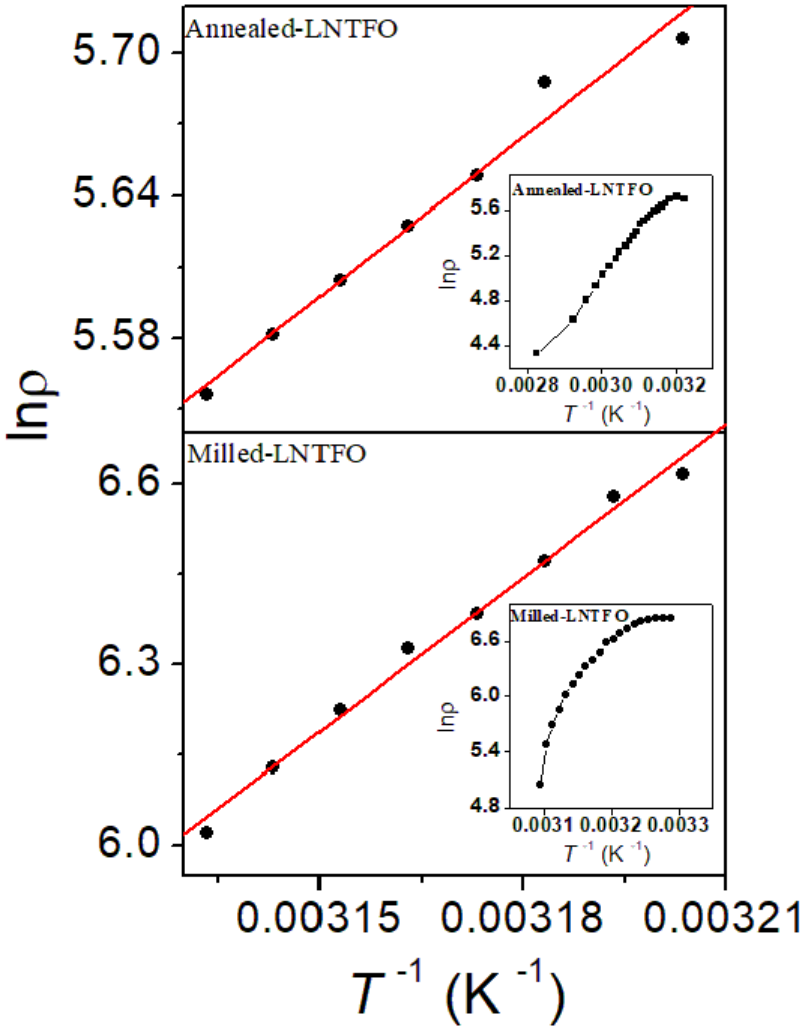

Figure 6.10: Sampled dataset for activation energy estimation for the milled and annealed LNTFO samples.

The calculations were performed assuming the resistivity follows Arrhenius equation expressed as

$$\rho(T) = \rho_0 \exp\left[\left(\frac{E_a}{k_B T}\right)\right],$$

where E_a the activation energy of the conduction is process, k_B the Boltzmann constant and T is the absolute temperature [20]. Observed fluctuation of voltage as measurements were being taken maybe be due to Seebeck effect [53]. It is well known that E_a for semi-conductors varies slightly with temperature. In this case E_a was calculated for temperatures in the same range at every 1 °C. The values calculated from the slope of the milled and annealed samples are 3.4±0.1 eV and 0.9±0.06 eV respectively. The milled sample shows insulating behavior at these temperatures. This is in agreement with increasing resistivity for simultaneously Ni-Ti perovskite [21]. A significantly smaller energy gap for the annealed sample which may be due crystal lattice expansion and interatomic bonds being weakened implying less energy required to break bonds and possibly also increase in ionic conduction at higher temperature as it is known that for semiconducting materials electrons and holes move between divalent Ni^{2+} and trivalent Fe^{3+} and Ti^{3+} ions [105]. It has been also suggested that in p-type semiconductors such as LFO formation of anion or oxygen desorption caused the decrease or increase in energy barrier [106]. A high band gap and low activation energy reported to be a pre-requisite for good gas sensing application [4]. Moreover, activation energy is directly proportional to sensing capabilities [107].

6.3.5 Brunauer-Emmett-Teller (BET)

Specific surface area and pore size distribution were obtained from the nitrogen adsorption-desorption isotherms as shown in Figure 6.11. The nitrogen adsorption-desorption curve exhibited type IV adsorption branch with a H3 hysteresis loop which according to IUPAC classification is characteristic of a mesoporous structure [108]. However, the width of the hysteresis is small which serves as an indication of a comparably small surface area. The BET specific surface area of the sample is 6.93±0.04 m^2/g. This is due to large particles, large grain size and the agglomeration of particles as proven by HRTEM and SEM. At relative pressure $P/P_0 \approx 0.5$ the pores appear to be empty. The adsorption of N_2 increased from 1.6 to 28.3 cm^2/g at relative pressures of 0.06 to 1 respectively. Desorption isotherm decreases with decreasing relative pressure following a path different from that of adsorption isotherm and hence a hysteresis loop due to condensation of N_2 in the sample

pores. Furthermore, below $P/P_0 \approx 0.5$ the adsorption-desorption isotherms join together to form a reversibility curve. The calculated average pore size and volume is 27 nm and 0.04 cm^3/g respectively. Pore size distribution of the sample as shown in the inset of Figure 9 was obtained by calculations via BJH method. The pore size distribution is in the range 2 to 47 nm and are of nun-uniform size which is strongly indicative of a type IV isotherm [109, 110].

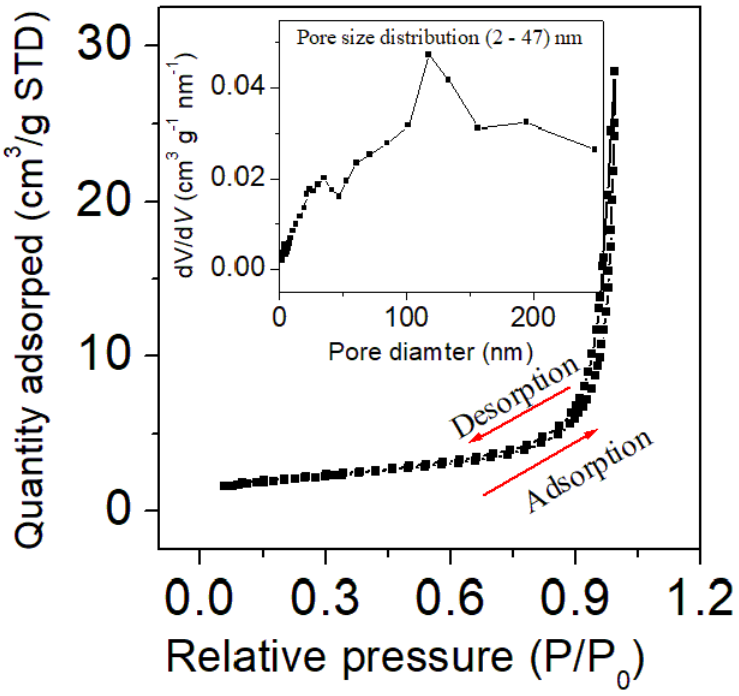

Figure 6.11: N_2 gas adsorption-desorption of the annealed LNTFO powder.

6.4 Conclusion

The polycrystalline samples of LNTFO was synthesized using ball milling and high temperature treatment for a relatively short time. In the absence of the hydroxyl group the conductivity of LNTFO increased significantly. The activation energy increased drastically which is good for solid state gas sensors as it has been reported to be proportional to gas sensing. Ni-Ti substitution increases the resistivity on the material at ambient temperatures. The saturation magnetization increased in comparison to LFO materials prepared using solid state route. The isomer shift values extracted from ^{57}Fe Mössbauer fitting indicates the presences of only Fe^{3+}. Furthermore, the strong covalent bond indicated by isomer shift values possibly between the metal and oxygen may play a huge role

in sensing. The increased magnetization at low temperature may serve as an important advantage for application in the gas sensing technology. However, the influence of magnetic properties with respect to gas sensing has not been extensively studied therefore it is recommended for further investigation. The specific surface area is quite low which hinders the materials optimum performance hence regrinding the material taking care not to destroy the phase would be useful in reducing particle size and increasing surface area preliminary to gas sensing tests.

Chapter 7

Synthesis and characterization of $BiNi_{0.25}Ti_{0.25}Fe_{0.5}O_3$ composites

7.1 Introduction

Multiferroic materials have attracted enormous attention due to their potential application in spintronic devices, information storage, magnetically modulated transducers and sensors [10]. $BiFeO_3$ (BFO) is a rhombohedrally distorted perovskite with *R3c* space group [111]. BFO is well known for its multiferroic properties due to both ferroelectric and antiferromagnetic ordering at room temperature [112]. It is also a p-type semiconductor that exhibits gas sensing properties to a certain degree [10]. In principle properly selected aliovalent dopants can serve to enhance gas sensing response and gas selectivity of oxide semiconductor sensors.

Therefore together with the interesting and unique properties possessed by nickel titanate $NiTiO_3$ described in section 6.1 paragraph 2, we have synthesize $BiNi_{0.25}Ti_{0.25}Fe_{0.5}O_3$ (BNTFO) in which equal mole ratio of Ni and Ti are substituted on the B sites of BFO.

7.2 Experimental details

BNTFO was prepared by a two-step process of milling and thermal annealing. The precursors were high purity Bi_2O_3 (99%), NiO (99.8%), TiO_2 (99.8%) and Fe_2O_3 (99%) supplied by Sigma Aldrich. The oxides were weighed according to expected stoichiometry. Approximately 5 grams of well-mixed powdered oxides were charged in a 250 ml stainless steel jar containing 9 mm diameter hardened stainless steel balls in a ball to mass ratio of 10:1. The sample was milled in air atmosphere using a Retch planetary ball mill (type: PM 400 MA) operated at 300 rpm for 5 hours. The milled powder was annealed at 750 °C for 6 hours at a heating rate of 5 °C/min in a Sentro Tech furnace. The X-ray diffraction (XRD) patterns after annealing were obtained using CoKα radiation (1.7903 Å) on a Philips diffractometer (type: PW 1710) in 2θ steps of 0.008°. The Mössbauer spectrum was acquired at room temperature at about 300 K using a conventional constant acceleration spectrometer with a ^{57}Co source sealed in Rh matrix. Magnetization measurements were performed in the range of 10 to 300 K on a 5 Tesla mini cryogenic free measurement system purchased at Cryogenic Limited, UK. The microstructure and morphology were investigated using high resolution electron microscopy (HRTEM) and field emission scanning electron microscopy (FESEM) on a Zeiss Evo LS15 instrument.

7.3 Results and discussion

7.3.1 Structural and morphology analyses

The XRD pattern of BNTFO is shown in Figure 7.1. Majority of the Sharp prominent peaks belong to the perovskite structure. However, the presence of small impurity peaks indicates that the materials contain some impurity phases such as $Bi_5Fe_4O_9$ and $Bi_{25}FeO_{40}$ which have been reported to be observed in a bismuth ferrite sample of the same composition [113]. Furthermore, some of the impurity phase peaks were indexed using $Bi_5Ti_3O_{15}$ with space group *A-22a*. However, the current XRD pattern indicates a relatively improved structure when compared to that synthesized by Shukla *et al.* The sharp peaks indicate relatively large crystalline sizes which are expected due to heat treatment at 750 °C.

The majority of the prominent peaks are equivalent to perovskite structure but differ-

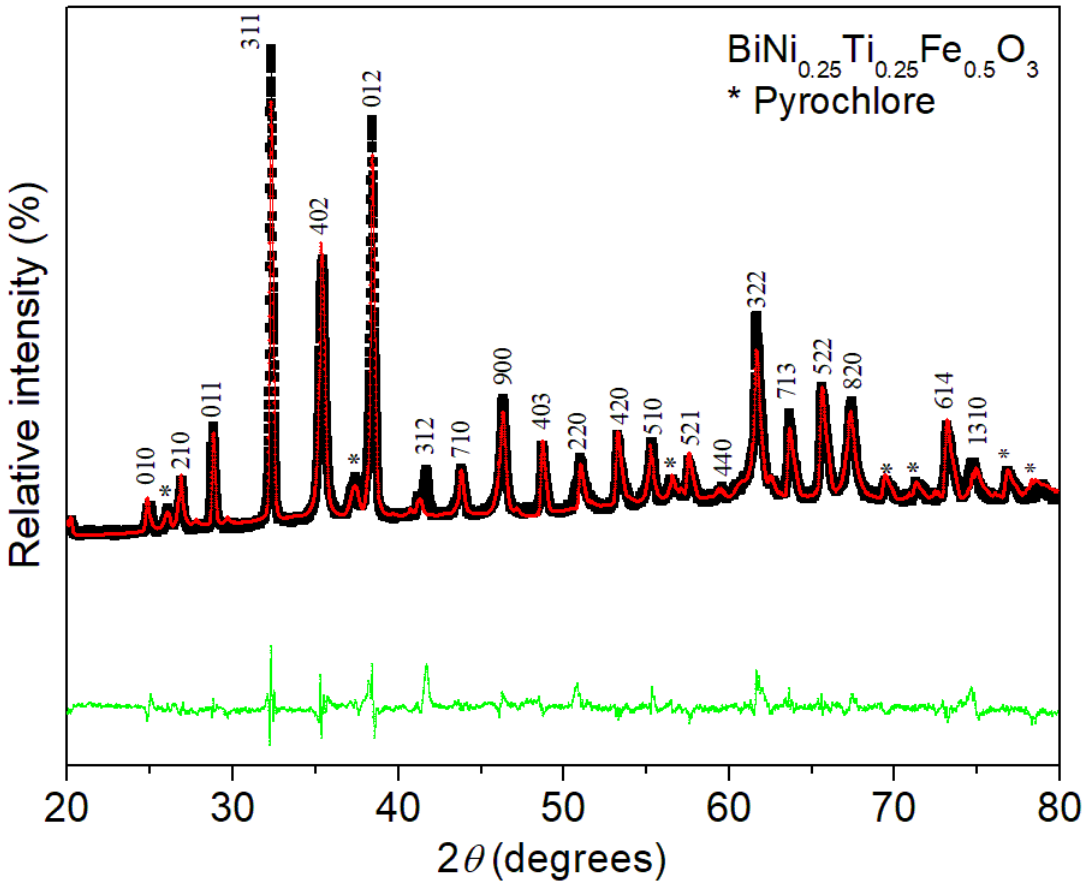

Figure 7.1: XRD pattern of BNTFO sample.

ent from those of the starting precursors indicating a new polycrystalline phase of the compound BNTFO formed [21]. The splitting of peaks at higher 2θ angles confirms the existence of an orthorhombic crystal system. The Goldschmidt tolerance factor t for the BNTFO compound was estimated to be 0.87 using equation 6.3.2. The best fitting model chosen using Match software for Reitveld refinement is that of bismuth ferrite with space group *R3-2"C* with a majority of the prominent peaks being indexed. Table 7.1 shows the comparison of the lattice parameters and volume for the as-prepared compound of BNTFO (B2) to that reported in literature (B1) of the same compound. The lattice parameters for both compounds are in relative agreement. The density of the as-prepared sample is 9 g/cm^3. Figure 7.2 shows FESEM micrographs of the as-prepared BNTFO sample. The grain size varies from large to small and semi-circular in shape with distinct grain boundaries. electrical properties have been reported to be influence by the presence of grains and grain boundaries [114]. The grains show a relatively good surface coverage. The FESEM micrographs indicate the existence of a polycrystalline sample. Nanorod like features are also observed in the morphology of the sample. EDX spectra shown in Fig-

ure 7.3 confirm the presence of all elements of the compound BNTFO. TEM micrographs shown in Figure 7.4 substantiate results from FESEM with semi-spherical particle shapes.

Table 7.1: Comparison of as-prepared BNTFO compound to that reported in literature.

	Lattice Parameters			Volume
	a (Å)	b (Å)	c (Å)	(Å^3)
B1	20.467 (4)	4.151 (4)	7. 145 (4)	606.94
B2	18.120 (1)	5.4491 (2)	7.5497 (2)	660 (5)

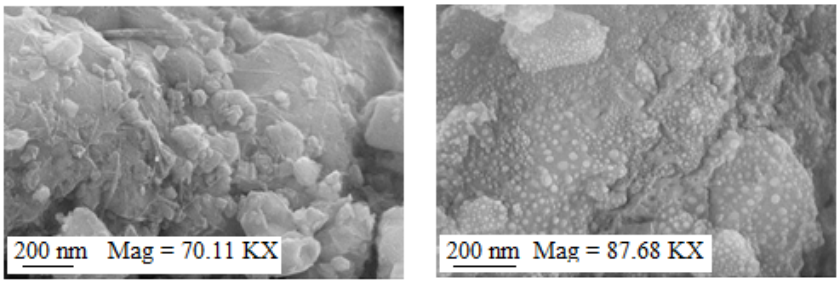

Figure 7.2: FESEM micrographs of the BNTFO sample.

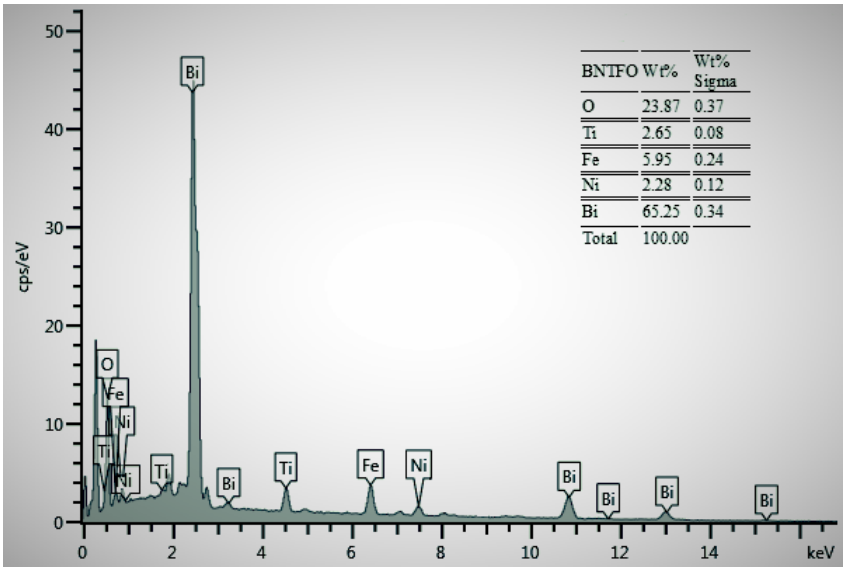

Figure 7.3: EDX spectra of the compound BNTFO.

TEM was also perfomed to determine the particle sizes and particle distribution for the as-prepared BNTFO. Particle size distribution is within the nano-range. Particles appear

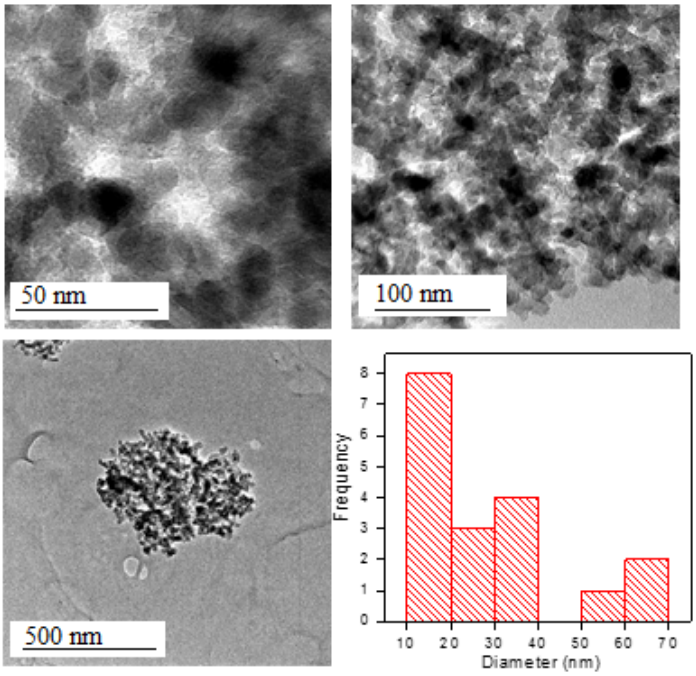

Figure 7.4: TEM micrographs of the BNTFO sample.

to be clustered at different regions of the sample. The strain estimated from the slope of the Williamson-Hall plot was obtained to be 0.0024±0.0008 using the strong reflection peaks (311, 402, 012, 322, 522).

7.3.2 Mössbauer and Magnetization

Magnetization measurements were conducted at temperatures ranging from 300 - 10 K in an applied field of up to 50 kOe. For the present purposes we have chosen a few of the temperature points. The hysteresis loops illustrated in Figure 7.5 show soft ferromagnetic behavior. The inset on Figure 7.5 indicates increasing coercive field with decreasing temperatures. Table 7.2 shows the variation of the saturation magnetization M_S, coercivity H_C, remnant magnetization M_R and squareness R with temperature for the annealed sample of BNTFO. Graphical presentations are shown in Figure 7.6. Saturation magnetization is relatively enhanced compared to $LaNi_{0.25}Ti_{0.25}Fe_{0.5}O_3$. M_S was estimated according to the law of approach to saturation magnetization. The coercive field increases with decreasing temperature. The values of M_S, H_C and M_R are observed to be enhanced in comparison to some of the known multiferroics such as BFO and $Bi_{1-x}Ho_xFeO_3$ (x = 0.15 and x = 0.20) [115]. The substitution of Ni and Ti in BFO enhances magnetic ordering which is evident from the enhancement in remnant magnetization and coercivity.

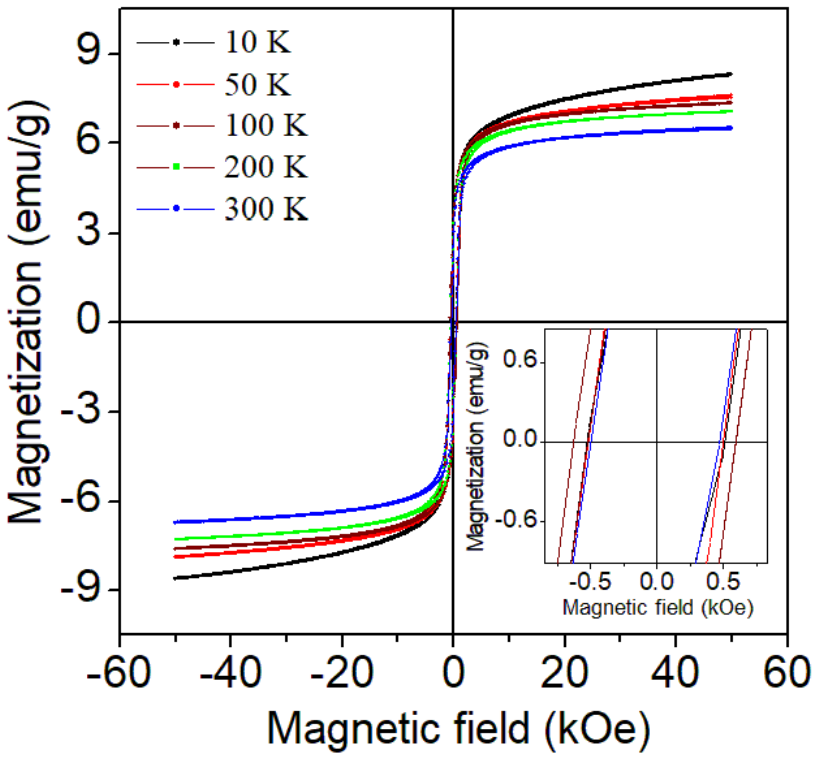

Figure 7.5: Hysteresis loops of BNTFO sample at temperatures between 10-300 K.

Table 7.2: Variation of Saturation magnetization M_S, coercive field H_C, remanence magnetization M_R and squareness R with temperature for the annealed BNTFO.

T (K)	M_S (emu/g)	H_C (kOe)	M_R (emu/g)	R
	±0.21	±0.02	±0.1	±0.14
10	7.32	0.62	3.1	0.43
50	7.27	0.51	2.9	0.41
100	7.22	0.61	3.0	0.42
200	7.02	0.55	2.6	0.37
300	6.47	0.49	2.5	0.38

^{57}Fe Mössbauer spectroscopy at room temperature was used to investigate the hyperfine magnetic field and the oxidation state of Fe. The Mössbauer spectra were fitted using two sextets and one doublet. The doublet parameters are isomer shift IS = 0.37±0.02 mm/s, quadrupole spitting QS = 0.60±0.03 mm/s, line width Γ = 0.20±0.02 mm/s and Fe^{3+} fractional population f = 17±1 %. Table 7.3 shows extracted data for the two fitted sextets shown in the Mössbauer spectra in Figure 7.7.

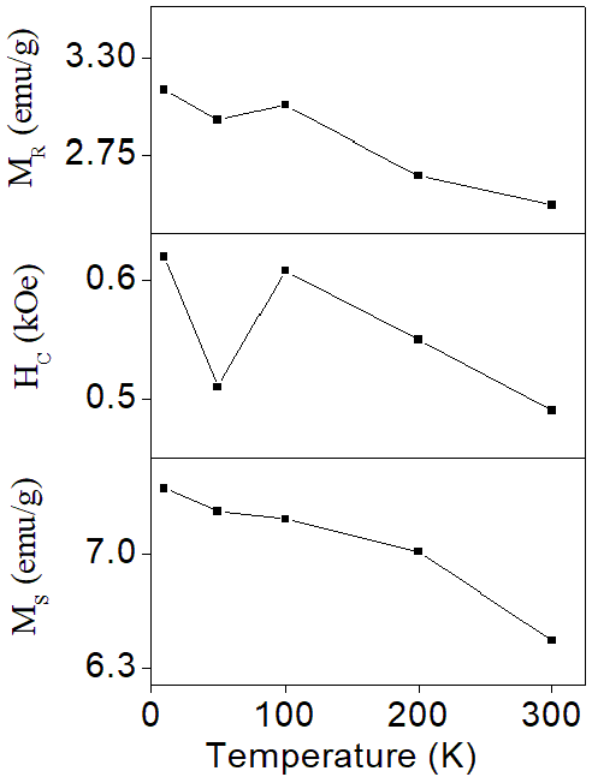

Figure 7.6: M_S, H_C and M_R at different temperatures for as-annealed BNTFO sample.

Table 7.3: Room temperature Mössbauer parameters for the two fitted sextets of prepared BNTFO sample for A and B sites.

H (kOe)		IS (mm/s)		QS (mm/s)		Γ (mm/s)		f (%)	
H_A	H_B	IS_A	IS_B	QS_A	QS_B	Γ_A	Γ_B	f_A	f_B
±5	±4	±0.03	±0.03	±0.02	±0.03	±0.04	±0.05	±6	±7
518	510	0.49	0.10	-0.08	0.11	0.27	0.30	41	41

The doublet can be related to the equivalence of crystallographic sites that Fe^{3+} cations occupy. The high quadrupole splitting indicates effect of the high electric field gradients (EFG) on ^{57}Fe nuclei. According to the isomer shift values iron ions exist in the state of only Fe^{3+}. The two sextets are attributed to the presence of iron ions on the A and B sites of BNTFO. The high hyperfine are associated with super-exchange interaction between atomic moments. The larger hyperfine value was assigned to the octahedral B sites.

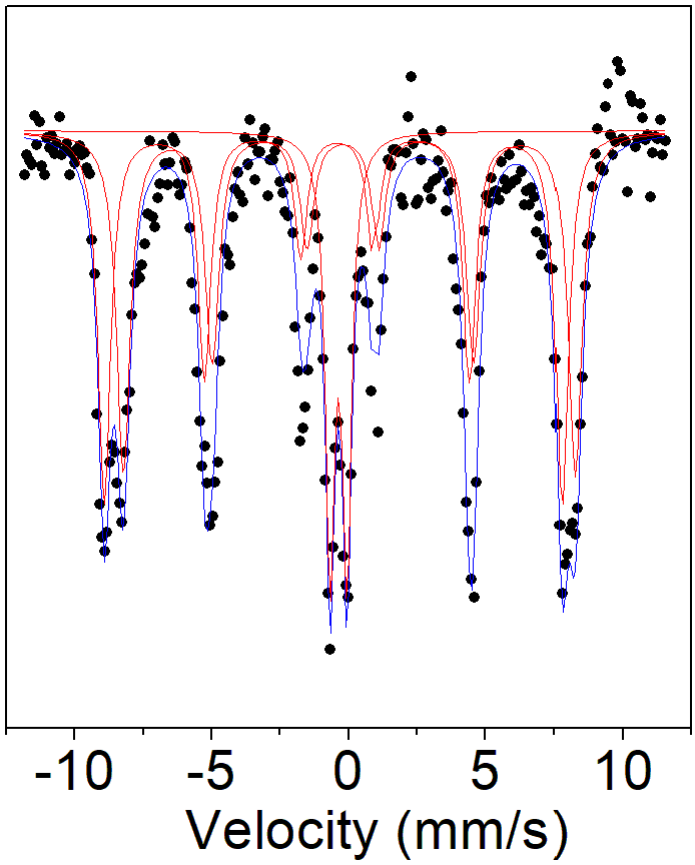

Figure 7.7: Room temperature Mössbauer of BNTFO sample.

7.3.3 Resistivity measurements

Resistivity measurements were conducted in the temperature range 24 °C $\leq T \leq$ 100 °C using the four probe technique. The sample was pressed into a pellet at 2000 psi for 4 minutes and annealed at 200 °C for 2 hours. Figure 7.8 illustrate a plot of ln ρ verses T^{-1}.

Activation energy of 0.66±0.02 eV was determined from the slope of Figure 7.8. The resistivity was assumed to follow Arrhenius equation. Simultaneous substitution of Ni and Ti tend to increase the activation energy as compared to some bismuth base ferrites reported in literature [116, 114]. The low electrical resistivity may be linked to the presence of impurities [117].

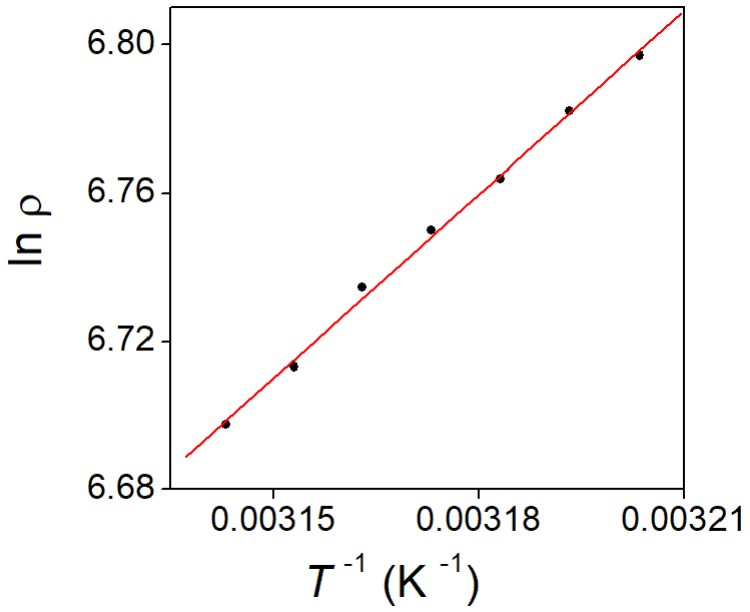

Figure 7.8: Plot of ln ρ verses T^{-1} for as - prepared BNTFO.

7.4 Conclusion

In this work, we presented a novel synthesis approach compared to that of Shukla *et al* [113]. In which they synthesized the same compound of BNTFO by mixing high purity precursors (carbonate and oxides) using agate mortar and pestle in air for 8 hours and in methanol for 10 hours and calcined at 750 °C for 6 hours. The improved polycrystalline sample of BNTFO was successfully synthesized by high energy ball milling for 5 hours and thermal treatment at 750 °C for 6 hours. The simultaneous substitution of (Ni, Ti) on the B sites of BFO resulted in a significant increase in saturation and remnant magnetization. The presence of only Fe^{3+} iron ions have been observed. The particle size varied between 10 - 70 nm. Activation energy was obtained to be 0.66±0.02 eV and the absorber surface morphology showed a relatively good grain coverage.

Chapter 8

Structural, electrical and magnetic characterization of $SrNi_{0.25}Ti_{0.25}Fe_{0.5}O_3$ perovskite

8.1 Introduction

Perovskite type oxides have been receiving considerable attention due to their thermal stability, ideal band gap and the different sizes between the cations at A and B that sites allow their chemical formula to be easily manipulated to permit enough control on the semiconductor properties. Currently, perovskites of the type $AFeO_3$, where A is a rare earth or alkaline-earth metal are amongst the most intensively studied materials due to their unusual physical properties which are significantly influenced by compositional variations [118, 119]. The perovskite $SrFeO_3$ (SFO) has been reported to have potential applications in gas sensors [120]. Perovskite oxides exhibiting high electrical conductivity at high temperatures are interesting for their potential applications in high temperature solid oxide fuel cells and gas sensing materials. On a fundamental point of view, SFO has the potential to exhibits the unstable Fe^{4+} which reduces to Fe^{3+} in a process of homovalent doping resulting in oxygen vacancies [121]. Depending on the oxygen content, SFO exhibits single phases in four different structures namely cubic $SrFeO_3$, tetragonal $Sr_8Fe_{8O2}O_3$ corresponding to $SrFeO_{2.875}$, orthorhombic $Sr_4Fe_4O_{11}$ corresponding to $SrFeO_{2.75}$ and brownmillerite type $Sr_2Fe_2O_5$ which has been reported to be that of $SrFeO_{2.5}$ [122]. Amongst numerous perovskite oxides, SFO exhibits unusual structural,

magnetic, electronic and transport properties [22, 123].

Materials having Ni and Ti at approximately equal proportions $NiTiO_3$ have been reported to have potential applications in sensors, fuel cells and photo-catalysis [88]. The alloy nitinol NiTi also exhibits rather strange but fascinating characteristics. We have therefore synthesized $SrNi_{0.25}Ti_{0.25}Fe_{0.5}O_3$ perovskite in which nearly equiatomic Ni-Ti is substituted to the B site of $SrFeO_3$. To our knowledge studies of SNTFO compound have not been reported in the literature.

8.2 Experimental details

The SNTFO compound was prepared by a two-step process of milling and thermal annealing. The starting compounds were high purity SrO (99.8%), NiO (99.8%), TiO_2 (99.8%) and Fe_2O_3 (99%) purchased from Sigma Aldrich. The oxides were weighed according to the expected stoichiometry. About 5 grams of well-mixed powdered oxides were charged in a 250 ml stainless steel jar containing 9 mm hardened stainless steel balls in a ball to mass ratio of 10:1. The sample was milled on a high energy Retsch PM 400 MA type planetary ball mill operated at 300 rpm for 5 hours. The milled powder was annealed at 1000 °C for 6 hours at a heating rate of 5 °C/min in a Sentro Tech furnace. The X-ray diffraction (XRD) patterns after annealing were obtained using CoKα radiation (λ = 1.7903 Å) on a Philips diffractometer (type: PW 1710) in 2θ steps of 0.008°. The Mössbauer spectrum was acquired at room temperature at about 300 K using a conventional constant acceleration spectrometer with a ^{57}Co source sealed in Rh matrix. The magnetization measurements were performed in the range 10 to 300 K on a 5 Tesla mini cryogenic free measurement system. The microstructure and morphology of the sample were investigated using high resolution electron microscopy (HRTEM) and field emission scanning electron microscopy (FESEM).

8.3 Results and discussion

8.3.1 Structural and morphology analysis

A single phase XRD pattern of SNTFO is shown in Figure 8.1. The best fitting perovskite model used to refine the perovskite structure is an orthorhombic crystal system belonging to space group *-P 2c 2ab*. The refinements were performed using a fullprof program. Lattice parameters obtained from the refinement are $a = 5.4287 \pm 0.0006$ Å, $b = 5.4755 \pm 0.0006$ Å and $c = 7.6819 \pm 0.0008$ Å. The density and direct cell volume are 4.408 g/cm^3 and 228.341 ± 0.044 Å^3. It is well known that the relative size of ions comprising a perovskite compound determines its symmetry. The tolerance factor t calculated for this compound is 0.95.

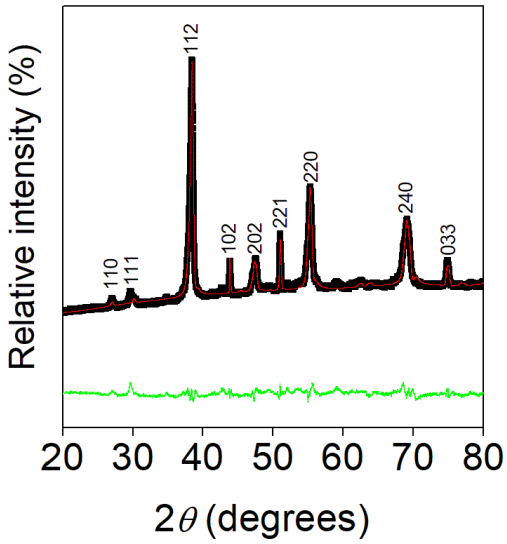

Figure 8.1: Room temperature XRD pattern of SNTFO.

The FESEM micrographs shown in Figure 8.2 reveal information about the quality of the absorber layer for the perovskite SNTFO sample. Grain sizes vary from small to large and are of roughly semi-spherical shapes which is evidence of a polycrystalline morphology consisting of a relatively rough surfaces. EDX spectra in Figure 8.3 confirm the presence of all expected elements of the compound SNTFO. HRTEM micrographs in Figure 8.4 show small particle sizes and confirm crystallinity of the compound SNTFO. The average particle size is obtained from HRTEM is 127 ± 12 nm. The bulk nature of SNTFO is due to high temperature heat treatment during synthesis at 1000 °C.

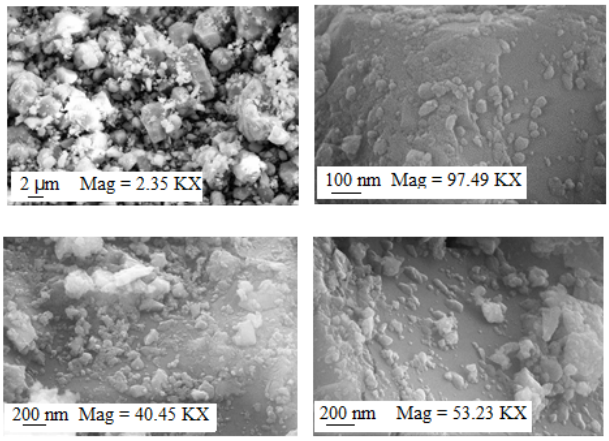

Figure 8.2: FESEM micrograph of SNTFO sample.

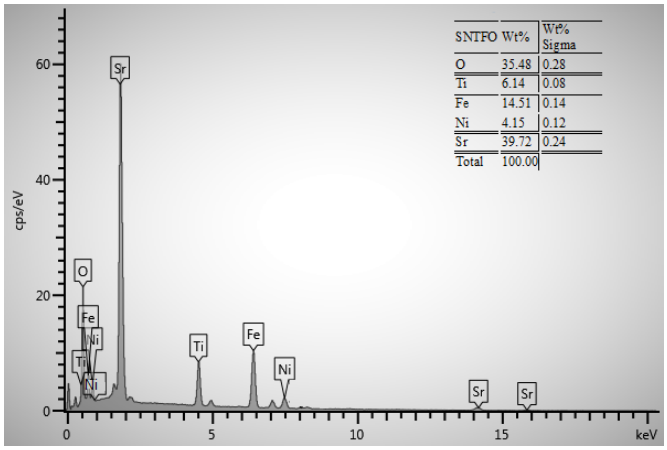

Figure 8.3: EDX spectra of SNTFO sample.

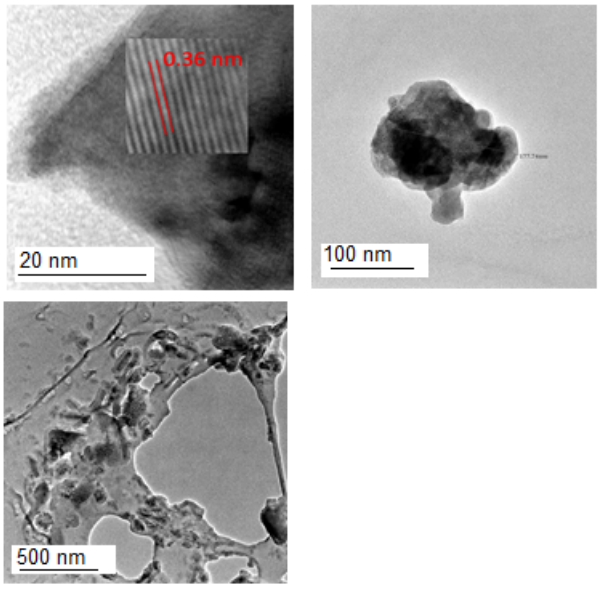

Figure 8.4: HRTEM micrography of SNTFO sample.

8.3.2 Mössbauer and Magnetization

Magnetization measurements were conducted in the temperature range 10 K to 300 K in an applied field of up to 50 kOe. The hysteresis loops are presented in Figure 8.5. Table 8.1 shows the variation of saturation magnetization, coercive field, remnant magnetization and squareness with temperature for the annealed SNTFO sample extracted from the hysteresis loops. The saturation magnetization M_S at 300 K and 200 K is very close to zero with very small values of H_C and M_R, this is typical of paramagnetic behavior. However, from 100 K to 10 K, M_S and H_C increases. The sigmoidal shape hysteresis loops at this range together with the small values of M_R is indicative of super-paramagnetic behavior.

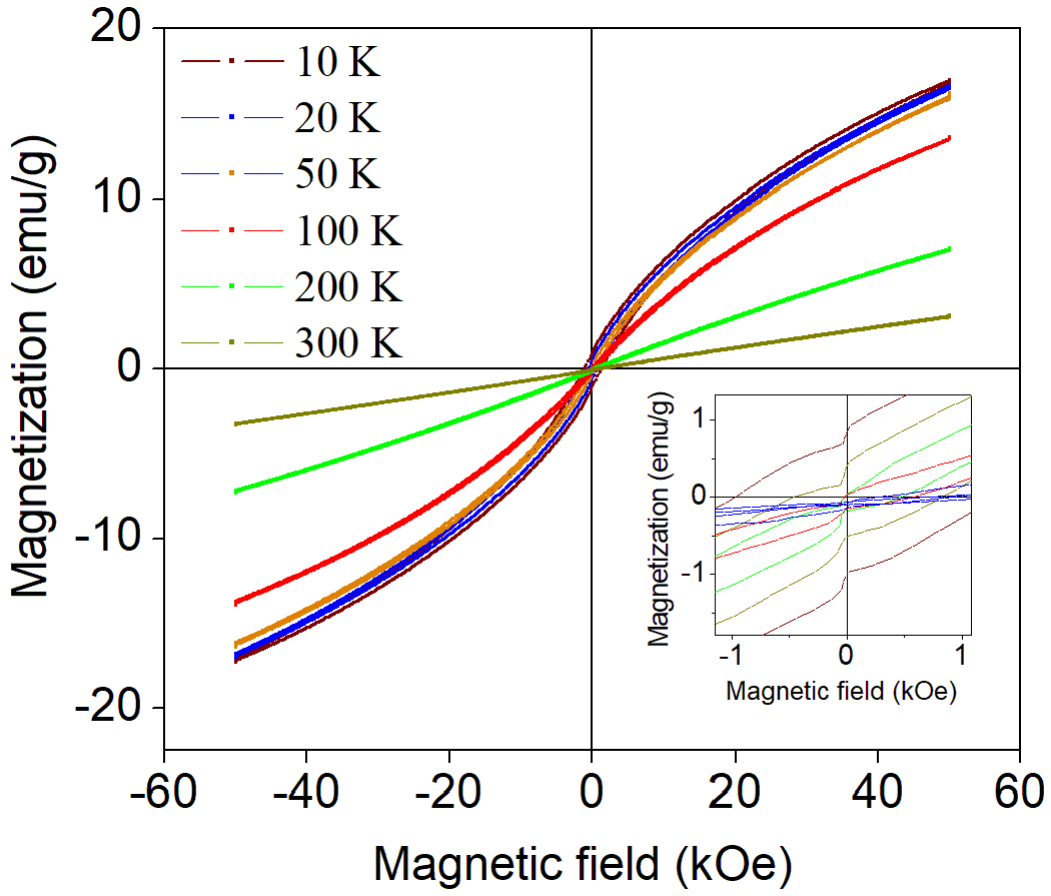

Figure 8.5: Hysteresis loops of SNTFO sample at temperatures between 10-300 K.

The room temperature Mössbauer spectra shown in Figure 8.6 indicates paramagnetic behavior for the compound SNTFO and was fitted by two doublets. The paramagnetic behavior at room temperature is well supported by the hysteresis loop of the compound at room temperature. The corresponding fit parameters are shown in Table 8.2. Isomer

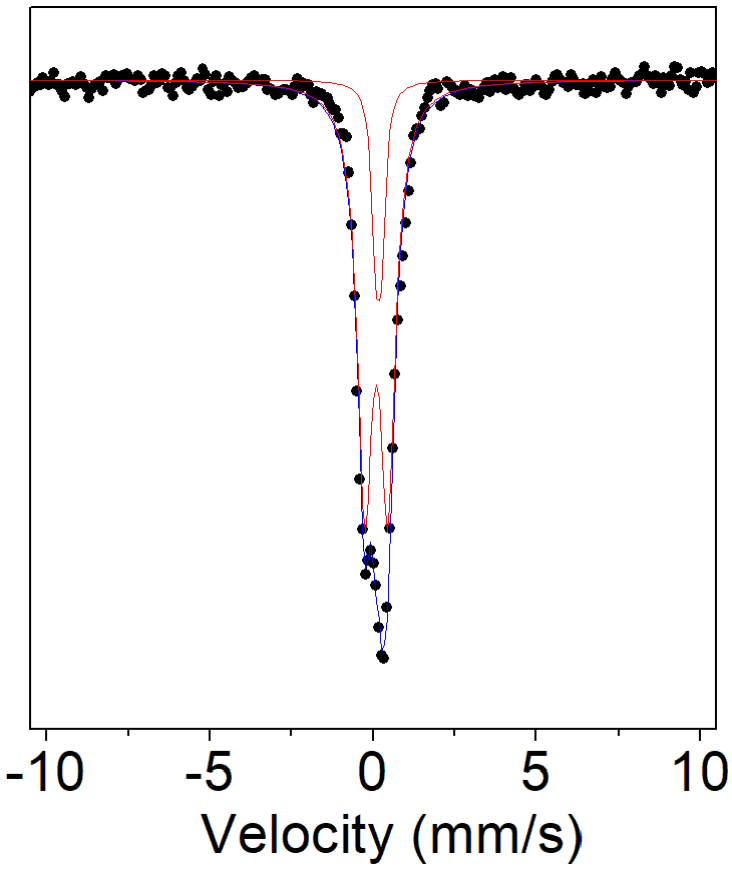

Figure 8.6: Room temperature Mössbauer of as prepared SNTFO sample.

Table 8.1: Variation of Saturation magnetization M_S, coercive field H_C, remanence magnetizationM_R and squareness R with temperature for the annealed SNTFO.

T (K)	M_S (emu/g)	H_C (kOe)	M_R (emu/g)	R
	±0.23	±0.06	±0.11	±0.001
10	14.13	1.14	0.92	0.065
20	11.39	0.65	0.44	0.039
50	11.26	0.24	0.09	0.008
100	9.67	0.29	0.08	0.008
200	1.94	0.32	0.02	0.010
300	0.003	0.34	0.01	3.333

shift IS values for high spin Fe^{2+}, Fe^{3+}, Fe^{4+} and Fe^{6+} ions lie within the characteristic ranges 0.6 - 1.7 mm/s, 0.1 - 0.6 mm/s, -0.2 - 0.2 mm/s and -0.8 - -0.9 mm/s respectively [124]. Hence, the IS in doublets 1 is attributed to possible combination of Fe^{3+} and Fe^{4+}

Table 8.2: Room temperature Mössbauer parameters for the two fitted singles of prepared SNTFO sample.

Fit	IS (mm/s)	QS	Γ (mm/s)	f (%)
Doublet 1	0.098 (7)	0.71 (2)	0.27 (1)	83.4 (56)
Doublet 2	0.20 (1)	0.18 (3)	0.14 (2)	16.6 (50)

which corresponds to $Fe^{3.5}$ ions [125] and the quadrupole doublet 2 is typical of Fe^{3+}. The two doublets are possibly have similar signature to that of orthorhombic $Sr_4Fe_4O_{11}$ phase [125]. The molar fractional population of Fe^{3+} and Fe^{4+} on doublet 1 calculated from peak area is obtained to be 83.4 ±5.6 % and that of doublet 2 is 16.6±5.0 %.

8.3.3 Resistivity measurements

The four probe method was used to conduct resistivity measurements in the temperature range 24 °C $\leq T \leq$ 100 °C. The resistivity was assumed to follow Arrhenius equation. The 0.7 grams of sample was pressed into a pellet at 2000 psi for 4 minutes. Figure 8.7 shows a plot of ln ρ versus T^{-1}.

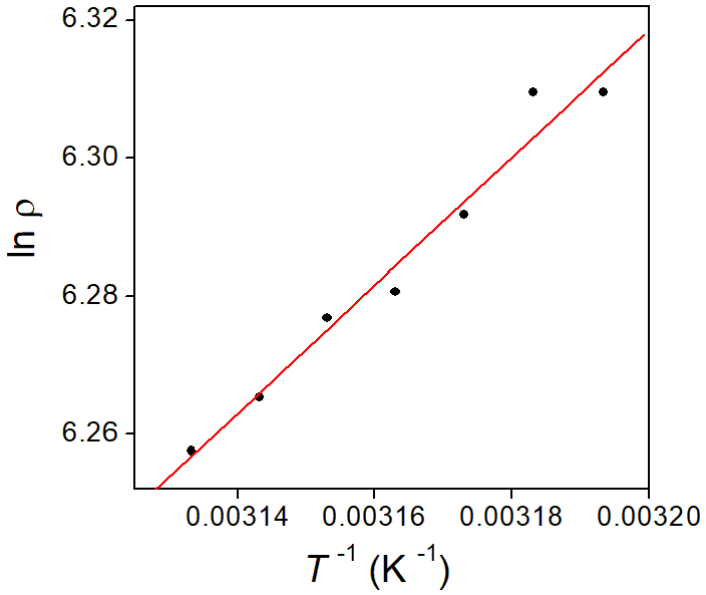

Figure 8.7: Plot to estimate activation energy for SNTFO sample.

Activation energy of 0.37±0.03 eV was obtained from the slope of Figure 8.7 that indicates

semiconducting behavior and good electrical conductivity at relatively high temperatures. However, the activation energy is relatively higher than that reported for $SrFeO_{3-\delta}$ thin films [126]. It has also been reported that perovskite oxides exhibiting high electronic conductivity at relatively higher temperatures are interesting for their potential applications in high temperature solid oxide fuel cells and gas sensing materials. In the case of gas sensors, they represent an alternative for resistive type sensors based on SnO_2, TiO_2 and CeO_2–ZrO_2 semiconducting oxides [127, 128, 129].

8.4 Conclusion

$SrNi_{0.25}Ti_{0.25}Fe_{0.5}O_3$ (SNTFO) belonging to an orthorhombic crystal system was successfully synthesized using high energy ball milling and thermal annealing at relatively high temperatures. The material shows paramagnetic behavior at room temperature whilst at lower temperatures it is superparamagnetic. Magnetization M_S is relatively low ranging from 14.14 to 0.003 emu/g and the coercive field increased with decreasing temperature. Mössbauer spectra indicate the presence of both Fe^{4+} and Fe^{3+} ions which are consistent with those reported for SFO compounds. Particle size obtained from HRTEM averaged 127±12 nm and the surface morphology is indicative of a rough absorber surface with semi-spherical grains of different sizes. Activation energy of 0.37±0.03 eV is indicative of good electronic conductivity at relatively high temperature. This is one of the good characteristic requirements for a good gas sensor [107, 4]. However, we would still expect to improve material performance by regrinding the material without destroying the phase in order to increase the surface area, reduce agglomeration and reduce particle size. Increase surface by milling is expected to increase absorber surface area and improve sensing characteristic of the sample.

Chapter 9

Synthesis, structural and magnetic properties of $Ni_{0.5}Ti_{0.5}Fe_2O_4$

9.1 Introduction

Ferrites of the spinel structure have the general formulae AB_2O_4 where A and B are usually the divalent and trivalent cations occupying the tetrahedral (A) and octahedral (B) interstitial positions. Their magnetic properties are heavily governed by the cations distribution between the two interstitial positions. The cation distribution and resulting magnetic properties of nano-ferrites are interesting and different from those of their bulk counterparts [130]. The interesting properties possessed by nano-ferrites makes them useful in numerous applications such as magnetic fluids, solar cells, sensors and catalysis [131]. Nickel base ferrites of the spinel structure has been reported to have interesting properties such as low coercivity, high saturation magnetization, chemical and thermal stability [132]. These qualities allow the materials to be used in applications such as gas sensors, magnetic fluids, magnetic storage systems [133, 134]. The properties of $NiFe_2O_4$ can be tuned by doping in the A or B sites of the spinel structure. Furthermore, the synthesis technique used has great influence on the resulting properties. In this work we investigated the structural and magnetic properties of $Ni_{0.5}Ti_{0.5}Fe_2O_4$ (NTFO) synthesized by high energy ball milling technique.

9.2 Experimental details

The $Ni_{0.5}Ti_{0.5}Fe_2O_4$ sample was prepared by high energy mechanical milling. The starting precursors purchased at Sigma Aldrich were Fe_3O_4 (99.99%), NiO (99.8%), and TiO_2 (99.8%). The materials were weighed according to calculated stoichiometry. Approximately 5 grams of well mixed powdered oxides were charged in a 250 ml stainless steel jar containing 9 mm hardened steel balls in a ball to mass ratio of 10:1. The sample was milled in air atmosphere using a Retch planetary ball mill (type: PM 400 MA). The high energy ball milling (HEBM) was performed at speeds of 300 rpm for different times of 0.25, 0.50, 1.00, 1.50, 2.00, 5.00 and 10.00 hours. The X-ray diffraction (XRD) patterns were obtained for all allocated times using CoKα radiation (λ = 1.7903 Å) on a Philips diffractometer (type: PW 1710) in 2θ steps of 0.008°. The Mössbauer spectrum was acquired at room temperature using a conventional constant acceleration spectrometer with a ^{57}Co source sealed in Rh matrix. Magnetization measurements at temperatures 10 to 300 K were conducted using a 5 Tesla mini cryogen free system purchased from Cryogenic Limited, UK. The microstructure and morphology were investigated using high resolution electron microscopy (HRTEM) and a scanning electron microscopy (HRSEM). The elemental composition was confirmed using energy dispersive X-ray (EDX) spectroscopy.

9.3 Results and discussion

9.3.1 Structural and morphology analyses

Figure 9.1 shows the XRD pattern of the as-prepared NTFO sample. A secondary impurity peak at 29° has been matched to TiO_2 using HighScore Plus software [135]. This may be due to unbroken bonds of titanium oxide due to short milling time. To accurately extract important structural information, the XRD peaks for the sample milled for 5 hours was fitted and refined using the best fitting model belonging to a cubic crystal system of space group *–F 4vw 2vw 3*. The best fitting model was obtained using Match software [91]. The Reitveld refinement was carried out using Fullprof Suite program [92, 93]. Lattice parameters, direct cell volume and density of the NTFO compound were determined. The Bragg's structural factor and goodness of fit for the reported refinement are 5.68 and 2.47 respectively.

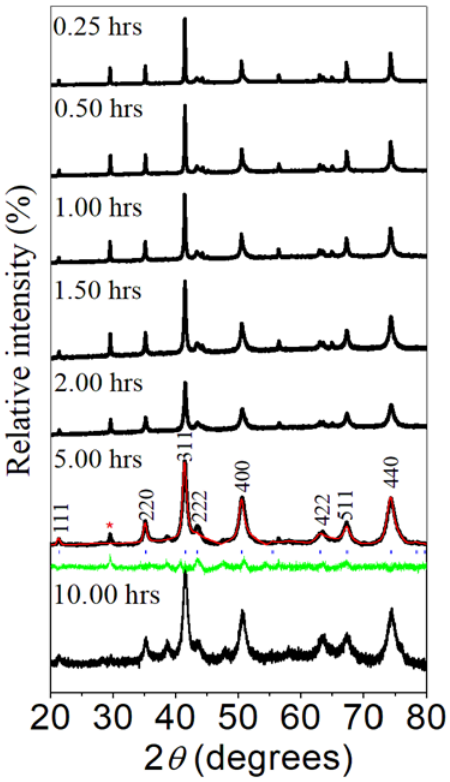

Figure 9.1: XRD pattern of NTFO sample milled at different times.

The refined lattice parameters are 8.3936±0.0001 Å. The bulk direct cell volume and refined density are obtained to be 591.35±0.15 Å^3 and 5.37 g/cm^3 respectively. The average lattice strain obtained from the slope of the Williamson-Hall plot shown in Figure 9.2(a) is 0.0061±0.0002 and the average crystalline size of the compound was estimated from the strong reflection of (311) peak in the XRD pattern and was calculated to be 21.6±1.2 nm using Scherrer's formula. More impurity peaks at 10 hours emerge which is evidence of a structure starting to lose form. Figure 9.2(b) shows that the lattice strain increases with increasing milling time whilst the crystallite size decreases with increasing milling time which is in good agreement with the general behavior of HEBM materials [136, 137]. In Figure 9.2(b) the increasing lattice strains with milling time are due to the fact that during HEBM continuous welding and fracture of the material takes place, causing increased crystal defects such as point defects and dislocations due to plastic deformation of powder particles leading to increased lattice strains as indicated by peak broadening and decrease in peak heights in the XRD patterns [137]. The lattice parameters and density were respectively calculated using Bragg's law [138, 139] and $\rho_{XRD} = \frac{8M}{N_A a^3}$, where M is the molar mass of the sample and N_A is the Avogadro's number [139]. The relation between density

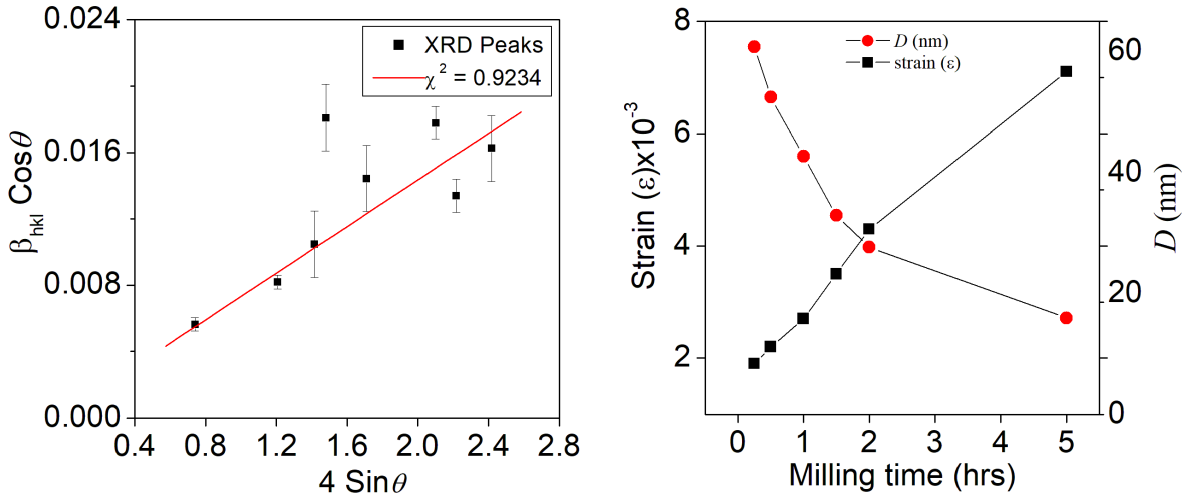

(a) (b)

Figure 9.2: (a) Williamson-Hall plot of β_{hkl} cosθ against 4 sinθ of NTFO spinel. (b) Lattice strain ε and crystallite size D at varying milling times.

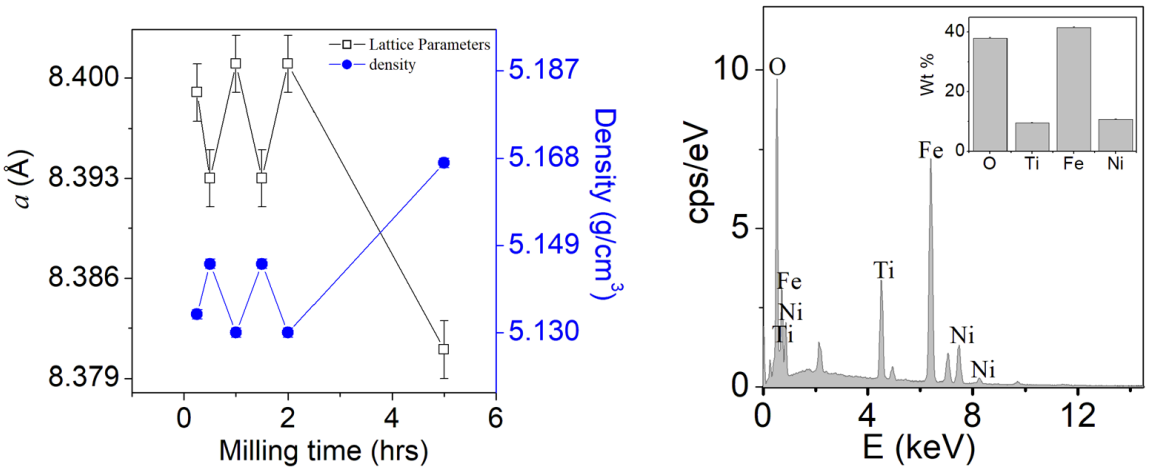

(a) (b)

Figure 9.3: (a) Relation of the Lattice parameters and density at different milling times. (b) EDX elemental composition and atomic percentage of milled NTFO.

and lattice parameters is presented in Figure 9.3(a). Figure 9.3(b) shows peaks corresponding to all expected elements (Ni, Ti, Fe, O). The remaining peaks are of Au used to coat the sample before measurements. The inset in Figure 9.3(b) shows weighted percentages of each element of the compound. The SEM micrographs for as-prepared sample are shown in Figure 9.4 which clearly show densely packed grains of different shapes and sizes.

TEM was conducted to determine crystallite size distribution, average crystallite size and

lattice fringe distributions at different regions of the sample. The crystallite distribution can be observed in Figure 9.5 and the average crystallite size of 45±9 nm was obtained from Imagej software. The inconsistency between the crystallite size obtained from the strong reflection peak (113) and from TEM may be an indication of particle agglomeration. The majority of the crystallites are observed to be in the nano-range 1 to 100 nm whilst a few in the bulk range (>100) nm. The crystallinity of the material is shown in Figure 9.5 with average lattice fringes of 0.21 nm. Figures 9.5 also shows crystals which are relatively loosely packed and are of different sizes and shapes as indicated by SEM micrographs.

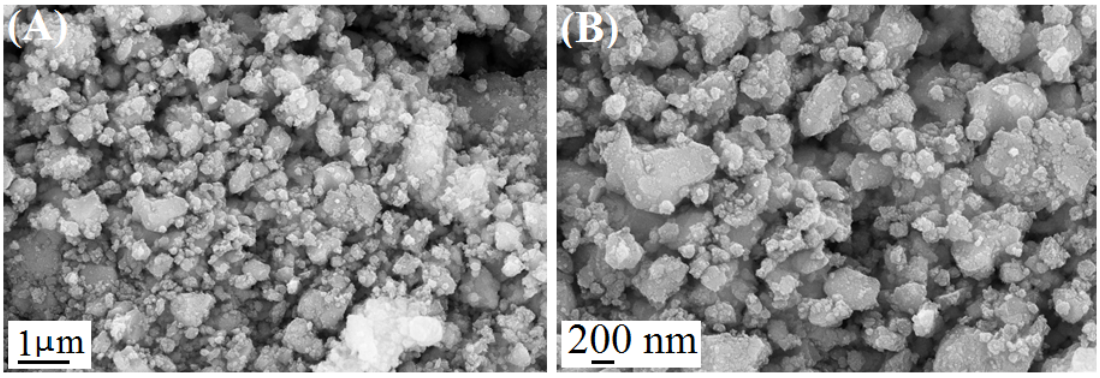

Figure 9.4: SEM micrographs (A), (B) at 10K and 20K magnifications respectively.

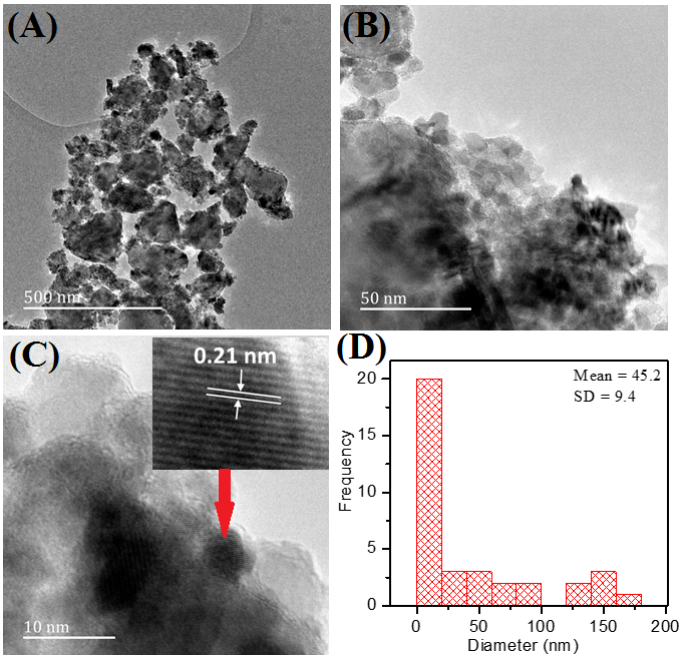

Figure 9.5: (A) and (B) shows TEM micrographs with (C) showing lattice fringes obtained from HRTEM. (D) shows the Particle size distribution.

9.3.2 Magnetisation and Mössbauer meausurements

Magnetization measurements were conducted at temperatures ranging from 10 to 300 K in applied fields of up to 50 kOe. The hysteresis loops presented in Figure 9.6 show typical soft ferromagnetic properties. The unidirectional shifts of the magnetic hysteresis loops along the positive or negative magnetic field axes indicate evidence of exchange bias fields [140]. However, in the NTFO sample no evidence of exchange bias field is observed in the inset of Figure 9.6.

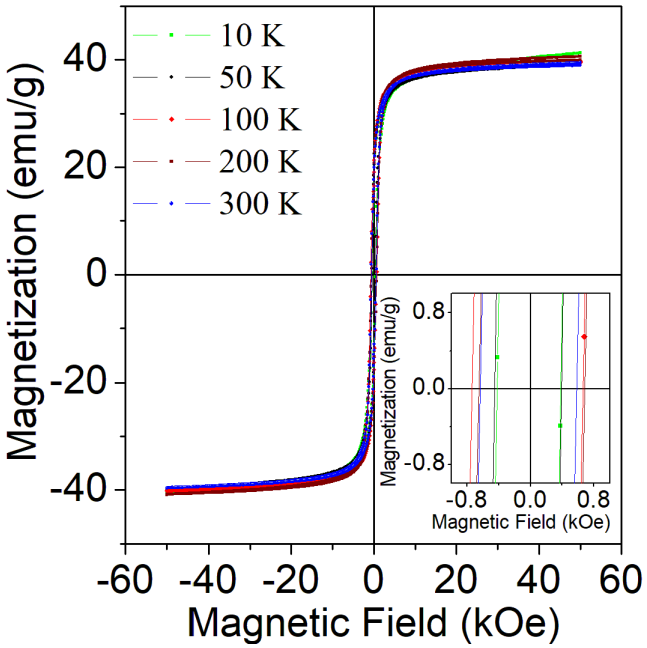

Figure 9.6: Magnetic hysteresis loops of as-milled NTFO at different temperatures.

Table 9.1 shows the variations of M_S, H_C, $M_S H_C$, M_R and squareness R with temperature for the milled NTFO at 5 hours. Interestingly, on close inspection it was observed that the coercivity of the material decreased with decreasing temperature whilst the saturation magnetization slightly increased as illustrated in Figure 9.7. The slight increase in M_S at lower temperatures may be because of the Zeeman energy dominating the thermal energy [141] whilst the coercivity is probably slightly decreasing as a results of decreasing anisotropy field H_A [142]. Figure 9.8 shows a plot of H_C versus $\frac{1}{M_S}$ at temperatures 300 - 10 K for as-milled NTFO sample and it reveals rather intriguing behavior of the material at lower temperature. The plot is based on Stoner-Wohlfarth theory which suggests $H_C = \frac{0.96K}{M_S}$ [143]. The behavior of the material at temperatures 10 K, 20 K and 50 K indicate that the sample's anisotropy constant K is approximately constant which

is rather interesting. The change of larger anisotropy constant K at high temperatures to relatively lower K at low temperature may indicate structural change due to magnetic reversal.

Table 9.1: Variation of M_S, H_C, M_R and R with temperature for as-milled NTFO.

T (K)	M_S (emu/g)	H_C (Oe)	$M_S H_C$ (emu Oe g^{-1})	M_R (emu/g)	R
	± 0.03	± 32	$\pm 1.2 \times 10^3$	± 0.42	± 0.05
300	38.84	820	31.8×10^3	18.34	0.47
250	39.83	646	25.7×10^3	17.84	0.45
200	39.93	664	26.5×10^3	16.92	0.42
150	39.45	653	25.8×10^3	17.35	0.44
100	39.11	697	27.3×10^3	18.32	0.47
50	38.32	422	16.2×10^3	17.67	0.46
20	38.56	412	15.9×10^3	17.32	0.45
10	38.73	407	15.8×10^3	16.16	0.42

^{57}Co Mössbauer spectroscopy at room temperature was used to investigate the hyperfine magnetic field and the oxidation state of Fe. The Mössbauer spectra shown in Figure 9.9 was best fitted using two sextets. Table 9.2 shows the extracted Mössbauer parameters by recoil Mössbauer analysis software. The isomer shift values in the range 0.6 - 1.7 mm/s and 0.1 - 0.5 mm/s have been largely assigned to Fe^{2+} and Fe^{3+} respectively [124]. The isomer shift values for both A and B sites shown in Table 9.2 reveal co-existence of both Fe^{3+} and Fe^{2+}. The hyperfine field H are associated with super-exchange interactions between magnetic moments in A and B sub-lattice. The greater value of the line broadening Γ is suspected to be due to presence of Fe^{3+}. The iron ions fractional population f were obtained to be 59 % and 41 % for A and B sites respectively.

Magnetization reversals are generally possible in ferrites which can give rise to reduced magnetizations at lower temperature. For example in Co_2TiO_4 spinel compounds complex magnetization and magnetic compensation behavior have been observed [144]. The cation distribution is assumed to be of the form: $Co^{2+}[Co^{3+}Ti^{3+}]O_4$ where Co^{2+} occupies tetrahedral (A) sites and $Co^{3+}Ti^{3+}$ the octahedral (B) sites. Three possible interactions exist

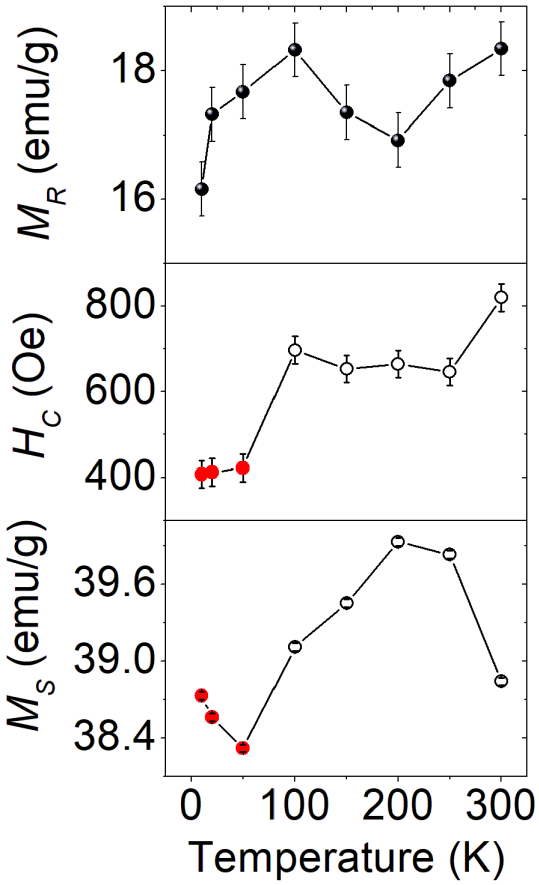

Figure 9.7: M_S, H_C and M_R at different temperatures for as-milled NTFO sample.

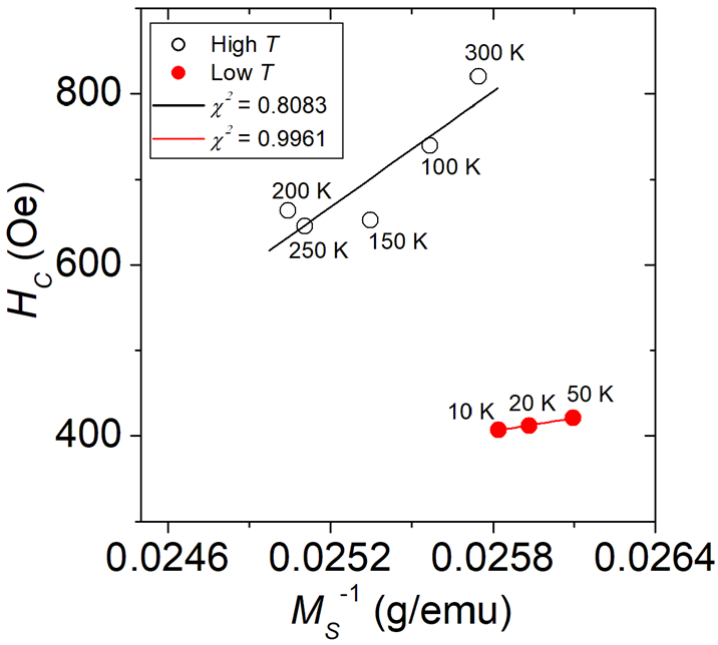

Figure 9.8: A plot of H_C versus $\frac{1}{M_S}$ at temperatures 300 - 10 K for as-milled NTFO sample.

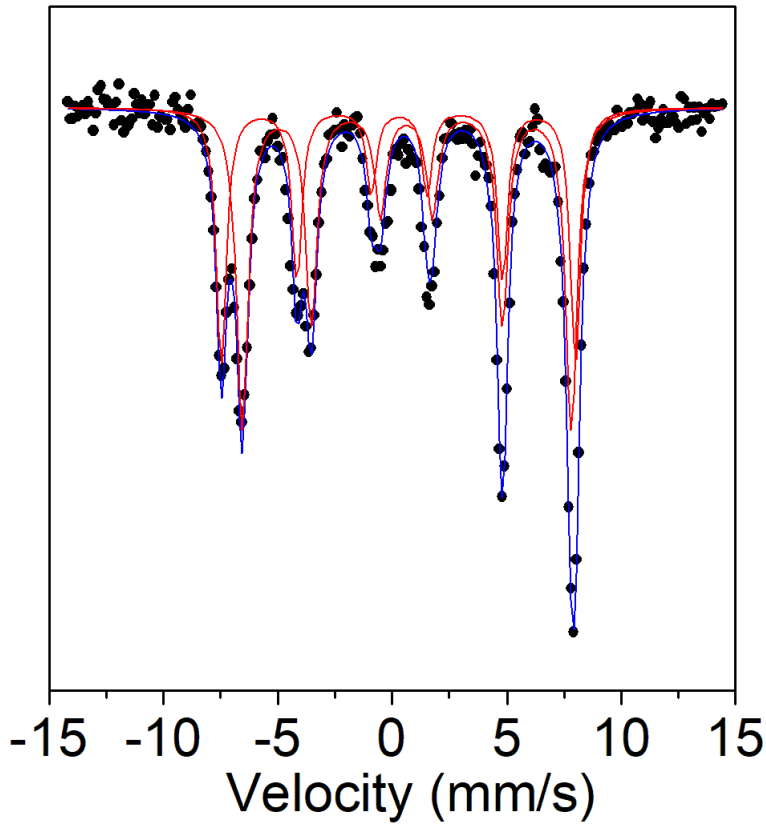

Figure 9.9: Mössbauer fittings of NTFO, measurements at ambient temperature.

Table 9.2: Room temperature Mössbauer parameters of as-milled NTFO sample: H, IS, QS, Γ and Fe^{3+} fractional population f on A an B.

H (kOe)		IS (mm/s)		QS (mm/s)		Γ (mm/s)		f (%)	
H_A	H_B	IS_A	IS_B	QS_A	QS_B	Γ_A	Γ_B	f_A	f_B
±1	±1	±0.01	±0.02	±0.013	±0.025	±0.02	±0.03	±4	±4
446	480	0.63	0.29	0.002	-0.022	0.31	0.27	59	41

namely AA, BB being ferromagnetic and AB antiferromagnetic. This ensures both positive and negative exchange interactions coexist. Magnetization that can collapse at lower temperature was observed which was attributed to spin-flip transitions and continuous crossover effect between negative and positive exchange bias. Similarly in $Ni_{0.5}Ti_{0.5}Fe_2O_4$ (NTFO), a cation distribution of the form $[(Ni^{2+})_{0.5}(Fe^{2+})_{0.5}][(Fe^{3+})_{1.5}(Ti^{3+})_{0.5}]O_4$ for AB_2O_4 spinel structure can be assumed which may also lead to complex magnetization behavior. We have assumed that Ni^{2+} and Fe^{2+} have preference for A sites while Fe^{3+} and Ti^{3+} are assigned to B sites. The cation distribution for NTFO is further confirmed

by the isomer shift values in Table 9.2 of 0.63 mm/s and 0.29 mm/s corresponding to Fe^{2+} and Fe^{3+} respectively [124]. We also note that the internal hyperfine fields in Table 9.2 are 446 kOe and 480 kOe for A and B sites. This appears to be consistent with the proposed cation distribution for NTFO.

9.4 Conclusion

$Ni_{0.5}Ti_{0.5}Fe_2O_4$ nanoferrites were successfully synthesized by mechanical milling HEBM for a relatively short time. The material consists of a secondary phase thought to be associated to TiO_2. Prolonged milling appears to destroy the phase. From the structural analysis it is evident that starting precursors for a chemical reaction are of vital importance as they have great influence on the reaction product. The mean particle size was obtained to be 45±9 nm. The density is inversely proportional to the lattice parameters. The coercivity tends to decrease with temperatures whilst saturation magnetization slightly increases. Isomer shift values revealed co-existence of both Fe^{3+} and Fe^{2+}. Particle sizes reduced with milling time whilst the strain increased. At low temperatures 10 to 50 K the anisotropy constant is approximately constant. The change to larger anisotropy constant K at higher temperatures 100 to 300 K to relatively lower K at low temperatures may indicate structural change due to magnetic reversal. More measurements are required at reduced temperature intervals and in the range 50 to 100 K in order to account and confirm the observed changes in the anisotropy constants in Figure 9.8.

Chapter 10

General conclusions and recommendations

The single phase polycrystalline sample of $LaNi_{0.25}Ti_{0.25}Fe_{0.5}O_3$ (LNTFO) was successfully synthesized via high energy ball milling and high temperature heat treatment. The average crystallite size obtained by HRTEM was 91±5 nm which is expected for a material that was finally thermally heat treated. SEM micrographs indicate that the sample has relatively good surface coverage with semi-spherical grains. Magnetization measurement in the range 10 - 300 K showed soft ferromangetic behavior with M_S in the range 2.25 - 2.61 emu/g and the coercivity increased from 0.36 to 0.41 kOe with decreasing temperature. Generally M_S in pervoskites has been reported to be relatively low. Nevertheless, there is a slight increase in M_S for the reported LNTFO sample when compared to $LaFeO_3$ (LFO) samples reported in literature. The slight increase in magnetization maybe due to the presence of uncompensated spin of Ni^{2+} and Fe^{3+}. Mössbauer data revealed the sample has some magnetic ordering at room temperature. The isomer shift values indicate possible strong covalent bonds between metal and the oxygen ions and only Fe^{3+} ions exist. The activation energy 0.90±0.06 eV was obtained from resistivity measurements. This low activation energy at relatively higher temperatures may play significant role in sensing. However, specific surface area of 6.93±0.04 m^2/g for the as prepared sample may be further improved by performing reactive grinding would also reduce particle sizes in the process.

An improved polycrystalline sample of $BiNi_{0.25}Ti_{0.25}Fe_{0.5}O_3$ (BNTFO) was successfully

synthesized by milling for 5 hours at 300 rpm and followed by thermal annealing for 6 hours at 750 °C. Some secondary phases were indexed to $Bi_5Fe_4O_9$ and $Bi_{25}FeO_{40}$ which have been reported to be present in $BiFeO_3$ (BFO). Some small extra peaks matched and indexed to $Bi_5Ti_3O_{15}$. The crystallite size were found in the range from 10 to 70 nm and some grains agglomerated with semi-spherical shapes ranging from relatively small to large. Improved magnetization measurements were observed relative to LNTFO sample with M_S for the as-prepared sample ranging from 6.47 to 7. 32 emu/g and coercivity ranging from 0.49 to 0.62 kOe at room temperature. The hysteresis loop of BNTFO shows typical soft ferromagnetic behavior. Mössbauer revealed magnetic ordering at room temperature. Only the presence of Fe^{3+} iron ions are indicated by the isomer shift values. Magnetic hyperfine values of 518±5 kOe and 510±4 kOe were attributed to the presence of iron ions in the A and B sites respectively. The relatively higher hyperfine value is associated with super-exchange interaction between atomic moments. An activation energy of 0.66±0.02 eV was determined from the slope of ln ρ verses T^{-1}.

$SrNi_{0.25}Ti_{0.25}Fe_{0.5}O_3$ belonging to an orthorhombic crystal system was also successfully synthesized by using high energy ball milling and thermal annealing at 1000 ° for 6 hours. The material shows paramagnetic behavior at room temperature whilst at lower temperatures its superparamagnetic. The magnetization M_S is relatively low ranging from 14.14 emu/g to 0.003 emu/g and the coercive field increases with decreasing temperature. Mössbauer spectra indicate the presence of both Fe^{4+} and Fe^{3+} ions which are consistent to those reported for $SrFeO_3$ (SFO) compounds. Particle sizes obtained from HRTEM averaged 127±12 nm and the surface morphology is indicative of a rough absorber surface with semi-spherical grains of different sizes. The activation energy of 0.37±0.03 eV is indicative of good electronic conductivity at relatively higher temperature. This is a one of the good characteristic requirement for good gas sensor. However, the material perfomance is also likely to improve by soft regrinding the materials so as to avoid destroying the phase and in the process increase surface area, reduce agglomeration and reduce particle size. The increase in surface coverage in this regard would influence the absorber surface of the gas molecules and improved sensing properties.

Comparing the three samples SNTFO, BNTFO and LNTFO we observed that the acti-

vation energy is highest for SNTFO and the magnetization increased with simultaneous substitution of Ni and Ti indicating B sites substitution has significant influence on the magnetic behavior of the materials. The synthesis technique is common for these samples and it been observed that materials synthesized using these two techniques (ball milling and heat treatment) tend produce polycrystalline samples.

Polycrystilline $Ni_{0.5}Ti_{0.5}Fe_2O_4$ has been successfully synthesized by mechanical milling for a relatively short time. We have found strong correlation between coercive fields H_C and saturation magnetization M_S that is consistent with the Stoner - Wohrfarth theory. Our results show anisotropy constants in two distinct temperature ranges (low and light) that vary little with temperature.

10.1 Future work

In this work it has been shown that it is possible to synthesize single phase Ni-Ti substituted perovskites. Ferrite perovskites such SFO, LFO and BFO have been reported to have a degree of gas sensing abilities. It will be interesting to investigate how magnetism could influence gas sensing. It is strongly recommended studies on materials preferably synthesized or modified by high energy ball milling be further investigated in order to study the changes in properties. Furthermore, it has been reported that B site substitution in perovskite oxides play an important role in the adsorption of different gases. The B sites partial substitution could play an important role in modifying sensing behavior in the material therefore it will be of great interest to study the influence of varying Fe-Ni-Ti content in the material. This is expected to lead to materials that have different physical, chemical and magnetic properties. A better understanding of surface science and gas/solid interaction is further required, this will assist in the understanding of the adsorption phenomena and electrical resistivity changes. Ultimately, gas sensing tests will need to be conducted to determine how the materials perform under hazardous environmental gases with particular interest in gas/sensor selectivity properties.

Bibliography

[1] S. Kanan, M. El-Kadri, I. Abu-Yousef and M. Kanan. Semiconducting metal oxide based sensors for selective gas pollutant detection. *Sensors*, 9:8158–8196, 2009.

[2] G. Fine, L. Cavanagh, A. Afonja and R. Binions. Metal oxide semi-conductor gas sensors in environmental monitoring. *Sensors*, 10:5469–5502, 2010.

[3] S. Capone, A. Forleo, R. Rella, P. Siciliano, J. Spadavecchia, D. Presicce and A. Taurino. Solid state gas sensors: State of the art and future activities. *ChemInform*, 35, 2004.

[4] G. Korotcenkov. Metal oxides for solid-state gas sensors: What determines our choice? *Material Science and Engineering B: Solid State Materials for Advanced Technology*, 139:1–23, 2007.

[5] T. Seiyama, A. Kato, K. Fujiishi and M. Nagatani. A new dectector for gaseous components using semiconductive thin films. *Analytical Chemistry*, 34:1502–1503, 1962.

[6] Y. Sun, S. Liu, F. Meng, J. Liu, Z. Jin, L. Kong and J. Liu. Metal oxide nanostructures and their gas sensing properties: A review. *Sensors*, 12:610–631, 2012.

[7] S. Seal and S. Shukla. Nanocrystalline SnO gas sensors in view of surface reactions and modifications. *JOM*, 54:35–38, 2002.

[8] D. Matatagui, O. Kolokoltsev, N. Qureshi, E. Mejia-Uriarte and J. Saniger. A magnonic gas sensor based on magnetic nanoparticles. *Nanoscale*, 7:9607–9613, 2015.

[9] D. Matatagui, O. V. Kolokoltsev, N. Qureshi, E. V. Mejía-Uriarte, C. L. Ordoñez-Romer, A. Vázquez-Olmos and J. M. Saniger. Magnonic sensor array based on

magnetic nanoparticles to detect, discriminate and classify toxic gases. *Sensors and Actuators, B: Chemical*, 240:497–502, 2017.

[10] G. Dong, H. Fan, H. Tian, J. Fang and Q. Li. Gas-sensing and electrical properties of perovskite structure p-type barium-substituted bismuth ferrite. *RSC Adv.*, 5:618–623, 2015.

[11] E. Comini. Metal oxide nano-crystals for gas sensing. *Analytica Chimica Acta*, 568(1):28 – 40, 2006.

[12] C. Wang, L. Yin, L. Zhang and D. Xiang R. Gao. Metal oxide gas sensors: Sensitivity and influencing factors. *Sensors*, 10:2088–2106, 2010.

[13] A. Mishra. Iron-doped $BaTiO_3$: Influence of iron on physical properties. *Materials Science and Applications*, 1:1–14, 2012.

[14] Z. Cheng and J. Lin. Layered organic-inorganic hybrid perovskites: structure, optical properties, film preparation, patterning and templating engineering. *CrystEngComm*, 12:2646–2662, 2010.

[15] J. Haines, J. Rouquette, V. Bornand, M. Pintard, P. Papet and F. Gorelli. Scattering studies at high pressure and low temperature: technique and application to the piezoelectric material $PbZr_{0.52}Ti_{0.48}O_3$. *Journal of Raman Spectroscopy*, 34:519–523, 2003.

[16] L.G. Tejuca and J.L. Fierro. *Properties and applications of perovskite-type oxides.* CRC Press, 2^{nd} edition, 1992.

[17] L. G. Tejuca, J.L. Fierro and J. M. Tascon. Structure and reactivity of perovskite-type oxides. 36:237–328, 1989.

[18] R. Roth. Classification of perovskite and other ABO_3 - type compounds. *Journal of Research of the National Bureau of Standards*, 58:75–88, 1957.

[19] J.L. Fierro M.A. Pena. Chemical structures and performance of perovskite oxides. *Chemcal Reviews*, 101:1981–2018, 2001.

[20] L. J. Berchmans, R. Sindhu, S. Angappan and C. Augustin. Effect of antimony substitution on structural and electrical properties of $LaFeO_3$. *Journal of Materials Processing Technology*, 207:301–306, 2008.

[21] N. Kumar, A. Shukla, C. Behera and R. Choudhary. Structural, electrical and magnetic properties of $Bi(Ni_{0.45}Ti_{0.45}Fe_{0.10})O_3$. *Journal of Alloys and Compounds*, 688:858–869, 2016.

[22] J. B. MacChesney, R. C. Sherwood and J. F. Potter. Electric and magnetic properties of the strontium ferrates. *J. Chem Phys*, 43(6):1907–1913, 1965.

[23] M. Musa Saad H.-E. Investigation on structural, electronic and magnetic properties of perovskites $SrMO_3$ (M =Mn and Co) via gga and gga + u methods. *Journal of Science: Advanced Materials and Devices*, 2(1):115 – 122, 2017.

[24] P. Lemmens and P. Millet. Lecture notes in spin-orbit-topology, a triptych in *Quantum Magnetism* , 2004.

[25] J. Hemberger, P. Lunkenheimer, R. Fichtl, H. A. K. Von Nidda, V. Tsurkan and A. Loidl. Relaxor ferroelectricity and colossal magnetocapacitive coupling in ferromagnetic $CdCr_2S_4$. *Nature*, 434:364, 2005.

[26] D. Higashiyama, S. Miyasaka, N. Kida, T. Arima and Y. Tokura. Control of the ferroelectric properties of $DyMn_2O_5$ by magnetic fields. *Phys. Rev. B*, 70:174–405, 2004.

[27] H. Zheng, J. Wang, S. E. Lofland, Z. Ma, L. Mohaddes-Ardabili, T. Zhao, L. Salamanca-Riba, S. R. Shinde, S. B. Ogale, F. Bai, D. Viehland, Y. Jia, D. G. Schlom, M. Wuttig, A. Roytburd and R. Ramesh. Multiferroic $BaTiO_3$-$CoFe_2O_4$ nanostructures. *Science*, 303:661–663, 2004.

[28] S. Royer, F. S. Berube and S. Kaliaguine. Effect of the synthesis conditions on the redox and catalytic properties in oxidation reactions of $LaCo_{1-x}Fe_xO_3$. *Applied Catalysis A: General*, 282:273–284, 2005.

[29] K. C. Patil, S. T. Aruna and T. Mimani. Combustion synthesis: an update. *Current Opinion in Solid State & Materials Science*, 6:507–512, 2002.

[30] L. Y. Wu, J. M. Ma, H. B. Huang, R. F. Tian, W. J Zheng and Y. F. Hsia. Hydrothermal synthesis and ^{121}sb Mössbauer characterization of perovskite type oxides:Ba_2SbLnO_6 (Ln = Pr, Nd, Sm, Eu). *Mater. Charact*, 61:548–553, 2010.

[31] X. Qi, J. Zhou, Z. X. Yue, Z. L. Gui and L. T. Li. A simple way to prepare nanosized $LaFeO_3$ powders at room temperature. *Ceramics International*, 29:347–349, 2003.

[32] J. Sfeir, S. Vaucher, P. Holtappels, U. Vogt, H. J. Schindler, J. Van Herle, E. Suvorova, P. Buffat, D. Perret, N. Xanthopoulos, & O. Bucheli. Characterization of perovskite powders for cathode and oxygen membranes made by different synthesis routes. *Journal of the European Ceramic Society*, 282:1991–1995, 2005.

[33] O. Carp, L. Patron, A. Ianculescu, J. Pasuk, and R. Ola. New synthesis routes for obtaining dysprosium manganese perovskites. *Journal of Alloys and Compounds*, 351:314–318, 2003.

[34] Y. Shlapa, S. Solopan, A. Bodnaruk, M. Kulyk, V. Kalita, Y. Tykhonenko-Polishchuk, A. Tovstolytkin and A. Belous. Effect of Synthesis Temperature on Structure and Magnetic Properties of $(La, Nd)_{0.7}Sr_{0.3}MnO_3$ Nanoparticles. *Nanoscale Research Letters*, 12:100, 2017.

[35] P. G. Radaelli, G. Iannone, M. Marezio, H. Y. Hwang, S. W. Cheong, J. D. Jorgensen and D. N. Argyriou. Structural effects on the magnetic and transport properties of perovskite $A_{1-x}A'_xMnO_3$ ($x = 0.25, 0.30$). *Phys. Rev. B*, 56:265–276, 1997.

[36] N. Thuy and D. Minh. Size Effect on the Structural and Magnetic Properties of Nanosized Perovskite $LaFeO_3$ Prepared by Different Methods. *Advances in Materials Science and Engineering*, 2012:1–6, 2012.

[37] S. M. Khetre, H. V. Jadhav, P. N. Jagadale, S. R. Kulal and S. R. Bamane. Studies on electrical and dielectric properties of $LaFeO_3$. *Advances in Applied Science Research*, 2:503–511, 2011.

[38] M. C. Carotta, G. Martinelli, Y. Sadaoka, P. Nunziante and Enrico Traversa. Gas-sensitive electrical properties of perovskite-type smfeo3 thick films. *Sensors and Actuators B: Chemical*, 48:270 – 276, 1998.

[39] J.M.D. Coey. *Magnetism and Magnetic Materials.* Cambrigdge University Press. pages 7–8, 24–25, 50–56, 63, 195–203, 330, 329, 2009.

[40] C. G. Stefanita. *Magnetism: Basic and Applications.* Springer, 2^{nd} edition, 2012.

[41] C. Kittel. Ferromagnetic Resonance. *Journal de Physique et le Radium*, 12, 1951.

[42] A. P. Guimaräes. Magnetism and magnetic resonance in solids. *John Wiley & Sons*, pages 12–18, 27–35, 47–49,119–141, 1988.

[43] A. Goldman. Modern ferrite Technology. *Springer Science +Business Media*, New York. pages 24, 52–53, 2006.

[44] S. Laurent, C. Henoumont, D. Stanicki, S. Boutry, E. Lipani, S. Belaid, R. Muller and L. Vander Elst. MRI Contrast Agents. pages 5–12, 2017.

[45] B. Moskowitz. Hitchhiker's Guide to Magnetism. *Environment Magnetic Work*, 270:48, 1991.

[46] N. Osman. *Sythesis, structural and magnetic characterization of spinel nanoparticle ferrites with application for electrochemical sensors.* University of KwaZulu-Natal, PhD Dissertation, 2015.

[47] `http://www.physics.oregonstate.edu/~tgiebult/COURSES/ph674/mfa4.pdf` [Accessed: 06-07-2017].

[48] R. Winpenny. *Molecular Cluster Magnets.* World Scientific, 2011.

[49] J. Frenkel and J. Dorfman. Spontaneous and induced magnetisation in ferromagnetic bodies. *Nature*, 126:274, 1930.

[50] C. Kittel. Theory of the structure of ferromagnetic domains in films and small particles. *Phys. Rev.*, 70:965–971, 1946.

[51] J. Frenkel and J. Dorfman. Superparamagnetism : Theory and Applications. *Researchgate*, pages 1–27, 2012.

[52] O. Petracic. Superparamagnetism Nanoparticle Ensembles. *Superlattices and Microstructures*, 47:569–578, 2010.

[53] C. Kittel. *Introduction to Solid State Physics. John Wiley & Sons*, page 207, 2011.

[54] A. Goldman. *Modern ferrite Technology.* Springer. pages 9–14, 17–21, 52, 55, 2010.

[55] C. Tannous and J. Gieraltowski. The stoner–wohlfarth model of ferromagnetism. *European Journal of Physics*, 29(3):475, 2008.

[56] G. Wertheim. *Mössbauer effect: Principles and Applications.* Acedamic Press INC, 1964.

[57] D. Dickson and F. Berry. *Mössbauer Specrtoscopy.* Cambridge University Press, 1986.

[58] N. Greenwood and T. Gibb. *Mössbauer Spectroscopy.* Chapman and Hall Ltd, London, 1971.

[59] H. Frasch and H. Menke. V08:*Mössbauer Effect.* **4**, 2013.

[60] P. Schaaf. *Mössbauer Spectroscopy.* **4**, 2005.

[61] P. Gütlich, E. Bill, and A.X. Trautwein. *Mössbauer Spectroscopy and Transition Metal Chemistry.* Springer Heidelberg Dordrecht London, New York. pages 11–15, 80, 2011.

[62] P. Dominic, E. Dickson, and F.J. Berry. *Mössbauer Spectroscopy.* Cambridge University Press, London. 1986.

[63] H.R. Verma. *Atomic and Nuclear Analytical Methods.* Springer-Verlag Berlin Heidelberg. pages 198–382, 2007.

[64] A.K Cheetham and P. Day. *Solid State Chemistry: Techniques.* Oxford University Press, 1^{st} edition, 1987.

[65] J. Sunarso, S. Baumann, J. M. Serra, W. A. Meulenberg, S. Liu, Y. S. Lin and J. C. Diniz da Costa. Mixed ionic-electronic conducting (miec) ceramic-based membranes for oxygen separation. *Journal of Membrane Science*, 320:13–14, 2008.

[66] C. Suryanarayana. Mechanical alloying and milling. *Progress in Material Science*, 46:1–184, 2001.

[67] V.V. Boldyrev and K. Tkacova. Mechanochemistry of solids: Past, present and prospects. *Journal of Materials Synthesis and Processing*, 8:121–132, 2000.

[68] S.J. Golosov. Introduction to ultrafine milling in planetary mills. *Nauka, Novosibirsk*, pages 103–129, 1971.

[69] F.L. Zhang and F. Saito. Mechanochemical synthesis of $LaMnO_3$ from La_2O_3 and Mn_2O_3 powders. *J. Alloys Comp.*, 297:99–103, 2000.

[70] Q. Zhang, T. Nakagawa and F. Saito. Mechanochemical synthesis of $La_{0.7}Sr_{0.3}MnO_3$ by grinding constituent oxides. *Journal of Alloys and Compounds*, 308(1):121 – 125, 2000.

[71] F.L. Zhang and F. Saito. Effect of Fe_2O_3 crystallite size on its mechanochemical reaction with La_2O_3 to form $LaFeO_3$. *Journal of Materials Science*, 36:2287–2290, 2001.

[72] H. Alamdari and S. Royer. *Mechanochemistry: Perovskites and Related. Mixed Oxides Concepts and Applications*. Wiley-VCH Verlag GmbH & Co. KGaA, 2016.

[73] F.L. Zhang, M. Zhu and C.Y. Wang. Parameters optimization in the planetary ball milling of nanostructured tungsten carbide/cobalt powder. *Int. J. Refract. Met. Hard Mater*, 26:329–333, 2008.

[74] V.F. Freitas, H.L. Grande, S.N. de Medeiros, I.A. Santos, L.F. Cotica and A.A Coelho. Structural, microstructural and magnetic investigations in high-energy ball milled $BiFeO_3$ and $Bi_{0.95}Eu_{0.05}FeO_3$ powders. *J. Alloys Comp.*, 461:48–52, 2008.

[75] H.B. Bob. *Two-dimensional X-ray diffraction*. John Wiley & Sons, Inc., 2009.

[76] S. Keav, S. Matam, D. Ferri and A. Weidenkaff. Structured Perovskite-Based Catalysts and Their Application as Three-Way Catalytic Converters-A Review. *Catalyst*, 4:226–255, 2014.

[77] J. E. Tasca, A. E. Lavat and M. Gloria. Double perovskites La_2MMnO_6 as catalyst for propane combustion. *Integrative Medicine Research*, 5:235–241, 2017.

[78] V. Lantto, S. Saukko, N. N. Toan, L. F. Reyes and C. G. Granqvist. Gas sensing with perovskite-like oxides having ABO_3 and BO_3 structures. *Integrative Medicine Research*, 13:721–726, 2004.

[79] S. Maike, A. Leifert and U. Simon. Preparation and gas sensing characteristics of nanoparticulate p-type semiconducting $LnFeO_3$ and $LnCrO_3$ materials. *Advanced Functional Materials*, 17:89–97, 2007.

[80] Anon. Preparation, characterization and gas-sensing properties of rare earth mixed oxides. *Sensors and Actuators B: Chemical*, 99:399–404, 2004.

[81] A. Asamitsu, Y. Moritomo, T. Arima and Y. Tokura. A structural phase transition induced by an external magnetic field. *Nature*, 373:407–409, 1995.

[82] Y. Harumi, S. Natsuko, H. Teruhisa and Y. Katsuhiko. Recent developments in solid oxide fuel cell materials. 20:117–131, 2001.

[83] S. Skinner, M. Laguna-bercero and A. Miguel. Advanced inorganic materials for solid oxide fuel cells. 44:1–100, 2010.

[84] T. Yao, A. Ariyoshi and T. Inui. Synthesis of $LaMeO_3$ (M = Cr,Mn, Fe, Co) perovskite oxides from aqueous solutions. *Journal of the American Ceramic Society*, 80:41–44, 2005.

[85] Anon. Oxygen ion migration in perovskite-type oxides. *Journal of Solid State Chemistry*, 118:125–132, 1995.

[86] D. Athayde, D. Souza, A. Silva, D. Vasconcelos, E. Nunes, J. Diniz da Costa and W. Vasconcelos. Review of perovskite ceramic synthesis and membrane preparation methods. *Ceramics International*, pages 1–43, 2015.

[87] Y. Chiang, D. Birnie and W. Kingery. *Physical ceramics : principles for ceramic science and engineering*. Wiley, 1997.

[88] A. Sobhani-Nasab, S. Hosseinpour-Mashkani, M. Salavati-Niasari, H. Taqriri, S. Bagheri and K. Saberyan. Synthesis, characterization, and photovoltaic application of $NiTiO_3$ nanostructures via two-step sol–gel method. *Journal of Materials Science: Materials in Electronics*, 26:5735–5742, 2015.

[89] N. T. Thuy, D. L. Minh, H. T. Giang and N. N. Toan. Structural, electrical, and ethanol-sensing properties of $La_{1-x}Nd_xFeO_3$ nanoparticles. *Advances in Material Science and Engineering*, 2014:5–10, 2014.

[90] M. Scafetta, A. Cordi, J. Rondinelli and S. May. Band structure and optical transitions in $LaFeO_3$: theory and experiment. *Journal of Physics: Condensed Matter*, 26:502–506, 2014.

[91] `http://www.crystalimpact.com/match/` [Accessed: 12-06-2016].

[92] J. Rodriguez-Carvajal. Fullprof Tutorial. 447:1–26, 2011.

[93] L. Mccusker, R. Dreele, D. Cox, E. Loue and P. Scardi. Rietveld refnement guidelines. *International Union of Crystallography Journal of Applied Crystallography J. Appl. Cryst*, 32:36–50, 1999.

[94] `http://www.gatan.com/products/tem-analysis/gatan-microscopy-suite-software` [Accessed: 25-10-2016].

[95] `https://imagej.net/Particle_Analysis` [Accessed: 15-02-2017].

[96] K. Peng, L. Fu, H. Yang and J. Ouyang. Perovskite $LaFeO_3$/montmorillonite nanocomposites: synthesis, interface characteristics and enhanced photocatalytic activity. *Scientific Reports*, 6:19–23, 2016.

[97] S. Thirumalairajan, K. Girija, V. Ganesh, D. Mangalaraj, C. Viswanathan and N. Ponpandian. Novel synthesis of $LaFeO_3$ nanostructure dendrites: A systematic investigation of growth mechanism, properties, and biosensing for highly selective determination of neurotransmitter compounds. *Crystal Growth and Design*, 13:291–302, 2013.

[98] S. A. Ivanov, R. Tellgren, F. Porcher, T. Ericsson, A. Mosunov, P. Beran, S. K. Korchagina, P. Anil Kumar, R. Mathieu and P. Nordblad. Preparation, structural, dielectric and magnetic properties of $LaFeO_3$-$PbTiO_3$ solid solutions. *Material Research Bulletin*, 47:1–33, 2012.

[99] C. Jagadeeshwaran, A. P. Selvadurai, V. Pazhanivelu and R. Murugaraj. Structure, Optical and Magnetic behavior of $LaFeO_3$ and

$LaFe_{0.9}Ni_{0.1}O_{3-\delta}$ by combustion method. *International Journal of Innovative Research in Science & Engineering*, pages 9–14, 2014.

[100] S. V. Andreev, M. I. Bartashevich, V. I. Pushkarsky, V. N Maltsev, L. A. Pamyatnykh, E. N. Tarasov, N. V. Kudrevatykh and T. Goto. Law of approach to saturation in highly anisotropic ferromagnets application to NdFeB melt-spun ribbons. *Journal of Alloys and Compounds*, 260:196–200, 1997.

[101] M.S. Islam, M. Cherry and C.R.A. Catlow. Oxygen diffusion in $LaMnO_3$ and $LaCoO_3$ perovskite-type oxides: A molecular dynamics study. *Journal of Solid State Chemistry*, 124(2):230 – 237, 1996.

[102] F. J. Berry, X. Ren and J. F. Marco. Reduction properties of perovskite-related rare earth orthoferrites. *Czechoslovak Journal of Physics*, 55(7):771–780, 2005.

[103] G. Shirane, D. Cox and S. Ruby. Mössbauer study of isomer shift, quadrupole interaction, and hyperfine field in several oxides containing ^{57}Fe. *Physical Review*, 125:158–165, 1962.

[104] S. McWilliams, E. Brennan-Wydra, K. Cory MacLeod and P. Holland. Density Functional Calculations for Prediction of ^{57}Fe mössbauer Isomer Shifts and Quadrupole Splittings in β-Diketiminate Complexes. *ACS Omega*, 2:594–606, 2017.

[105] H. Abdallah, T. Moyo and J. Z. Msomi. Mössbauer and electrical studies of $Mn_xCo_{1-x}Fe_2O_4$ compounds prepared via glycothermal route. *Journal of Superconductivity and Novel Magnetism*, 24:669–673, 2011.

[106] Anon. Screen-printed perovskite-type thick films as gas sensors for environmental monitoring. *Sensors and Actuators B: Chemical*, 55:99–110, 1999.

[107] T. Arakawa, H. Kurachi and J. Shiokawa. Physicochemical properties of rare earth perovskite oxides used as gas sensor material. *Journal of Materials Science*, 20:207–210, 1985.

[108] K. Sing. Reporting physisorption data for gas/solid systems with special reference to the determination of surface area and porosity (recommendations 1984). *Pure and Applied Chemistry*, 57:603–619, 1985.

[109] H. Su, L. Jing, K. Shi, C. Yao and H. Fu. Synthesis of large surface area $LaFeO_3$ nanoparticles by SBA-16 template method as high active visible photocatalysts. *Journal of Nanoparticle Research*, 12:967–974, 2010.

[110] B. Clair, J. Gril, F. Di Renzo, H. Yamamoto and F. Quignard. Characterization of a gel in the cell wall to elucidate the paradoxical shrinkage of tension wood. *Biomacromolecules*, 9:494–498, 2008.

[111] R. Palai, R. S. Katiyar, H. Schmid, P. Tissot, S. J. Clark, J. Robertson, S. A. T. Redfern, G. Catalan and J. F. Scott. β phase and γ - β metal-insulator transition in multiferroic $BiFeO_3$. *Physical Review B - Condensed Matter and Materials Physics*, 77(1):1–11, 2008.

[112] D. Jia, J. Xu, H. Ke, W. Wang, Y. Zhou, J. Lu, A. Gunther, F. Schrettle, F. Mayr, S. Krohns, P. Lunkenheimer, A. Pimenov, V. D. Travkin, A. A. Mukhin and A. Loidl. On the room temperature multiferroic $BiFeO_3$: magnetic, dielectric and thermal properties. *Physical Review B - Condensed Matter and Materials Physics*, 29(4):3099–3102, 2009.

[113] A. Shukla, B. Nitin Kumar, B. Behera, N. P. Choudhary and R Bullet. Structural, dielectric and magnetic characteristics of $Bi(Ni_{0.25}Ti_{0.25}Fe_{0.5})O_3$ ceramics. *Journal of Materials Science: Materials in Electronics*, 27(2):1209–1216, 2015.

[114] A. Perejón, N. Masó, A. R. West, P. E. Sánchez-Jiménez, R. Poyato, J. M. Criado and L. A. Pérez-Maqueda. Electrical properties of stoichiometric $BiFeO_3$ prepared by mechanosynthesis with either conventional or spark plasma sintering. *Journal of the American Ceramic Society*, 96:1220–1227, 2013.

[115] W. Tang, H. Lin, S. Yang, Y. Zhang, Y. Tong and S. Xie. Structural, photocatalytic and enhanced magnetic properties of $Bi_{1-x}Ho_xFeO_3$ nanoparticles synthesized via sol-gel method. *Ferroelectrics*, 489(1):65–72, 2015.

[116] Y. Nomura, T. Tachi, T. Kawae and A. Morimoto. Electric and magnetic properties of the strontium ferrates. *Physica Status Solidi (B) Basic Research*, 252:833–838, 2015.

[117] G. L. Yuan, S. W. Or, Y. P. Wang, Z. G. Liu and J. M. Liu. Preparation and multi-properties of insulated single-phase $BiFeO_3$ ceramics. *Solid State Commun*, 138(2):76–81, 2006.

[118] P. Manimuthu and C. Venkateswaran. Evidence of ferroelectricity in $SrFeO_{3-\delta}$. *Journal of Physics D: Applied Physics*, 45(1):015–303, 2012.

[119] I. R. Shein, V. L. Kozhevnikov and A. L. Ivanovskii. New half-metallic ferromagnets: Double perovskites Sr(FeM)O_3 (m = Sn, Ti, Zr). *JETP Letters*, 82(4):239–242, 2005.

[120] Y. Wang, J. Chen and X. Wu. Preparation and gas-sensing properties of perovskite-type $SrFeO_3$ oxide. *Materials Letters*, 49(6):361 – 364, 2001.

[121] P. K. Gallagher, J. B. MacChesney and D. N. E. Buchanan. Mössbauer effect in the system $Sr_3Fe_2O_{6-7}$. *J. Chem Phys*, 45(7):2466–2427, 1966.

[122] J.P. Hodges, S. Short, J.D. Jorgensen, X. Xiong, B. Dabrowski, S.M. Mini and C.W.Kimball. Evolution of oxygen-vacancy ordered crystal structure in the perovskite series $Sr_nFe_nO_{3n-1}$ (n=2,4,8 and ∞), and the relationship to electronic and magnetic properties. *J. Solid State Chem*, 151(36):190–209, 2000.

[123] S. Srinath, M. Mahesh Kumar, M. L. Post and H. Srikanth. Magnetization and magnetoresistance in insulating phases of $SrFeO_{3-\delta}$. *Phys. Rev. B*, 72(5):054– 425, 2005.

[124] M. Chen, S. Paulson, W. H. Kan, V. Thangadurai and V. Birss. Surface and bulk study of strontium-rich chromium ferrite oxide as a robust solid oxide fuel cell cathode. *J. Mater. Chem. A*, 3(45):14–26, 2015.

[125] P. Manimuthu, R. Murugaraj and C. Venkateswaran. Non-universal dielectric relaxation in $SrFeO_{3-\delta}$. *Physics Letters A*, 378(36):725–728, 2014.

[126] C . Solis, M. D. Rossell, G. Garcia, A. Figueras, G. Van Tendello and J. Santiso. Microstructure and high temperature transport properties of high quality epitaxial $SrFeO_{3-\delta}$ films. *Solid State Ionics*, 179:1996–1999, 2008.

[127] G. Sberveglieri. Recent developments in semiconducting thin-film gas sensors. *Sensors and Actuators B: Chemical*, 23(2):103 – 109, 1995.

[128] A. Rothschild and H. L. Tuller. Gas sensors: New materials and processing approaches. *Journal of Electroceramics*, 17(2):1005 – 1012, 2006.

[129] J. W. Fergus. Perovskite oxides for semiconductor-based gas sensors. *Sensors and Actuators B: Chemical*, 123(2):1169 – 1179, 2007.

[130] D. H. Chen and X. He. Synthesis of nickel ferrite nanoparticles by sol-gel method. *Mater. Res. Bull*, 36:369 – 377, 2001.

[131] Z. Zi, Y. Sun, X. Zhu, Z. Yang, J. Dai and W. Song. Synthesis and magnetic properties of $CoFe_2O_4$ ferrite nanoparticles. *J. Magn. Magn. Mater*, 321:251 – 2255, 2009.

[132] Z. Zhang, L. Wang, X. Xu, Y. Dong and L. Zhang. Development of a validated HPLC method for the determination of tenofovir disoproxil fumarate using a green enrichment process. *J. Anal Methods*, 7:290 – 298, 2015.

[133] C. Xiangfeng, J. Dongli and Z. Chenmou. The preparation and gas-sensing properties of $NiFe_2O_4$ nanocube and nanorods. *Sens. Actuators: B*, 123:793 – 797, 2007.

[134] D. Zhang, X. Zhang, X. Ni, H. Zheng and D. Yang. Synthesis and characterization of $NiFe_2O_4$ magnetic nanorods via a PEG-assisted route. *J. Magn. Magn. Mater*, 292:79 – 82, 2005.

[135] `http://www.panalytical.com/Xray-diffraction-software.htm` [Accessed: 05-06-2017].

[136] M. Toozandehjani, K. A. Matori, F. Ostovan, S. Abdul Aziz, M. S. Mamat and M.d. Shuhazlly. Effect of milling time on the microstructure, physical and mechanical properties of al-al2o3 nanocomposite synthesized by ball milling and powder metallurgy. *Materials*, 10(11), 2017.

[137] A. Wagih. Mechanical properties of Al–Mg/Al_2O_3 nanocomposite powder produced by mechanical alloying. *Adv. Powder Technol.*, 26:253–258, 2015.

[138] W. B. Dlamini, J. Z. Msomi and T. Moyo. XRD, Mössbauer and magnetic properties of $Mg_xCo_{1-x}Fe_2O_4$ nanoferrites. *Journal of Magnetism and Magnetic Materials*, 373:78–82, 2015.

[139] H. M. I. Abdallah and T. Moyo. Superparamagnetic behavior of $Mn_xNi_{1-x}Fe_2O_4$ spinel nanoferrites. *Journal of Magnetism and Magnetic Materials*, 361:170–174, 2014.

[140] I. P. Ezekiel and T. Moyo. Structural and magnetocaloric effect studies of $Ni_{43-x}T_{ix}Mn_{46}Sn_{11}$ heusler alloys. *Journal of Alloys and Compounds*, 749:672 – 680, 2018.

[141] I. Kong, S. H. Ahmad, M. H. Abdullah and A. N Yusoff. The effect of temperature on magnetic behavior of magnetite nanoparticles and its nanocomposites. *American Institute of Physics*, 1136:830–834, 2009.

[142] I. Szafraniak-Wiza, B. Andrzejewski and B. Hilczer. Magnetic properties of bismuth ferrite nanopowder obtained by mechanochemical synthesis. *Acta Physica Polonica A*, 126:1029–1031, 2014.

[143] W. B. Mdlalose, S. R. Mokhosi, S. Dlamini, T. Moyo and M. Singh. Effect of chitosan coating on the structural and magnetic properties of $MnFe_2O_4$ and $Mn_{0.5}Co_{0.5}Fe_2O_4$ nanoparticles. *AIP Advances*, 8:056726, 2018.

[144] A. Wei, S. Tao, Y. Fang, Z.D. Han, B. Qian, X.F. Jiang, H. Zhou, R.J. Tang and D.H. Wang. Magnetically tunable bipolar switching of the exchange-bias field in Co_2TiO_4. *Journal of Magnetism and Magnetic Materials*, 441:361 – 365, 2017.